

## ABSTRACT

WILLIAMS, AUSTIN H. Particles with “Gecko Legs”: Making and Applications of a Novel Hierarchical Nanomaterial. (Under the direction of Dr. Orlin D. Velev).

The complex morphology and chemistry of polymer nanomaterials enable many impressive natural phenomena and the functionalities of numerous consumer products and nanotechnologies. The novel technique of continuous polymer precipitation under turbulent liquid shear can scalably produce colloidal particles with controlled morphologies. Branched, nanofibrous soft dendritic colloid (SDC) and nanosheet (NS) particulates can be produced using this method from nearly any polymer. In this dissertation, the parameters governing the production of these advanced novel particle morphologies are investigated and their performance in soft matter applications related to coatings, gels, and membranes is evaluated.

The dissertation first presents the background and the principles of the method of polymer precipitation under shear in Chapter 1. Chapter 2 first describes the expansion of the shear-based polymer precipitation method to include hydrogel cross-linking and polyelectrolyte complexation as precipitation mechanisms that are compatible with the technique. Making aqueous suspensions of SDCs from alginate and chitosan enables the investigation of the characteristics of these different types of SDCs by rheometry. A homocomposite system consisting of alginate SDCs as a reinforcement network within a molecular alginate hydrogel is introduced. The combination of colloidal and molecular alginate networks results in synergistic stiffening behavior with the composite. Moreover, the inclusion of the colloidal SDC network in the homocomposite gives the formulation a yield stress even prior to cross-linking the molecular network. Control of the kinetics of gelation in these homocomposites allows the extrusion and 3D printing of these double-network hydrogels without a precipitation bath.

Chapter 3 investigates the application of SDCs as advanced coatings with a specific focus on the use of SDCs as superhydrophobic and anti-icing coatings. We characterize the role of SDC coatings' overlapping fiber topographies on the wetting properties. The results show that the water contact angle on SDC coatings is amplified depending on the composition of the polymer comprising the SDCs. Two strategies to improve the wetting and mechanical properties of SDC coatings are then discussed – forming bicontinuous SDC coatings and using an elastomeric binder. Blending SDC suspensions prior to depositing the coating allows the formation of bicontinuous SDC networks with properties intermediate to the two pure SDC coatings. SDCs pre-mixed with emulsified elastomeric binder form composite coatings with improved wetting and ice adhesion properties. We show that both of these strategies can be used in facile ways to produce coatings with hydrophobic and anti-icing properties.

Chapter 4 discusses how SDCs can be applied in porous membranes. Using two diverse applications of porous polymer materials – bioscaffolds and lithium-ion battery separators – we investigate the structure-property relationships between the SDCs or NSs and the membranes from which they are composed. The pore structures of both types of membranes are explored and the effect of particle morphology on the porosity is characterized. The trends seen in the modulation of membrane properties by altering morphology of the particles from which it is composed in both polyurethane and polyvinylidene fluoride SDCs are compared as well as the impact of these morphological changes in their respective applications.

In the final section of this dissertation, the molecular mechanisms driving the formation of polyelectrolyte multilayer nanocoatings are investigated using a system of chitosan and alginate. The concept of polyelectrolyte charge-cycling is introduced, quantified, and correlated to multilayer growth. The film growth is further optimized by increasing the deposition temperature.

Finally, the optimized alginate-chitosan nanocoating is investigated as an oxygen barrier for packaging and direct product coating applications.

© Copyright 2021 by Austin Williams

All Rights Reserved

Particles with “Gecko Legs”: Making and Applications of a Novel Hierarchical Nanomaterial

by  
Austin Heath Williams

A dissertation submitted to the Graduate Faculty of  
North Carolina State University  
in partial fulfillment of the  
requirements for the degree of  
Doctor of Philosophy

Chemical Engineering

Raleigh, North Carolina  
2021

APPROVED BY:

---

Dr. Orlin D. Velev  
Committee Chair

---

Dr. Jan Genzer

---

Dr. Lilian Hsiao

---

Dr. Milad Abolhasani

## **BIOGRAPHY**

Austin Williams grew up in Atlanta, GA where graduated from the Westminster Schools. He received a Bachelor of Science in Chemistry from Birmingham-Southern College then went to North Carolina State University to pursue a Ph.D. in Chemical and Biomolecular Engineering under the direction of Dr. Orlin D. Velev.

## **ACKNOWLEDGEMENTS**

I would like to thank my advisor, Dr. Orlin D. Velev, for his guidance and support throughout graduate school. Additionally, I appreciate the support and congeniality from Dr. Velev's research group members, especially Dr. Sangchul Roh, Dr. Sabina Islam, Rachel Bang, and Yosra Kotb. I would like to thank Dr. Peter Fedkiw, Dr. Salvatore Luiso, and Mike Petrecca for their collaborative efforts on the lithium-ion battery separator project as well as the many undergraduate and Master's students I worked with. Finally, I would like to thank Eastman Chemical Company and Dr. Tyler Nelson from Air Force Research Laboratory for their collaboration and support.

## TABLE OF CONTENTS

LIST OF TABLES .....	v
LIST OF FIGURES .....	vi
<b>Chapter 1: Polymer Nanomaterials Fabrication by Precipitation .....</b>	<b>1</b>
1.1. Introduction: fabrication of biomimetic nanomaterials .....	2
1.2. Nanoparticle suspensions and additives for composite reinforcement .....	5
1.3. Porous polymer sheets and nanofiber membranes .....	6
1.4. Shear-driven polymer precipitation and soft dendritic colloids .....	7
1.5. Polyelectrolyte complexation and layer-by-layer film nanoassembly .....	12
1.6. Layout of this dissertation .....	15
<b>Chapter 2: Biopolymer Soft Dendritic Colloids and Self-Reinforced Homocomposite Hydrogels with a Molecular-Colloidal Double Network .....</b>	<b>16</b>
2.1. Introduction .....	17
2.2. Materials and Methods .....	20
2.3. Results .....	23
2.4. Conclusions .....	44
<b>Chapter 3: Porous Sheets and Membranes from Soft Dendritic Colloids .....</b>	<b>47</b>
3.1. Introduction .....	48
3.2. Materials and Methods .....	51
3.3. Results .....	53
3.4. Conclusions .....	62
<b>Chapter 4: Soft Dendritic Colloid Superhydrophobic and Anti-Icing Surface Coatings ...</b>	<b>67</b>
4.1. Introduction .....	68
4.2. Materials and Methods .....	72
4.3. Results .....	75
4.4. Conclusions .....	83
<b>Chapter 5: Layer-By-Layer Polyelectrolyte Nanocoatings for Food-Grade Barrier Films .....</b>	<b>86</b>
5.1. Introduction .....	87
5.2. Materials and Methods .....	89
5.3. Results .....	91
5.4. Conclusions .....	105
<b>Chapter 6: Summary and Perspectives .....</b>	<b>107</b>
REFERENCES .....	118
APPENDICES .....	127
Appendix A: Supplementary information on Chapter 2 .....	128
Appendix B: Supplementary information on Chapter 3 .....	143
Appendix C: Supplementary information on Chapter 4 .....	147
Appendix D: Supplementary information on Chapter 5 .....	149

## LIST OF TABLES

Table 3.1	Porosity and pore Feret diameters of Soft and Stiff PU SDC nonwovens analyzed using Zeiss Xradia micro-CT .....	55
Table 3.2	Number-average pore size ( $P_n$ ), weight-average pore size ( $P_w$ ), and heterogeneity index ( $HG = M_w/M_n$ ) of PVDF SDC membranes .....	61
Table 4.1	Summary of data for water contact angle on thin films and SDC coatings of different polymers and porosities of SDC coatings.....	76
Table 4.2	Mechanical properties of porous SDC sheets composed of PS, PES, and PVOH...	77
Table 5.1	Oxygen barrier properties and comparison of biopolymer coatings at 0% RH .....	103
Table 5.2	Oxygen barrier properties and comparison of biopolymer coatings at 50% RH ...	104

## LIST OF FIGURES

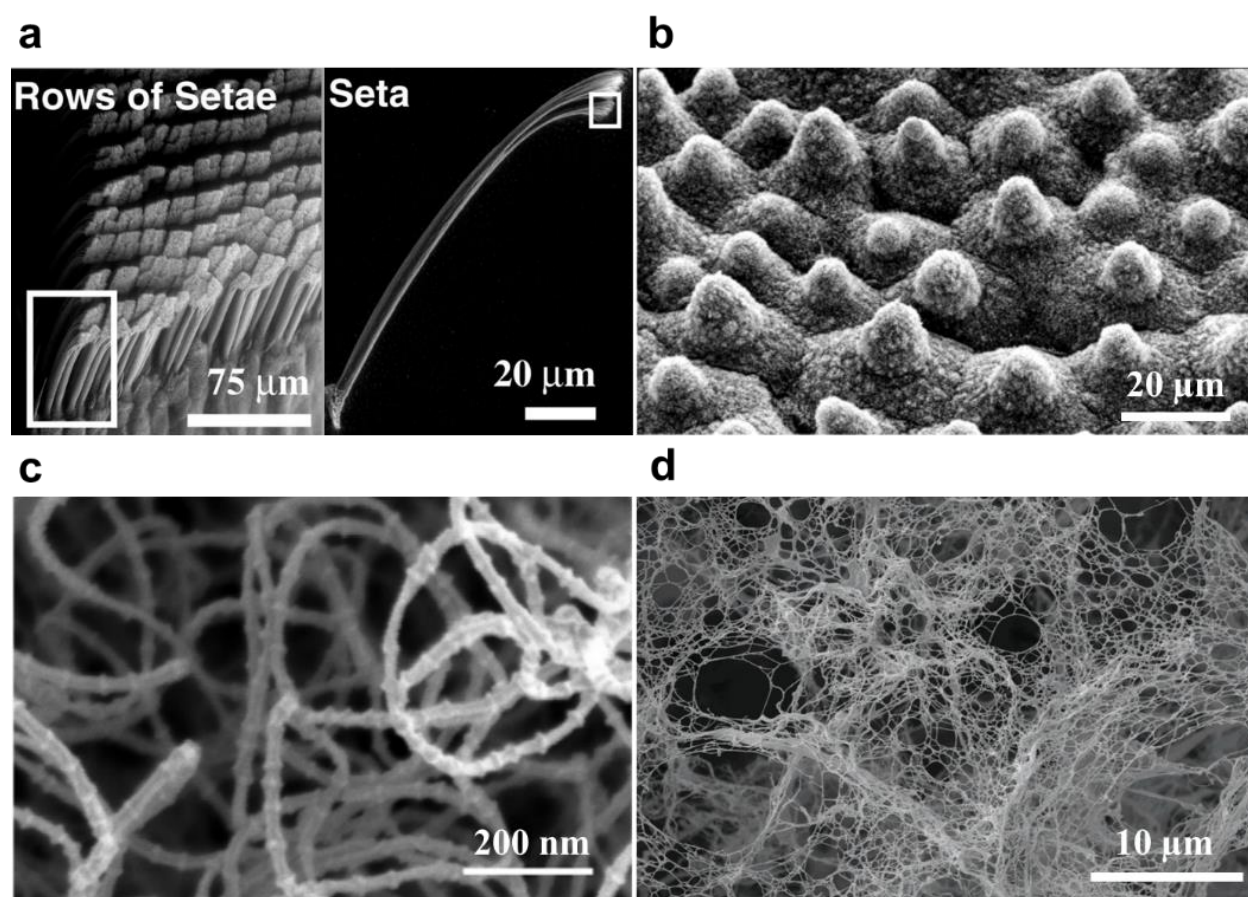
Figure 1.1	Scanning electron microscopy (SEM) images of naturally occurring fibrillar and hierarchical nanomaterials.....	3
Figure 1.2	Examples of common polymer nanofiber fabrication methods. ....	4
Figure 1.3	Polymer particle morphologies resulting from shear-based polymer precipitation in laminar nonsolvent flows.....	8
Figure 1.4	Polymer particle morphologies resulting from shear-driven polymer precipitation in laminar nonsolvent flows.....	10
Figure 1.5	The role of precipitation rate in governing the particle morphologies formed during turbulent shear-driven polymer precipitation allowing production of a broad range of materials from nanoparticles to nanosheets.....	11
Figure 1.6	Schematics of polyelectrolyte composite materials.....	13
Figure 2.1	Precipitation mechanisms utilized for producing nanofibrillated soft dendritic colloids.....	24
Figure 2.2	Controlling morphology of biopolymer particles by shear-driven precipitation.....	26
Figure 2.3	Suspension structuring of particles produced by shear-driven precipitation.....	28
Figure 2.4	Polyelectrolyte cSDCs and their pH-responsive behavior.....	30
Figure 2.5	Turbulent shear-driven precipitation and morphology of a sodium alginate soft dendritic colloid.....	32
Figure 2.6	Linear viscoelasticity and yield stress of SA SDC suspensions and molecular gels.....	34
Figure 2.7	Mechanical properties of SA homocomposite gels.....	37
Figure 2.8	Time-dependent gelation of SA SDC suspensions, SA CMHs, and SA HHGs.....	39
Figure 2.9	3D Printing with homocomposite hydrogels.....	41
Figure 3.1	Schematic of soft dendritic colloid nonwoven preparation and administration of aerosolized nanomaterials on seeded nonwovens.....	50
Figure 3.2	Glycerol addition to the nonsolvent provides polymer processing control over the morphology of the Soft and Stiff PU SDC mats.....	53

Figure 3.3	Morphological characterization of Stiff and Soft PU SDC membranes .....	54
Figure 3.4	Mechanical properties of Stiff and Soft PU SDC membranes .....	56
Figure 3.5	Microscopy of PVDF particles and their membranes. ....	58
Figure 3.6	Schematics of shear-driven polymer precipitation showing the formation of SDC and NS membranes .....	59
Figure 3.7	Mechanical properties of PVDF SDC membranes.....	60
Figure 4.1	Schematic of SDC coating formation.....	70
Figure 4.2	Microscopy of PS, PES, and PVOH SDCs and their coatings.....	76
Figure 4.3	Wetting and anti-icing properties of PS/PVOH bicontinuous SDC coatings .....	80
Figure 4.4	Wetting and anti-icing of PES SDC/PDMS composite coatings .....	82
Figure 5.1	Schematics of the charge cycle driving polyelectrolyte film growth for polyelectrolytes .....	92
Figure 5.2	Charge and conformation of chitosan and alginate .....	94
Figure 5.3	Polyelectrolyte multilayer growth of CS-Alg films .....	95
Figure 5.4	Average bilayer thickness vs. total $\Delta\%Charge$ ( $\Delta\%Charge_{CS} + \Delta\%Charge_{Alg}$ ) for CS-Alg films of different pH systems at room temperature with 45 second dips .....	96
Figure 5.5	Effect of the environmental parameters - temperature, pH, and dipping time on CS-Alg polyelectrolyte multilayer growth .....	98
Figure 5.6	Physical properties of CS – Alg PEM coatings.....	100
Figure 5.7	Barrier properties of CS <sub>6</sub> – Alg <sub>4</sub> LbL coatings .....	103
Figure 5.8	Pictures of an untreated bananas and bananas coated with 25.5 BL of CS <sub>6</sub> – Alg <sub>4</sub> at 60°C with a 5 second dip time .....	104
Figure 6.1	Nanofibrous biopolymer membranes and aerogels .....	109
Figure 6.2	Incorporation of magnetic iron oxide nanoparticles into cellulose acetate SDCs.....	115

## **CHAPTER 1: Nanomaterials Fabrication by Precipitation Under Liquid Shear**

## **1.1 Introduction: fabrication of biomimetic nanomaterials**

Many natural structures have nanoscale features, endowing them with functionalities delivered by these highly adapted nanomaterials. Common examples of these types of natural, nanostructured architectures are the nanofibrous and highly adhesive rows of setae located on the feet of geckos<sup>1,2</sup> that endow them with remarkable adhesion by maximizing van der Waals forces (Figure 1.1a), the surfaces of lotus leaves<sup>3</sup> whose hierarchical roughness and waxy surface enables superhydrophobic and self-cleaning properties (Figure 1.1b), nanofibrous spider webs<sup>4</sup> that show extraordinary strength and elasticity to ensnare insects (Figure 1.1c), and cellulose nanofibrils<sup>5</sup> that strengthen composite plant materials by forming a reinforcement fiber network (Figure 1.1d). Each of these naturally occurring nanomaterials has evolved to enhance their biological functionalities by taking advantage not only of their nano-scale morphologies, but also their finely tuned polymeric surface chemistries.



**Figure 1.1** Scanning electron microscopy (SEM) images of naturally occurring fibrillar and hierarchical nanomaterials. (a) The rows of nanofibrous setae and a singular seta located on the highly adhesive foot pads of geckos.<sup>2</sup> (b) The surface of the lotus leaf showing hierarchical surface roughness.<sup>3</sup> (c) The noded fibrils of the *Hyptiotes cavatus* spider web.<sup>6</sup> (d) microfibrillated cellulose isolated from oat straw cellulose powder.<sup>5</sup>

Immense academic and commercial interest has been focused on the fabrication of polymer nanomaterials, with the goal to synthetically engineer materials where advanced functionalities gained from nanoscale structuring for applications including food products<sup>7,8</sup>, filtration<sup>9,10</sup>, bioscaffolds<sup>11-13</sup>, pharmaceuticals<sup>14,15</sup>, coatings<sup>16-19</sup>, and lithium-ion battery separators.<sup>20-22</sup> Several synthetic techniques have been developed to engineer polymeric nanomaterials with features on the micro- and nanoscale and high aspect ratios. These techniques include lithography, flash precipitation<sup>23,24</sup>, fiber drawing<sup>25</sup>, electrospinning<sup>22,26,27</sup>, meltblowing<sup>28,29</sup>, phase

separation<sup>16,30,31</sup>, and layer-by-layer film formation.<sup>32–35</sup> Other than nanoparticles, nanofibers are the polymer morphology that is most commonly produced by these techniques because of their high surface area and networking properties, however, other colloidal particle morphologies have gained significant interest such as nano-sheet materials with low thickness ( $< 1 \mu\text{m}$ ) for applications in gas separation membranes, energy storage, and coatings.<sup>36,37</sup> Bacteria can be engineered to secrete nanofibrous cellulose, but this technique and similar methods of obtaining naturally-derived fibers require expensive secondary processing steps.<sup>38,39</sup>

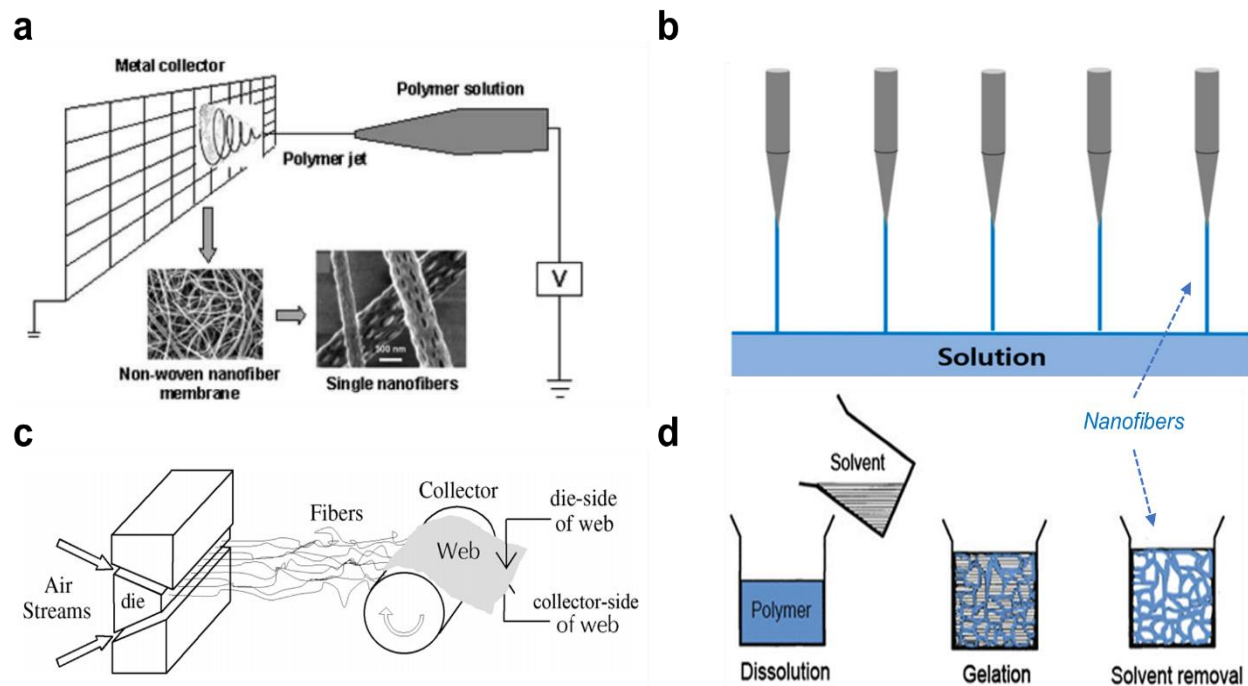


**Figure 1.2** Examples of common polymer nanofiber fabrication methods. (a) Electrospinning polymer webs using high voltage.<sup>40</sup> (b) Needle-drawing nanofibers from polymer solution.<sup>25</sup> (c) Meltblowing nanofiber mats using hot air streams and molten polymer.<sup>10</sup> (d) Polymer nanofibers produced from phase separation and solvent liberation.<sup>31</sup>

## 1.2 Nanoparticle suspensions and additives for composite reinforcement

Large aspect ratio materials like nanoparticles, fibers, and sheet-like particulates are utilized extensively as additives that modify suspension and fluid phase properties.<sup>41</sup> Fumed silica, an inorganic colloidal material, is a thixotropic thickening agent that readily forms a fractal, hydrogen-bonded network throughout the medium and efficiently increases the viscoelastic properties at low volume fractions. The fractal-like structure allows fumed silica to act as single particulates retaining stagnant solvent, subsequently increasing the excluded volume of the particles in suspension.<sup>42</sup> Molecular, hyper-branched polymer dendrimers have also been applied as rheological modifiers due to similar mechanisms of nano-scale network formation within a medium.<sup>43,44</sup> While nearly 3 orders of magnitude larger in size, hydrogel microfibers have shown similar networking behavior as yield stress additives in colloidal suspensions.<sup>45</sup>

Nanomaterial additives can also reinforce composite materials to modify mechanical, conductive, and thermal properties.<sup>46</sup> Both ceramic and polymer nanoparticles are commonly incorporated into polymeric matrices to modify strength, stiffness, and toughness of the composite network.<sup>47,48</sup> Inorganic carbon fibers<sup>49</sup>, cellulosic fibers<sup>5,50,51</sup>, and synthetic electrospun nanofibers<sup>52</sup> have all found applications as additives to efficiently improve the mechanical properties in thermoplastics as well as hydrogels with low additive content enabled by high aspect ratio materials. Highly adapted natural materials like human tissues and plants ubiquitously utilize branched-nanofiber architectures because these structures enhance their strength and improve their heat conductivity and transport properties.<sup>53,54</sup> The additional optimization of these functionalities offered by branched-nanofiber structures have galvanized interest in developing polymer fabrication techniques that achieve a branched-fiber morphologies.<sup>4,55</sup>

### 1.3 Porous polymer sheets and nanofiber membranes

Polymeric membranes with engineered porosities find diverse applications as membranes for filtration, desalination, and gas separation.<sup>56,57</sup> Phase inversion is a common technique in which a polymer solution is cast onto a substrate and immersed in a nonsolvent coagulation bath. Controlling the thermodynamic rate of demixing between the solvent and nonsolvent phases and varying parameters like the polymer concentration, the thickness of the polymer solution, and nonsolvent temperature allows the production of tailored polymeric membranes with controlled thickness, composition, and nano-scale pore structures.<sup>58</sup>

Another common strategy to produce polymer sheets with continuous and controlled pore networks is the fabrication of fibrous nonwovens. Analogous to the three-dimensional network that nanofibers can achieve in suspension and as composite reinforcement additives, nanofibers achieve similar interconnected networks in applications as nonwovens and porous membrane materials. Typically produced by techniques like electrospinning or melt-blowing, nanofiber coatings and nonwovens have found applications such as superhydrophobic surfaces, battery separator materials, and bioscaffolds.<sup>17,28,31</sup> For each of these applications, both the composition and the structure of the nanofiber are paramount towards the material's functional properties. Many research efforts using these techniques have sought to exhibit control over the diameter of the produced nanofibers by varying the polymer molecular weight and concentration, or environmental parameters specific to each technique like the applied voltage or melt temperature.<sup>27,59</sup> The variation of the diameter of the nanofibers in a nonwoven can modify not only the pore size and structure, but can also enable modulation of the mechanical properties of the bulk nonwoven.<sup>28,29</sup> Thus, a better understanding of the structure-property relationships between the colloidal components of these types of nonwoven polymers is critical.

#### 1.4 Shear-driven polymer precipitation and soft dendritic colloids

Recently, a new method of producing polymer nanomaterials introduced by the Velev group has been gaining interest called shear-based polymer precipitation.<sup>60</sup> In this technique, a polymer is dissolved in a solvent and that polymer solution is injected into a sheared nonsolvent medium. As the polymer undergoes precipitation from solution due to the influx of nonsolvent medium, it is templated by the streamlines of the sheared nonsolvent phase to produce structured particulates. The parameters in these liquid-liquid shear systems that are dictating the resulting particle morphologies are (1) the hydrodynamic properties of the solvent and nonsolvent, (2) the polymer concentration and molecular weight in the injection solution, and (3) the rate of precipitation. This method was first investigated in detail using a laminar nonsolvent flow generated within a Couette cell. In Figure 1.3a, it is shown that with little polymer entanglement (low polymer molecular weight or low concentration), the polymer solution undergoes droplet break-up during the influx of nonsolvent and precipitates into nanoparticles.<sup>23,24</sup> As the polymer concentration increases and by altering the compositions of the solvent and nonsolvent phases, the method was adapted to scalable production of microrods and nanofibers (Figure 1.3b-d).<sup>60,61</sup> By increasing the rate of precipitation in laminar nonsolvent system that produces nanofibers, the formation of hollow polymer micro-ribbons is seen due to rapid precipitation at the interface of the polymer solution and the nonsolvent leading to exfoliation and collapse of the nanofiber skin.<sup>62</sup>

The transition from microsphere to nanofiber morphology is expected to occur at a critical capillary number ( $Ca$ ) shown in Equation 1.1, where  $\mu$  is the viscosity of the nonsolvent medium,  $V$  is the characteristic velocity of the medium, and  $\gamma$  is the interfacial tension of the solvent solution. At this critical  $Ca$  value, the inertial forces of the nonsolvent flow overcome the interfacial tension of the polymer solution, driving the elongation of the droplet.

$$Ca = \frac{\mu V}{\gamma} \quad (\text{Equation 1.1})$$

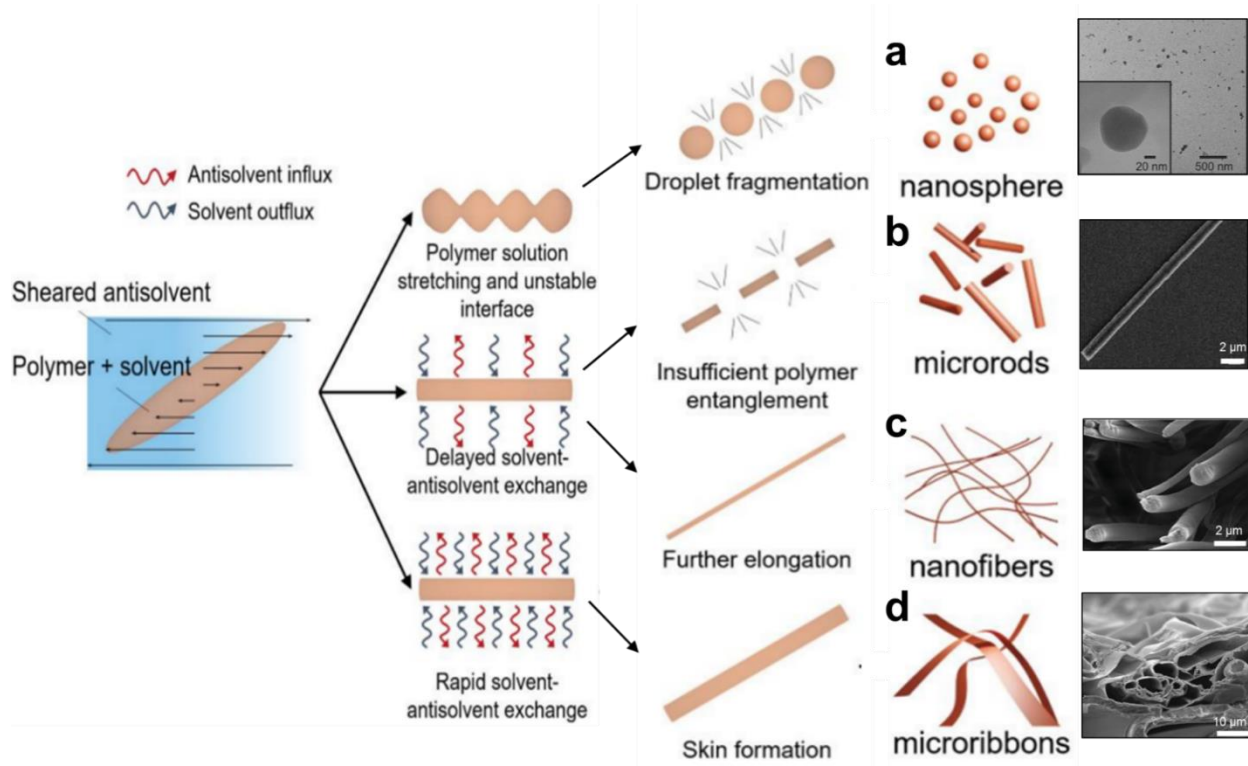


**Figure 1.3.** Polymer particle morphologies resulting from shear-driven polymer precipitation in laminar nonsolvent flows. (a) Lignin nanoparticles produced by flash precipitation of lignin solution into a water nonsolvent.<sup>24</sup> (b) SU-8 polymer microrods produced by liquid-liquid shear.<sup>60,61</sup> (c) Polystyrene nanofibers produced by in a laminar flow using a Couette cell.<sup>62</sup> (d) Polystyrene micro-ribbons produced by increasing the precipitation rate within a laminar nonsolvent flow.<sup>62</sup>

The transition of the nonsolvent flow from laminar to turbulent flow regime enables the production of new particle morphologies. As the nonsolvent shear increases into the turbulent regime and produces multi-scale vortices<sup>63</sup>, the particles resulting from shear-driven polymer precipitation begin to exhibit branched structures. We hypothesize that the transition from unidirectional to branched fibers occurs at a certain critical Reynolds number value ( $Re$ , Equation 1.2), where  $\rho$  is the density of the nonsolvent and  $D$  is the diameter of the tube.

$$Re = \frac{\rho V D}{\mu} \quad (\text{Equation 1.2})$$

We have estimated that this transition from laminar to turbulent flow and the subsequent change in shear-based precipitated particle morphology to branched-fibers occurs around a  $Re \approx 1,500$ . This is consistent with fluid dynamic studies that estimate that the transition from laminar to turbulent flows occur at a  $Re$  range of 2,000 – 4,000.<sup>64</sup>

Polymer precipitation templated in a turbulent flow can produce many different particle morphologies including soft dendritic colloid (SDC) and nanosheet (NS) particulates (Figure 1.4a).<sup>65</sup> While the multitude of thermodynamic and mechanical phenomena involved in the turbulent precipitation process make it difficult to model precisely or predict the resulting particle morphology, the concentration of polymer in the injected solution and the rate of precipitation are key factors in determining the structures of the resulting particulates. High polymer concentrations and rapid solvent-nonsolvent demixing evidenced by small one-phase regions in ternary phase diagrams yield particles with more sheet-like and less fibrous structures, while systems with larger one-phase regions and delayed precipitation produce SDCs (Figure 1.4b).<sup>56,65</sup> To produce these designer particulates, the time-scale of the interfacial deformation of the injected polymer solution droplet must be balanced with the time-scale of precipitation induced by the nonsolvent phase. Modulation of the precipitation rate results in the general trend of changing the particle morphologies from nanoparticles to SDCs to NSs, as shown in Figure 1.5. It is thought that the stochastic, fractal eddy formation within a turbulent flow is responsible for the hierarchical pattern of the polymer droplet during precipitation.<sup>66</sup> The nanofibrillar corona of SDCs readily forms an interparticle, physical adhesive network of sub-contacts that results in the gelation of SDC suspensions at low concentrations. This characteristic of SDCs has already been utilized to prepare composites in thermoelectric films with low filler content.<sup>67</sup>

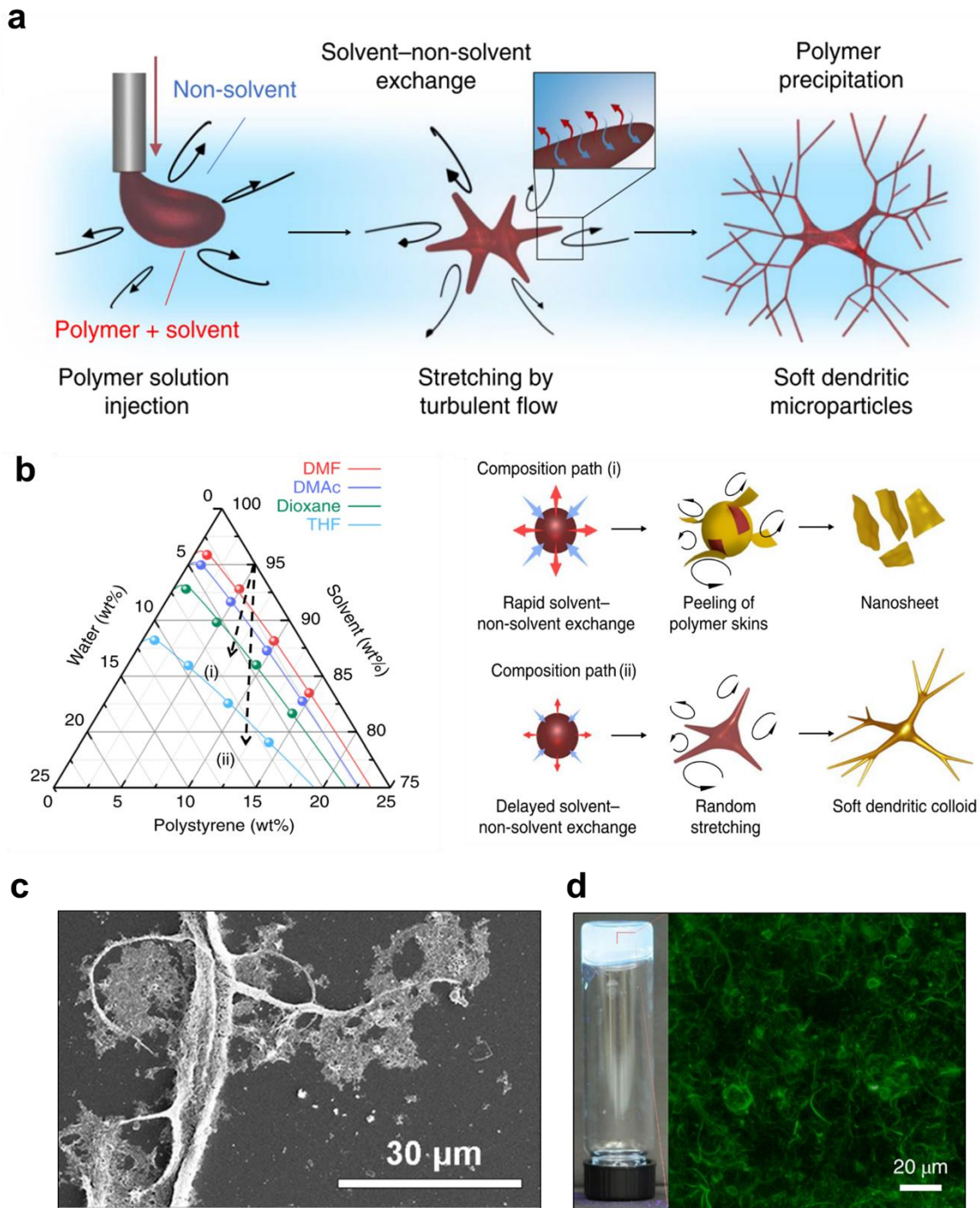


**Figure 1.4.** Fabrication and properties of soft dendritic colloids. (a) Schematic of the turbulent, nonsolvent-induced phase separation technique to first produce SDCs.<sup>65</sup> (b) Ternary phase diagram illustrating the formation of nanosheets in systems with rapid precipitation evidenced by a small one-phase region and SDC formation in systems with delayed precipitating and a large one-phase region. (c) Electron micrograph of PVDF SDCs utilized in free-standing composites for thermoelectric generation.<sup>67</sup> (d) a 1.0 vol.% cellulose acetate SDC suspension in mineral oil and a fluorescent confocal micrograph visualizing interparticle networking of SDCs.<sup>65</sup>

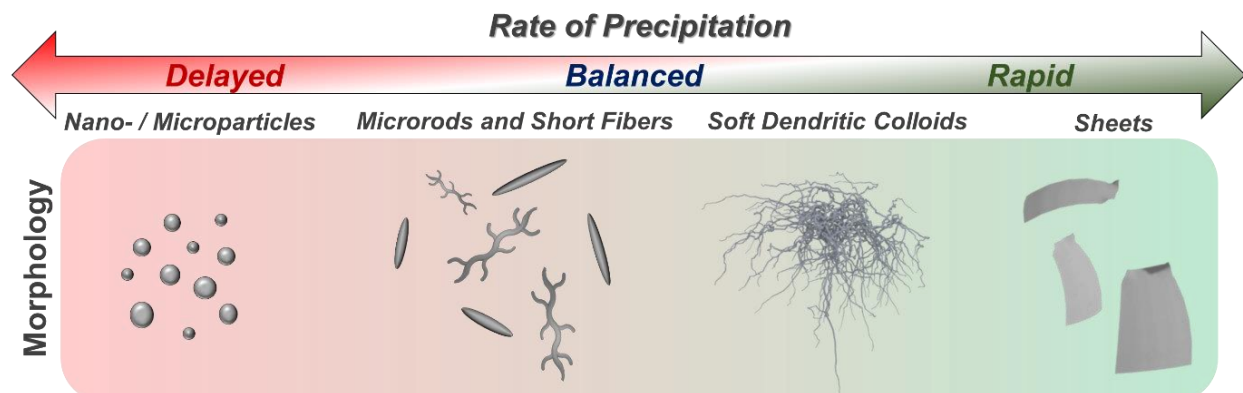


**Figure 1.5.** The role of precipitation rate in governing the particle morphologies formed during turbulent shear-driven polymer precipitation allowing production of a broad range of materials from nanoparticles to nanosheets.

Shear-based polymer precipitation is a highly scalable nanomanufacturing technique and its compatibility with a multitude of different polymer chemistries makes it very suitable for future technology development. One major advantage of the technique is the production of SDC and other particle morphologies in liquid suspension. Other nanofiber production techniques either produce dry fibers that are confined to a 2D mat, as is commonly the case with nanofibers production techniques, or they require expensive post-processing techniques as is the case with naturally-derived fibers like fibrillated cellulose.<sup>5</sup> Unlike the majority of other polymer fiber fabrication techniques, the SDCs are inherently produced in suspension which allows their facile re-suspension in media of another composition. Furthermore, the simple filtering of SDC suspensions yields highly fibrous and porous SDC membranes of controlled thickness and can be layered to produce Janus SDC materials.<sup>65</sup>

## 1.5 Polyelectrolyte complexation and layer-by-layer film nanoassembly

Polyelectrolytes are water-soluble polymers with charged, ionic functional groups located on the backbone of each repeating monomer in the molecular chain. Upon their mixture, polyelectrolytes with positively-charged functionalities, or polycations, will rapidly complex with negatively-charged polyelectrolytes, or polyanions, to form polyelectrolyte complexes (PECs, Figure 1.6a). By sequentially dipping a substrate into molecular solutions of oppositely charged polyelectrolytes, the complexation reaction between the two species can be confined to the substrate's surface to form nano-scale polyelectrolyte multilayers (PEMs, Figure 1.6b). This common technique is known as layer-by-layer deposition (LbL).<sup>32,68</sup> LbL is an easy to implement and versatile technique that can rapidly coat substrates of any surface topography with polymer films of controlled thickness and chemistries for applications in antireflective films, hollow microcapsules, biosensors, optics, and barrier coatings.<sup>35</sup> Polyelectrolyte complexation can also be templated within a fluid flow generated by concurrent electrospinning of both polyelectrolytes to produce PEC composite fibers (Figure 1.6c).<sup>69</sup>

The molecular architecture and the intermolecular interactions that build up the PEM govern the mechanical and self-healing features of the resulting polymer film.<sup>70</sup> PEMs incorporating hydrogen bonding in addition to ionic bonding into the molecular network typically exhibit lower mechanical moduli and greater elasticity.<sup>71,72</sup> It has been shown on the basis of several polyelectrolyte systems that the pH values of both polyelectrolyte solutions are the primary factor governing the PEM growth rate and that this growth rate is maximized when each polyelectrolyte is weakly charged in its respective solution.<sup>73-75</sup> In highly charged states, polyelectrolytes adopt more linear conformations due to electrostatic repulsion between their

charged groups. Weakly charged polyelectrolytes generally adopt coiled conformations as the degree of electrostatic repulsion is reduced and intramolecular hydrogen bonding can occur.<sup>76</sup>

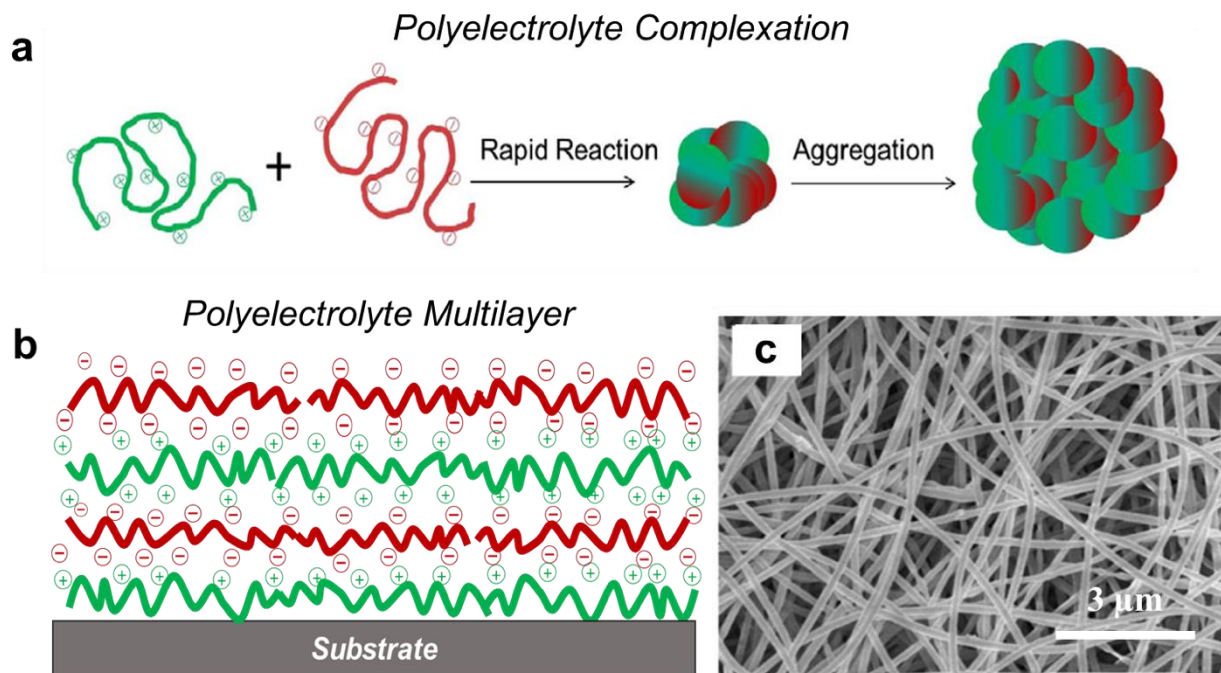


**Figure 1.6.** Schematics of polyelectrolyte composite materials. (a) Formation of self-assembled PECs by oppositely charged polyelectrolyte solutions.<sup>32</sup> (b) Confining the complexation reaction to the surface of a wafer sequentially dipped in oppositely charged polyelectrolytes to build a PEM using layer-by-layer deposition. (c) Electrospun chitosan-alginate nanofiber web prepared by *in situ* complexation.<sup>69</sup>

PEM nanocoatings with high oxygen barrier properties that are also elastic enough to withstand strain of the bulk material without sacrificing the barrier are of considerable interest. Synthetic polycation branched polyethyleneimine (BPEI) and polyanion polyacrylic acid (PAA) form a PEM with an impressive oxygen barrier properties, however, their primarily ionic film architecture is brittle and incapable of resisting strain without cracking.<sup>77</sup> Incorporating inorganic nanosheets into the polymer coating improves the coating tortuosity and barrier resistance, but ceramic additives do not improve the stretchability of the coating.<sup>78</sup> By deliberately adding another

polyethylene oxide (PEO) layer into the BPEI – PAA systems to form a BPEI – PAA – PEO quad-layer, hydrogen bonding can enable PEMs with strong gas barriers and flexibility.<sup>71,79</sup>

Biopolymers are attractive materials for applications in coatings and packaging because they can be sustainably sourced and utilized to replace common polyolefin materials in single-use applications.<sup>80</sup> Chitin and alginate are two naturally-occurring polysaccharides that are derived from crustaceous shells and algae, respectively.<sup>81</sup> Chitin can be further processed by deacetylation (~70 – 85%) to yield chitosan and leave ionically-active primary amine functionalities.<sup>82</sup> While the resulting amine groups are free to interact with a negatively charged groups on polyanions like alginate, the incomplete deacetylation of chitin leaves acetylated groups capable of engaging in hydrogen bonding on the polysaccharide backbone.<sup>83</sup> Chitosan and alginate have been deployed as packaging coatings, in direct food coatings, and as self-standing PEM films, but these efforts have not been optimized to maximize the chitosan – alginate nanocoating growth, and have not characterized or quantified the optimized coating's mechanical properties or permeability.<sup>84-89</sup>

## **1.6 Layout of this dissertation**

The shear-driven polymer precipitation technique has exceptional promise to scalably produce designer nanomaterials from a huge number of polymer and biopolymer matrixes. My thesis research presented here sought to identify and analyze the parameters that govern the morphological features of the particles resulting from shear-driven polymer precipitation as well as to find specific applications for SDCs. Chapter 1 introduces nanomaterials and common techniques by which they are fabricated, and a background of their applications as composite reinforcement materials, adhesives and coatings, and nonwovens. In Chapter 2, the precipitation mechanisms that can be utilized to produce all types of SDCs, including hydrogel SDCs (hSDCs) and polyelectrolyte composite SDCs (cSDCs) are explored and the characteristics of their aqueous suspensions are analyzed by rheometry. Then, we further investigate the rheological behavior of alginate hSDCs and utilize them as the reinforcement material in a continuous hydrogel molecular alginate matrix to produce a new class of “homocomposite” hydrogels. In Chapter 3, we explore how SDCs can be simply filtered to produce highly porous membranes and how the bulk mechanical and physical properties of SDC membranes can be modulated by altering the morphologies of the particles comprising the bulk material for applications in bioscaffolds and lithium ion battery separators. In Chapter 4, the highly adhesive properties of SDCs are utilized to prepare surface coatings. The wetting and anti-icing properties of SDC coatings, are investigated as a function of the polymer comprising the SDCs. Finally, the growth and application of a nano-scale biopolymer coating is explored in Chapter 5. The parameters governing the growth of chitosan – alginate polyelectrolyte layer-by-layer coatings are investigated and their application as a food-grade oxygen barrier is examined.

**CHAPTER 2: Biopolymer Soft Dendritic Colloids and Self-Reinforced Homocomposite  
Hydrogels with a Molecular-Colloidal Double Network**

## 2.1 Introduction

Naturally-derived polymer materials are of significant academic and commercial interest to due in the shift to replace single use polyolefin materials. Sodium alginate (SA or Alg) and chitosan (CS) are two biologically-derived polysaccharides. The ionic functionalities on the backbone of Alg and CS will rapidly complex with multivalent calcium and citrate molecules to form cross-link networks and water-swollen hydrogels.<sup>81,90</sup> Upon their mixing, the opposing charges of polycationic chitosan and polyanionic alginate will readily interact to form ionically-bound polyelectrolyte complexes.<sup>35,91</sup> Biocompatible materials like Alg and CS biopolyelectrolyte complexes have even found application as nanomaterials for the controlled release of pharmaceutical applications.<sup>92</sup>

Hydrogels made of polymer networks in water are generally soft and brittle, often lacking the resilience and toughness required for widespread deployment in applications such as tissue scaffolds, food products, soft robotics, and flexible electronics.<sup>93–101</sup> The elasticity of these materials can be improved by combining interpenetrating covalent and ionic polymer networks to form highly stretchable and tough hydrogels.<sup>102–108</sup> Another way of improving and enhancing the mechanical properties of hydrogels is by including high aspect ratio fillers, such as fibers, to mechanically reinforce the gel matrix.<sup>15,49,109–115</sup> Fiber-reinforced hydrogels can serve as comprehensive bioscaffolds for cell growth. The fiber networks offer robust control of hydrogel stiffness, and can mimic the morphology of the physiological extracellular matrix, which has been shown to affect cell activity, differentiation and response.<sup>116,117</sup> Controlling hydrogel stress propagation by fiber reinforcement is also useful in applications such as soft robotics, as it may enable nonlinear deformation modes and durability against frictional sliding.<sup>118</sup> However, using fillers made of a different material from the matrix introduces stressed interfaces that cause crack formation when the composite hydrogels are strained or heated.

One different materials design approach is to use single-polymer composites, or so-called homocomposites. The mesoscale reinforcement network of homocomposites is made of a material that is chemically identical to that of the primary matrix. Homocomposite reinforcement networks allow modulation of the mechanical properties of the host matrix without stress concentrations, delamination points or other problems arising from interfacial incompatibilities.<sup>46,119</sup> Homocomposite formulations have also been designed using elastomer particles bound by capillary bridges of the precursor liquid elastomer in multiphasic silicone pastes for 3D printing.<sup>120,121</sup> The chemical similarity of the continuous and reinforcement phases provides superior adhesion and enhanced load transfer.<sup>115,122–124</sup> Previous studies have also shown that homocomposites with fiber reinforcements allow tailored bulk melt rheology along with increased tensile modulus and strength.<sup>125,126</sup> They are made by using the differences in melting temperatures between thermoplastic polymer crystalline phases as a processing window.<sup>127,128</sup> However, homocomposite hydrogels (HHGs) remain challenging to fabricate because of the lack of techniques to construct reinforcing networks with the same chemical composition as the hydrogel matrix.

We report a class of HHGs where both the primary gel matrix and the reinforcement network are made of sodium alginate. Alginate hydrogels are used in a broad range of technological applications such as biomedical implants, tissue engineering scaffolds, and food products.<sup>81,129</sup> These HHGs are reinforced by a fibrillar network of alginate soft dendritic colloids (SDCs). The SDCs are a hierarchically structured class of soft matter synthesized through a scalable process of shear-driven precipitation in a turbulent medium, described in our recent report.<sup>65</sup> The high degree of branching around the cores of the SDC particulates makes them morphologically similar to polymeric molecular dendrimers, but SDCs are orders of magnitude

larger than these dendrimers.<sup>130,131</sup> Our previous studies with polymer SDCs dispersed in an organic oil medium showed that the branched, nanofibrous structure of the dendricolloids enables efficient network formation leading to gelation at low volume fraction due to enhanced van der Waals interactions.<sup>65,132</sup>

The hierarchically branched SDCs are expected to serve as efficient reinforcement in composite materials. Their branches provide large surface area, which could increase the composite stability by distributing the stress more uniformly.<sup>54,65,133–136</sup> We investigate here the SDC's effectiveness in reinforcing homocomposite hydrogels, expecting that the high surface area and maximized adhesiveness between the SDC network and the matrix will result in hydrogels of outstanding mechanical properties. To analyze the unusual mechanical properties of the HHGs, we also perform shear and tensile tests on their individual constituents: aqueous SA SDC suspensions and crosslinked SA molecular hydrogels (CMHs). We then characterize HHGs composed of SA SDCs embedded in a SA CMH matrix and discuss the origins of their synergistically enhanced viscoelastic properties. On this basis, we demonstrate that the HHGs can be readily formulated to provide a yield stress for 3D printing or pressure-driven extrusion.

## 2.2 Materials and Methods

### 2.2.1 Fabrication and characterization of SDCs, hSDCs, and cSDCs

Alginic acid sodium salt (SA or Alg, Sigma, 120-190 kDa) was dissolved at 3 wt.% in distilled water (Millipore) and chitosan (CS, low molecular weight, Sigma-Aldrich) was dissolved at 3 wt.% in 1.5 vol.% acetic acid (Alfa Aesar) in water (Millipore) and both stock solutions stored at 4°C. To fabricate SA SDCs, a colloidal high-shear mixer (IKA Magic Lab) was first filled with 500 mL of calcium ion ( $\text{CaCl}_2 \cdot 2\text{H}_2\text{O}$ , Sigma-Aldrich) or sodium citrate (NaCit, Fisher) precipitation medium. Prior to particle fabrication, SA and CS solutions were diluted to the desired concentration using water and 1.5 vol.% acetic acid, respectively. A volume of 20 mL of SA or CS solution was injected directly into the shear zone of the device at 20,000 rpm using a machined injection attachment, where the particles form nearly instantaneously and are left suspended in the precipitation medium. Solvent and nonsolvent compositions are listed in Figure 2.2. Particle suspensions were centrifuged for 3 minutes at  $3.0 \times 10^3$  xg, resulting in the formation of a concentrated pellet. The compacted SDCs were then re-suspended to 8× their pellet volume in distilled water using a Vortex mixer. This process was repeated 5× to remove any remaining ions from the suspension. Following particle washing, the SDCs were centrifuged and diluted to their desired concentration. Particle morphologies were visualized using optical microscopy (BX-61 Olympus) and field emission scanning electron microscopy (FEI Verios 460L scanning electron microscope). Images were processed using ImageJ to adjust brightness and contrast.

### 2.2.2 Fabrication/Synthesis/preparation of the molecularly crosslinked SA hydrogels

Conventional CMHs were prepared by adding 0.1 wt.%  $\text{CaCO}_3$  nanoparticles (NPs, 10 – 80 nm, American Elements®) and 28.14 mM solution of D-Gluconic acid  $\delta$ -lactone (GDL, Sigma-Aldrich) to an aqueous SA solution.<sup>137</sup> Upon dissolution in water and addition to the alginate mixture, GDL

slowly hydrolyzes, reducing the pH and gradually ionizing the  $\text{CaCO}_3$  NPs to release  $\text{Ca}^{2+}$  crosslinker ions.<sup>138</sup> This is preferred over the addition of instantly soluble Ca salt (like  $\text{CaCl}_2$ ) since it allows more homogeneous SA gel formation.

### 2.2.3 Preparation of alginate homocomposite hydrogels

Alginate molecular/SDC gels were made by first preparing stock solutions of 3.0 wt.% SA in water, mixed with 0.30 wt.%  $\text{CaCO}_3$  nanoparticles, and 1.38 wt.% SA SDCs in water to reach the desired concentrations and stirred thoroughly. To induce homogenous gelation, freshly prepared 20 wt.% D-(+)-gluconic acid  $\delta$ -lactone in water was added to the mixture at a ratio of 5/1 (GDL/ $\text{CaCO}_3$  w/w) and homogenized using a Vortex device. All gels were given 2 hours to complete crosslinking prior to characterization. The final concentrations of each constituent of HHGs are shown in Table A1.

### 2.2.4 Rheological and tensile characterization of suspensions and hydrogels

The viscoelastic properties of the SDC suspensions and HHGs were evaluated using a rheometer (Discovery HR-2, TA Instruments) equipped with a sandblasted plate and plate geometry (40 mm diameter and 0.8 mm gap size) with the temperature maintained at 25°C for all experiments. Small amplitude oscillatory frequency sweeps were performed within the linear viscoelastic regime. Amplitude sweeps were performed between 0.1 and 1000% strain at a frequency of 6.23 rad/s and time sweeps were performed at a frequency of 1 rad/s with 1% strain. The tensile properties of the gels were determined using a common testing machine (Instron 5943) with samples of 1.5 mm thickness, 44 mm width, 10 mm length, and a 5  $\text{cm}\cdot\text{min}^{-1}$  crosshead speed. Laser-cut acrylic molds were used to shape hydrogels during equilibration and laser-cut acrylic grips were used for tensile analysis to avoid directly gripping the hydrogel sample. A thin layer of cyanoacrylate adhesive

(Gorilla Glue Gel) was used for chemically bonding the gel to the grips to ensure that slippage did not occur during extension (Figure A10).

#### 2.2.5 X-ray photoelectron spectroscopy measurements

XPS measurements were performed using a SPECS FlexMod instrument with Mg  $k\alpha$  excitation (1254eV). A hemispherical PHOIBIS 150 analyzer was use with a takeoff angle normal to the surface, a 30° X-ray incidence angle, and a 60° angle from X-ray source to analyzer. Energy calibration was established by referencing to adventitious Carbon (C1s line at 285.0 eV binding energy) and the base pressure in the analysis chamber is in  $10^{-10}$  mbar range.

## 2.3 Results

### 2.3.1 Polymer nanomaterials fabrication by precipitation within turbulent liquid shear

The three precipitation mechanisms compatible with the shear-driven polymer precipitation technique presented here are nonsolvent-induced phase separation to form SDCs, ionic hydrogel cross-linking to form hydrogel SDCs (hSDCs), and polyelectrolyte complexation to form composite SDCs (cSDCs). Schematics showing the production of the characteristic SDC morphology by these three precipitation mechanisms are shown in Figure 2.1. The distinct control of resulting particle morphologies is shown with each precipitation mechanism in Figure 2.2. The three primary parameters – hydrodynamic shear, polymer concentration, and precipitation rate – are highly generalized because they are difficult to decouple experimentally. Furthermore, it is difficult to quantitatively compare rates of precipitation affected by different mechanisms. Nevertheless, the proper modulation of these three aspects in one system can produce particle morphologies ranging from nanoparticles to very thin polymer nanosheets.

While the production of hydrogel and composite particles is shown with the biopolymers alginate and chitosan here, the SDC fabrication process is not limited to these types of biopolymers and SDCs can be produced with synthetic polyelectrolytes as well (Figure 2.5). While SDCs, hSDC, and cSDCs are morphologically similar with all having branched-fiber structures, they show distinct behavior due to the different precipitation mechanisms by which they are produced. The SDC morphology is the most interesting particle feature, as the interparticle networking and suspension structuring is maximized in particles with hierarchical morphologies when measured by rheometry (Figure 2.3a-b, Figure 2.4b). Furthermore, in aqueous suspension, alginate hSDCs show greater suspension structuring than alginate SDCs due to their swollen hydrogel composition

compared to highly dense SDC fibers (Figure 2.3d). Polyelectrolyte hSDCs and cSDCs show additional ionic and pH-responsive behavior (Figure 2.3c, Figure 2.4c-d).

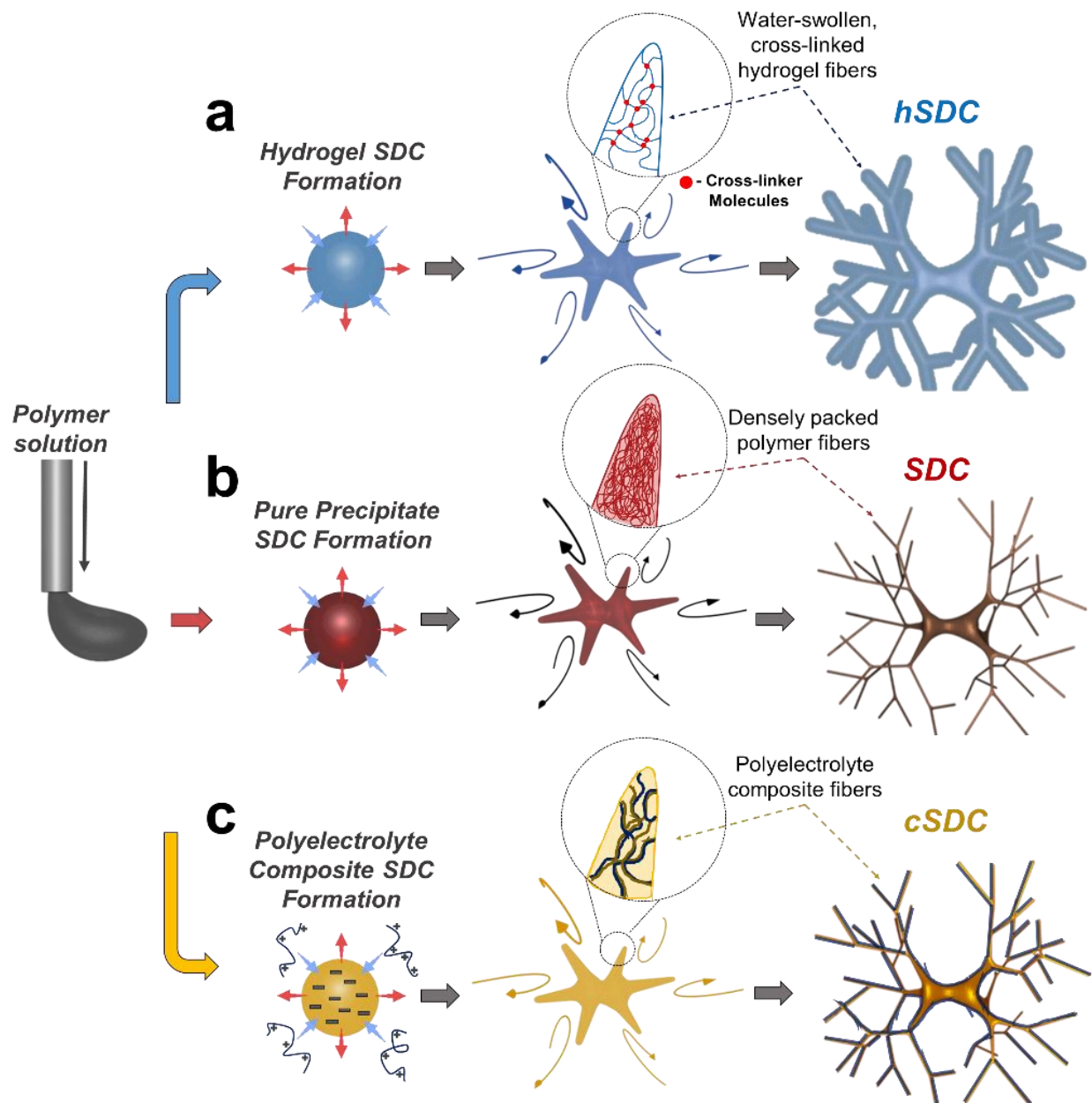


**Figure 2.1.** Precipitation mechanisms utilized for producing nanofibrillated soft dendritic colloids. Injection of a polymer solution for into a turbulent nonsolvent flow for (a) Hydrogel SDC formation by a rapid cross-link reaction in an aqueous nonsolvent, (b) Pure polymer precipitate SDC formation by nonsolvent-induced phase separation<sup>65</sup>, (c) an oppositely-charged polyelectrolyte solution to produce polyelectrolyte composite SDCs.

The shear-based polymer precipitation nanomanufacturing technique enables the fabrication of multiple different colloidal particle morphologies from several different polymer compositions. Applying concurrently a turbulent nonsolvent flow can result in the particle morphologies shown in Figure 2.2a, ranging from nanoparticles and other “chunks” in systems with low polymer entanglement and delayed precipitation rates to soft dendritic colloids to polymer nanosheets in systems with significant entanglement and rapid precipitation. Because many different precipitation mechanisms are compatible with this technique, morphologically similar particles from different systems can be produced. To highlight this, the biopolymers sodium alginate (SA or Alg) and chitosan (CS) were used to prepare hSDCs using a hydrogel ionic cross-link mechanism (Figure 2.2b-c), SDCs from an organic nonsolvent-induced phase separation mechanism (Figure 2.2d-e), and Alg – CS cSDCs using a polyelectrolyte complexation mechanism (Figure 2.2f, Figure A1). Particles fabricated using the different precipitation mechanisms may show morphological similarity, but each particle may exhibit different behaviors depending on both its polymer chemistry and its morphology.

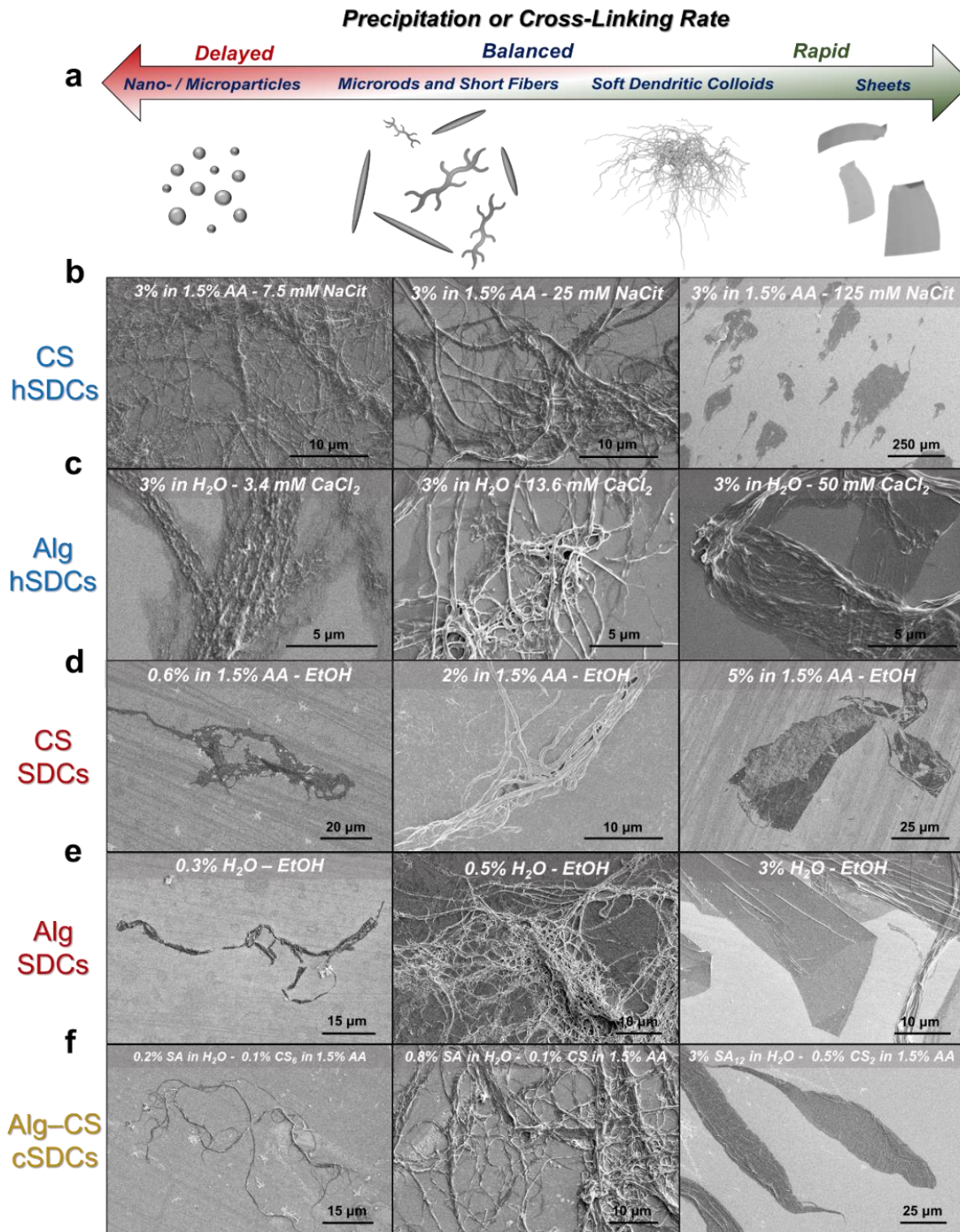


**Figure 2.2.** Controlling morphology of biopolymer particles by turbulent shear-based precipitation. (a) Scheme showing the general trend of particles produced by shear-driven precipitation within a turbulent flow by changing precipitation rate and mechanism for producing each morphology of (b) chitosan hSDCs, (c) alginate hSDCs, (d) chitosan SDCs, (e) alginate SDCs, and (f) alginate-chitosan polyelectrolyte composite cSDCs.

Analyzing aqueous suspensions of Alg and CS hSDCs using rheometry, we show that the SDC morphology optimizes the physical networking in equally concentrated suspensions both in alginate and chitosan systems (Figure 2.3a-b). These results help illustrate how by varying the concentration of cross-linker molecules in the nonsolvent phase and thereby modulating the precipitation rate, the morphology of the resulting particulates can be easily tuned to optimize their function for applications as suspension viscosity modifiers. Moreover, both the SA and CS systems show that the NS morphology can't quite achieve suspension structuring analogous to the one of the SDCs, but these particles still exhibit impressive structuring enabled by their high aspect ratios.

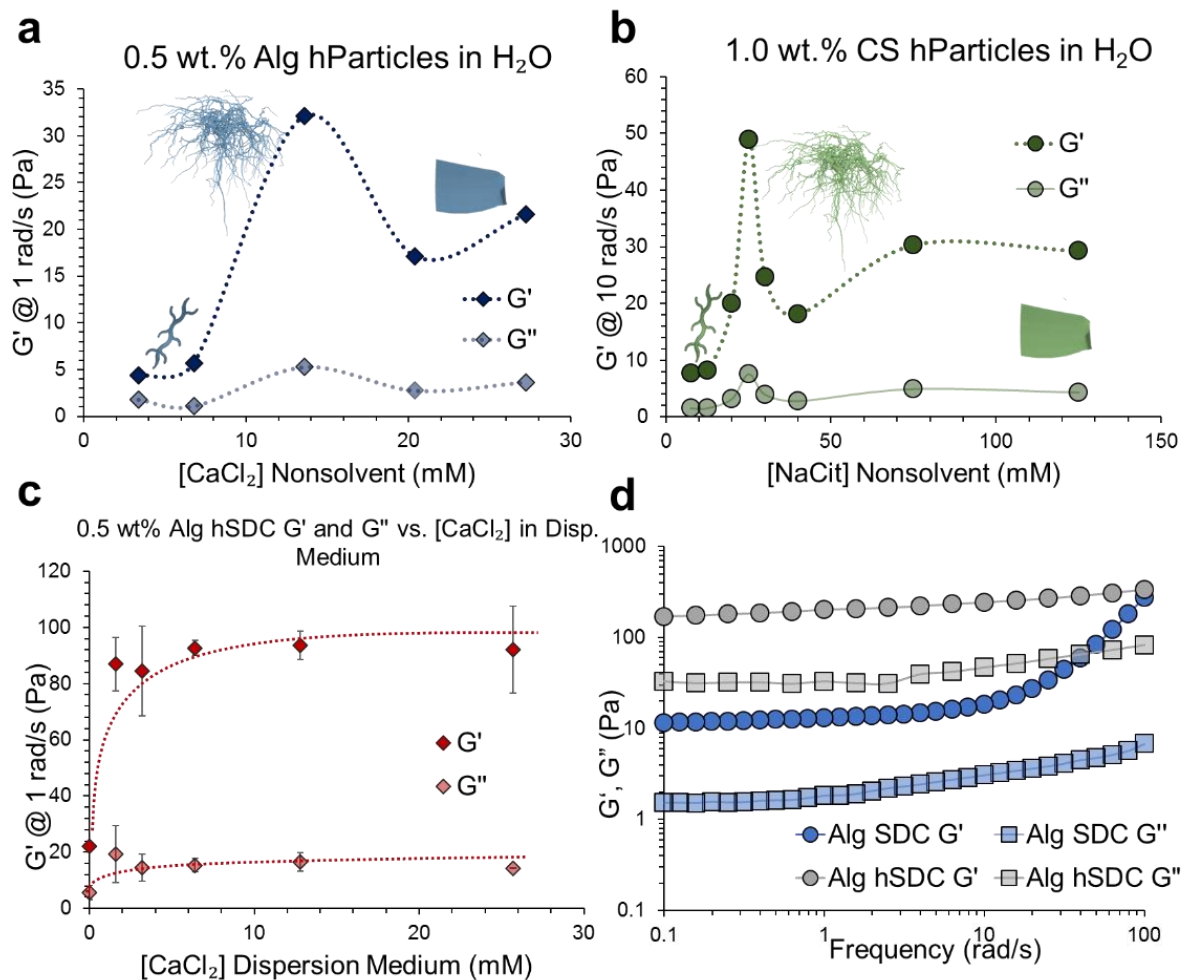


**Figure 2.3.** Suspension structuring of particles produced by shear-driven precipitation. (a-b) Storage moduli at  $1 \text{ rad}\cdot\text{s}^{-1}$  from frequency sweeps of suspensions in their respective nonsolvent media for (a) 0.5 wt.% Alg hSDCs with aqueous  $\text{CaCl}_2$  nonsolvent and (b) 1.0 wt.% chitosan hSDCs with aqueous NaCit nonsolvents of varying concentrations. (c) Storage and loss moduli from frequency sweeps of 0.5 wt.% Alg hSDCs (13.6 mM  $\text{CaCl}_2$  nonsolvent) dispersed in aqueous solutions of varied  $\text{CaCl}_2$  concentrations. (d) Frequency sweeps of 1.0 wt.% suspensions comparing Alg SDCs to hSDCs.

Alginate hSDCs retain surface charge as evidenced by the strong dependence of their suspension structuring on the suspension's salt concentration. To highlight this effect, 0.5 wt.% Alg hSDCs were washed thoroughly with deionized water and re-suspended in aqueous media of varied  $\text{CaCl}_2$  concentration. Frequency sweeps of each of the resulting Alg hSDC suspensions (Figure 2.3c) indicates that in deionized water, the Alg hSDCs show greatly reduced networking

in suspensions ( $G' = 20$  Pa) compared to any of the systems with added  $\text{CaCl}_2$ . This effect suggests that the alginate hSDCs retain some surface charge activity. In pure water, these charged fibers exhibit electrostatic repulsion that inhibits the structuring and network formation of those hSDCs. With the addition of just 1.25 mM  $\text{CaCl}_2$  to the suspension, the storage modulus increases over four-fold ( $G' = 85$  Pa), suggesting that the addition of these ionic species may effectively screen the charges of the hSDC fibers and mitigate repulsion between fibers.

To compare the suspension structuring ability of Alg hSDCs and SDCs, two aqueous suspensions of each alginate particle were prepared. Alg SDCs were prepared by precipitation into an ethanol as nonsolvent medium followed by the addition of  $\text{CaCl}_2$  to the ethanol suspension to cross-link the SDCs. The cross-linked SDCs were then washed and re-suspended in water without dissolving. In Figure 2.3d, it is shown that both suspensions exhibit gel-like behavior, however, the 1.0 wt.% Alg hSDC suspension has a storage modulus an order of magnitude larger than the Alg SDC suspension. The ionic cross-link mechanism that produces hSDCs may result in water-swollen hydrogel hSDC fibers that form more effectively networks in suspension compared to the more densely-packed SDC fibers.

The optimization of suspension networking by the SDC morphology is again seen in Alg-CS polyelectrolyte composite cSDCs. Because cSDCs are comprised of ionic interactions between these oppositely-charged polyelectrolytes, we believe that the resulting fibers exhibit degrees of amphiphilic or zwitterionic behavior (Figure 2.4a). This property of cSDCs leads to highly adhesive behavior even in suspension, with these particles strongly adhere to any surface surrounding their suspension. The adhesive effect introduced by this unique fiber chemistry may help explain the significantly elevated storage moduli of 1.0 wt.% cSDC suspensions (Figure 2.4b), with values greater than an order of magnitude larger than Alg hSDCs. Nevertheless, again the

cSDC morphology shows increased structuring compared to Alg-CS composite microrod particles (cRods) and nanosheets (cSheets). Zwitterionic fiber chemistry would also explain the pH-responsive behavior of cSDCs when suspended in a 0.01 M PBS buffered solution. An increase in the solution pH from 6.5 to values above 8.0 result in the conformational collapse of the cSDC and a subsequent reduction network structuring and solution opacity as the aggregated cSDC fibers less effectively scatter light (Figure 2.4c-d).

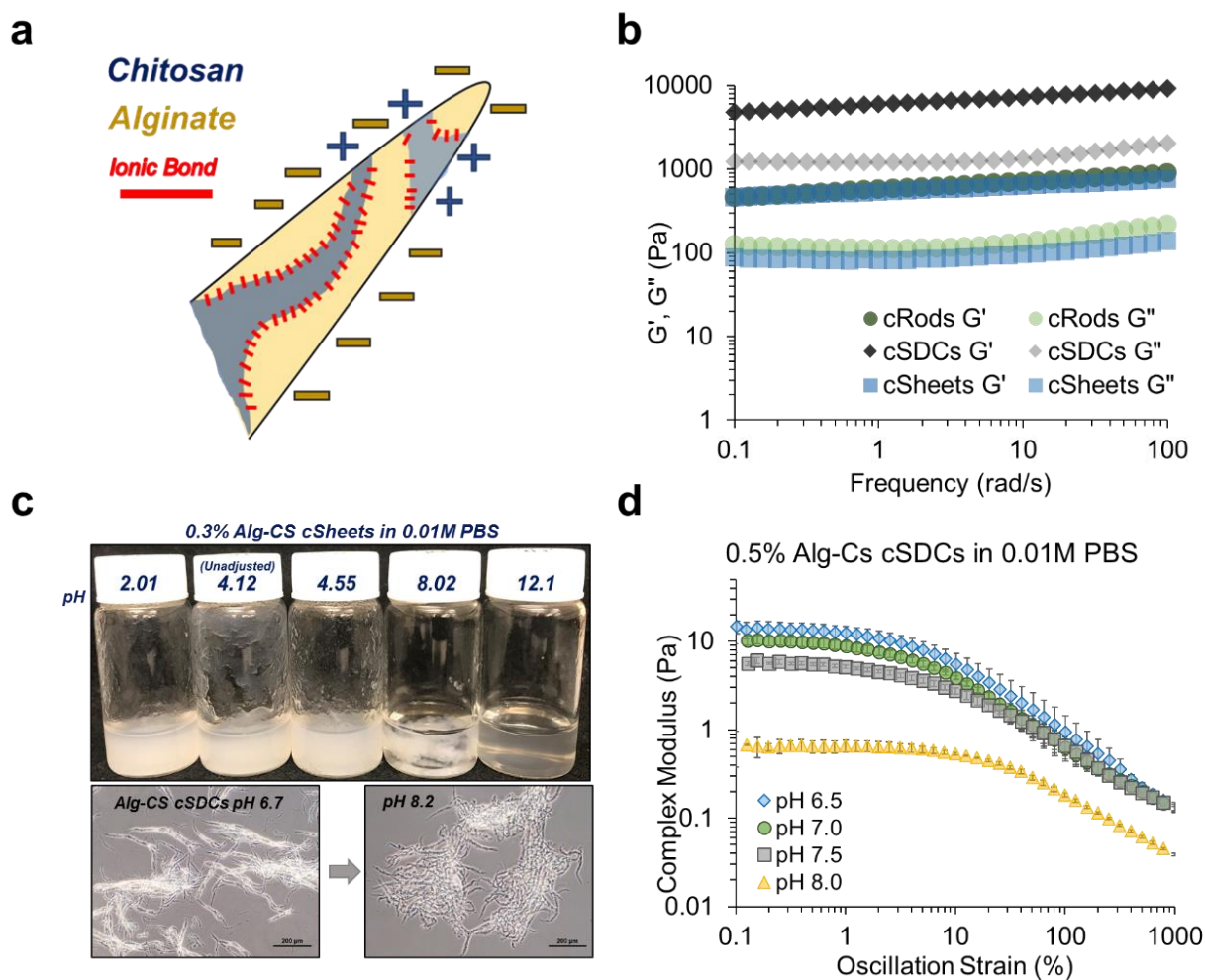


**Figure 2.4.** Polyelectrolyte cSDCs and their pH-responsive behavior. (a) Scheme illustrating the pH-responsive behavior of Alg-CS composite particles. (b) Frequency sweeps performed on 1.0 wt.% suspensions of Alg-CS cRods, cSDCs, and cSheets in H<sub>2</sub>O. (c) Pictures of 0.3 wt.% Alg-CS cSheet suspensions in 0.01M PBS with varying pH and microscope images of cSDC changing conformation from pH 6.7 to pH 8.2 (c-d) Amplitude sweeps of 0.5 wt.% suspensions of Alg-CS cSDCs in 0.01M PBS with varying pH.

### 2.3.2 Characterization of hydrogel soft dendritic colloids from alginate

In order to obtain the hydrogel alginate hSDCs (hereafter referred to as SDCs) used as reinforcement networks, a solution of alginate was injected in an aqueous solution of  $\text{Ca}^{2+}$  ions, which effectively bind and crosslink two  $-\text{COO}-$  side groups on the alginate backbone (Figure 2.5a).<sup>65</sup> The turbulent shear precipitation process results in SDCs with characteristic hierarchical morphology, illustrated in Figure 2.5b, with multiscale branching and generations of fibers spanning roughly 3 orders of magnitude in length scale. SDCs consist of micron-scale fibers that branch multiple times into ever thinner fibers. The outermost layer surrounding each SDC, or so-called “corona,” encompasses flexible nanofibers that can be as thin as 10 nm (Figure 2.5b). The nanofibers in the coronae endow them with physical adhesiveness, which is a major factor in the dendricolloids’ ability to build the structural strength of the colloidal network. The effective overall size of common SDCs, including their coronae, is in the 100-500  $\mu\text{m}$  range. The macroscopic features and properties of the SDCs and their suspensions are consistent across bulk measurements (for more details see Figure A2 & A3). The SA SDCs suspensions were washed with deionized water to remove excess  $\text{CaCl}_2$  ions from the suspension.

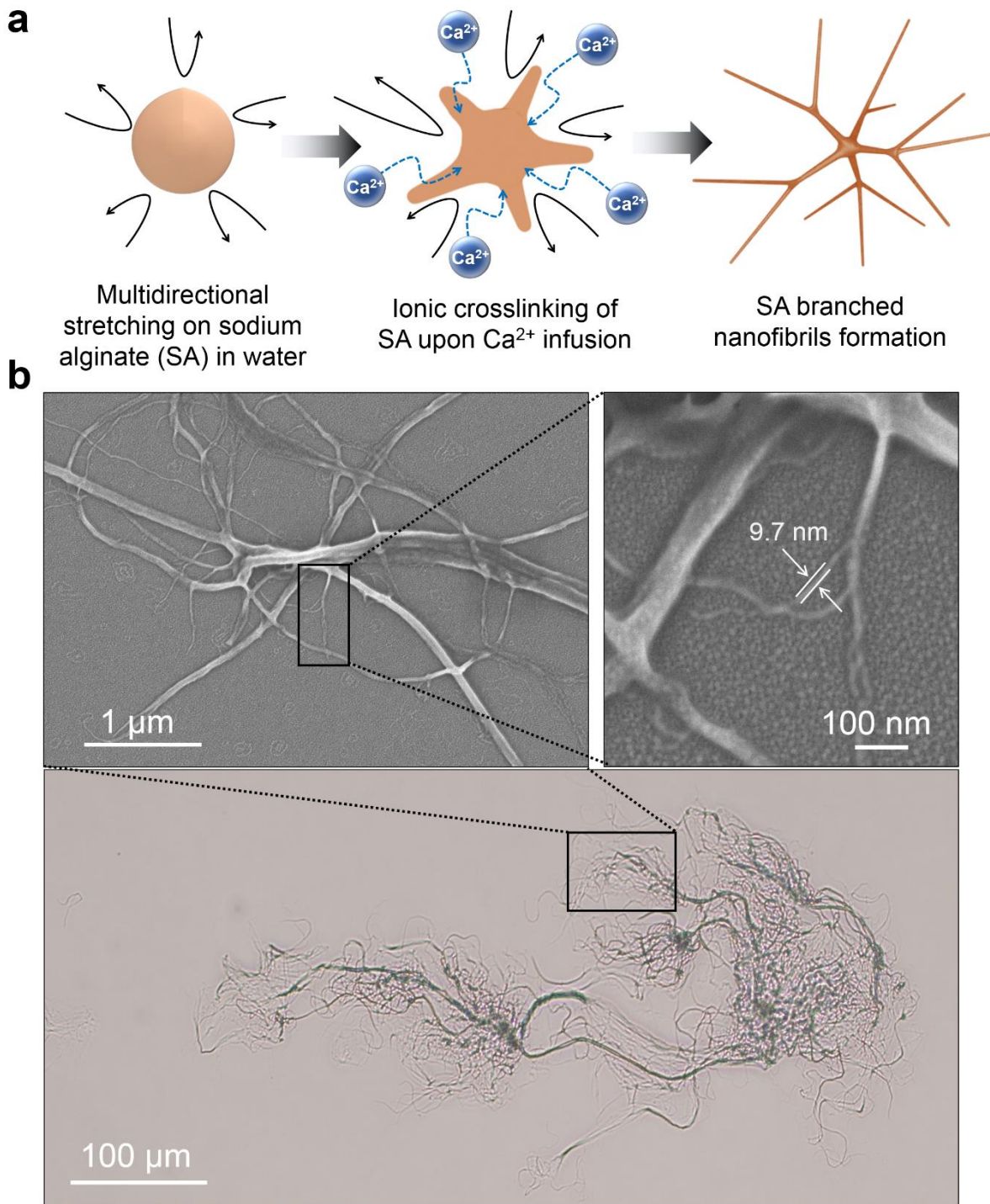


**Figure 2.5.** Turbulent shear-driven precipitation and morphology of a sodium alginate soft dendritic colloid. (a) Schematic of the SA hSDC formation process by precipitation in a turbulent medium. (b) Optical microscopy and field emission scanning electron microscopy (FE-SEM) images of sodium alginate soft dendritic colloids. These images illustrate the hierarchical fibrillar morphology of the hSDCs, which leads to high exclusion volume, strong van der Waals adhesiveness and high propensity for gelation.

### 2.3.3 Viscoelastic properties of aqueous SDC suspensions

We first established whether alginate SDCs form colloidal network hydrogels at low volume fractions in water. The hypothesis is that in aqueous suspensions, SDCs will strongly adhere to each other through van der Waals forces to form a percolating network of branched fiber sub-contacts (Figure 2.6a).<sup>65</sup> Characterization of the storage ( $G'$ ) and viscous ( $G''$ ) moduli of SDC suspensions within the linear viscoelastic region using a stress-controlled rheometer showed that the SDCs have a strong propensity for forming colloidal networks. A yield stress was observed in aqueous suspensions of 0.25 wt.% SDCs, i.e., at a lower concentration than most types of conventional colloidal gels (Figure A3).<sup>45,139</sup> The slopes of  $G'$  and  $G''$  obtained from small amplitude oscillatory frequency sweeps showed that SDC suspensions with solid content above 0.4 wt.% are gel-like in nature (Figure 2.6b).<sup>140–142</sup>

The efficient networking of SDCs is likely a result of the abundant adhesive physical contacts between the flexible, branched dendricolloids<sup>65</sup>, a phenomenon known as contact splitting that is one of the components enabling the universal adhesiveness gecko lizards.<sup>2</sup> SDC suspensions exhibit more pronounced solid-like characteristics than suspensions of common alginate particles. A 1.0 wt.% SDC suspension has a value of  $G' \approx 200$  Pa as compared to reported values of  $G' = 10 - 100$  Pa for 1.0 wt.% alginate microgel suspensions.<sup>8,143,144</sup>

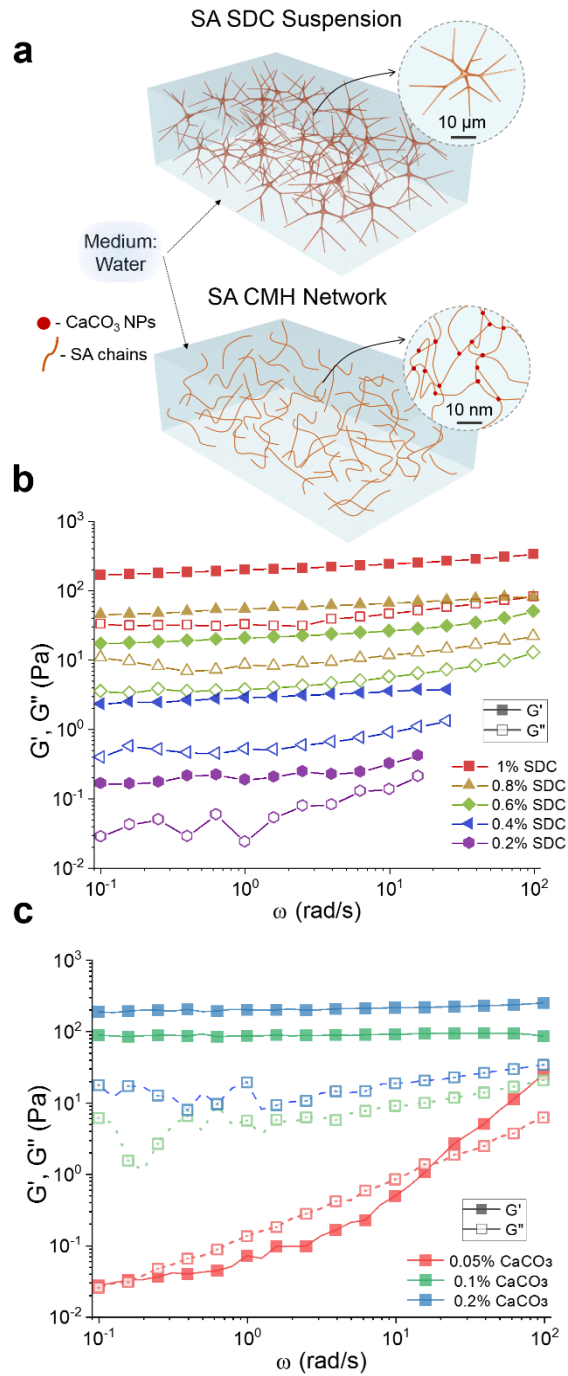


**Figure 1.6.** Linear viscoelasticity and yield stress of SA SDC suspensions and molecular gels. (a) Scheme comparing the gelation mode of a viscoelastic suspension of SDCs and of a crosslinked SA molecular hydrogel (CMH). Note the different length scales of the networks. (b) Frequency sweeps indicating the storage modulus ( $G'$ , filled) and loss modulus ( $G''$ , unfilled) of SA SDCs in aqueous suspensions. (c) Frequency sweeps indicating the storage modulus ( $G'$ , filled) and loss modulus ( $G''$ , unfilled) of 1.0 wt.% SA CMHs with 0.05 wt.%, 0.1 wt.% and 0.2 wt.% CaCO<sub>3</sub> nanoparticles and 28.14 mM after equilibration for 2 hours.

#### 2.3.4 Viscoelastic properties of alginate crosslinked molecular hydrogels (CMHs)

The continuous phase of the HHGs consists of a molecular alginate crosslinked with  $\text{Ca}^{2+}$  ions. We first characterized the properties of molecular hydrogels made of 1.0 wt.% crosslinked alginate in the absence of SDCs. The CMHs were prepared by the addition of  $\text{CaCO}_3$  nanoparticles and D-Gluconic acid  $\delta$ -lactone (GDL) to a SA solution. As GDL undergoes hydrolysis and lowers the pH, the  $\text{CaCO}_3$  slowly releases  $\text{Ca}^{2+}$  ions.<sup>137,138</sup> The linear viscoelastic properties of the CMHs following 2 hours of equilibration are plotted in Figure 2.6c. Solid-like behavior is observed above 0.05 wt.%  $\text{CaCO}_3$  (20/1 SA/ $\text{CaCO}_3$ ). Further loading of the alginate hydrogel with  $\text{Ca}^{2+}$  increases its stiffness, however, we found that hydrogels containing  $\geq 0.2$  wt.%  $\text{CaCO}_3$  (5/1 SA/ $\text{CaCO}_3$ ) exhibited significant syneresis – pronounced shrinkage of the crosslinked gel accompanied by release of water (Figure A4). To avoid such syneresis, we maintained the ratio of 10/1 SA/ $\text{CaCO}_3$  (1.0 wt.% SA, 0.1 wt.%  $\text{CaCO}_3$  for pure CMH) in the HHG formulations. Interestingly, at this ratio the pure 1.0 wt.% CMH and 1.0 wt.% SDC gels had storage moduli of similar magnitude, even though these two systems are gelled by different physical mechanisms and are very dissimilar in their appearance (clear CMH gels vs. turbid SDCs suspensions) attributed to the  $\text{Ca}^{2+}$  being highly localized in the SDC fibers as opposed to homogeneously distributed in the CMH matrix.

#### 2.3.5 Viscoelastic properties of composite HHGs

We next investigated how the colloidal network of SA SDCs can be combined with the molecular SA CMH matrix and crosslinked to produce self-reinforced HHGs. We synthesized a variety of HHGs where the total SA concentration was kept constant at 1 wt.% while the ratio of SDCs to CMH was varied (Table A1). The  $G'$  and  $G''$  values of the HHGs were measured as a function of time using small amplitude oscillatory stress and frequency sweeps after an equilibration time of  $t = 2$  h. All HHG samples exhibited solid-like behavior (Figure 2.7a). Notably, the  $G'$  values of all

HHG samples were larger than those of either pure CMHs or pure SDC suspensions, with maximum values recorded at low SDC concentrations (0.175 – 0.25 wt.% SDCs). Representative stress-strain curves (Figure 2.7b) obtained by mechanical tensile testing also demonstrate that the HHG systems have larger stiffness than the gels from SDCs or CMHs alone. Interestingly, we were not able to measure reliably the tensile behavior of pure SDCs suspension using a common testing machine. The SDC particulate gel is brittle and lacks the intrinsic elasticity of the crosslinked molecular alginate gel, illustrating the difference in their physical networking mechanisms.

The data from both rheometry and tensile stress-strain measurements for all HHGs are consolidated in Figure 2.7c. These data demonstrate that the homocomposite systems comprising mixed SDCs and CMHs exhibit a strong synergistic effect. Both the values of the complex modulus  $G^*$ , and the Young's modulus,  $E$ , for the homocomposite gels showed greater than  $3\times$  increases with maxima at low SDCs to CMH ratios. This effect cannot be solely attributed to the slightly increased concentration of the  $\text{Ca}^{2+}$  crosslinker in the homocomposite system with  $\text{Ca}^{2+}$  localized both within the SDC reinforcement as well as homogeneously distributed through the CMH continuous phase. The highest shear modulus measured in HHGs ( $G^* = 950$  Pa at a composition of 0.125 wt.% SDCs/0.875 wt.% CMH) does not correspond to the highest  $\text{Ca}^{2+}$  concentration, as further increasing the SDC content reduces the resulting HHG stiffness. The  $\text{Ca}^{2+}$  concentration in this formulation was estimated to be  $\sim 1.5\times$  the concentration found in the pure CMH (Figure A5, Table A2). A frequency sweep performed on a CMH with  $2\times$   $\text{CaCO}_3$  shows that the  $G^* \approx 250$  Pa (Figure 2.6c), which is much less than that of the stiffest HHG formulation (0.125 wt.% SDCs/0.875 wt.% CMH). Multiple measurements consistently showed a small increase in the  $G^*$  peak at a composition of 0.875% SDCs, which could be a result of secondary entanglement

of the concentrated SDCs stabilized by small amounts of molecular alginate, although its exact mechanism has yet to be elucidated.

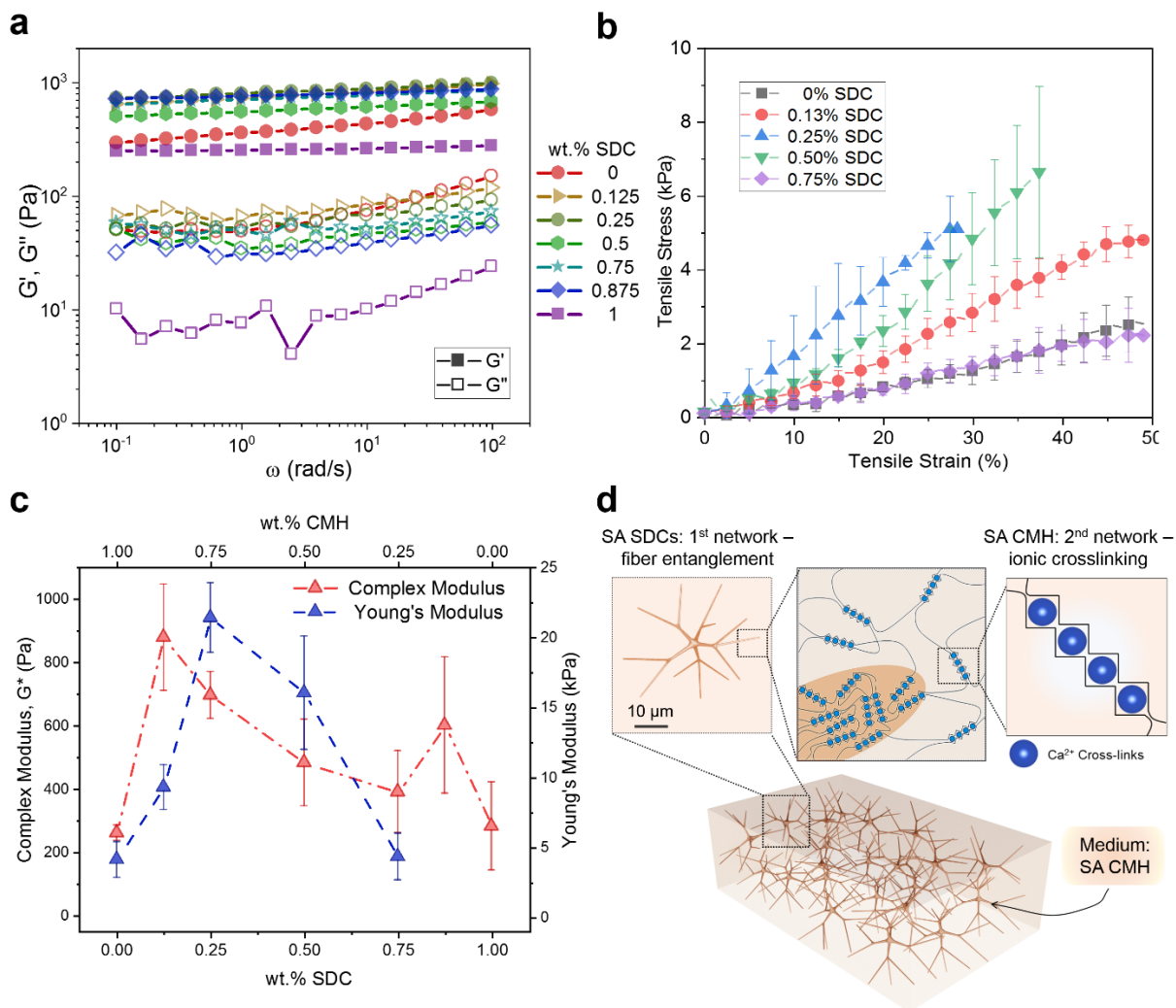


**Figure 2.7.** Mechanical properties of SA homocomposite gels. (a) Frequency sweeps of 1.0 wt.% HHGs of varying SDC concentrations ( $n=2$ ). (b) Representative stress-strain curves for various HHGs ( $n=5$ ). (c) Rheological complex modulus obtained from a frequency sweeps at a frequency of 1 rad/s (red,  $n=3$ ) and tensile (blue,  $n=5$ ) properties of various SDC/CMH HHGs. Total alginate concentration is maintained at 1.0 wt.% for all data. (d) Schematic of the hierarchical interactions between the colloidal and molecular alginate networks in HHGs. These results demonstrate the structural synergism of the double SDC and CMH networks within HHGs resulting in controllable and self-reinforced high composite stiffness.

In summary, the strong synergistic effect leading to increased mechanical strength of the HHGs could be directly attributed to the physical entanglement of the molecular SA and colloidal SDC networks, where the divalent  $\text{Ca}^{2+}$  ions bridge the alginate chains in the egg-box configuration at the interface between the microgel fibers and the continuous matrix.<sup>8</sup> The resulting HHG structure is illustrated in Figure 2.7d. This divalent-ion crosslinking structure is stable in most media but can be disassembled by immersion in solutions of strong chelating agents such as EDTA. We found that both pure SA and SDC systems dissolve easily in EDTA, while the HHG is more resilient, possibly due to suppressed chelator transport (Figure A6).

### 2.3.6 Time-dependent stiffening of homocomposite hydrogels

One of the other functionalities imparted by the colloidal-molecular networks in the HHGs is in the tunability of their gelation kinetics. We measured the time dependence of gelation through oscillatory shear rheology performed on SDCs, CMHs, and composite HHGs at the same SA concentration of 1 wt.%. The time sweeps performed with a pure 1 wt.% SDC suspension plotted in Figure 2.8a show that the SDC suspension immediately exhibits solid-like behavior without the addition of  $\text{CaCO}_3$  or GDL. This is expected, as the formation of this network occurs by contact splitting and entanglement of the fibrillar dendricolloids. The values of  $G'$  and  $G''$  of this system do not show any further stiffening by crosslinking or densification. The pure CMH, on the other hand, initially shows liquid-like behavior and gradually solidifies as  $\text{Ca}^{2+}$  crosslinker is released by hydrolysis. It develops into a fully crosslinked system in  $\approx 120$  mins (Figure 2.8b).

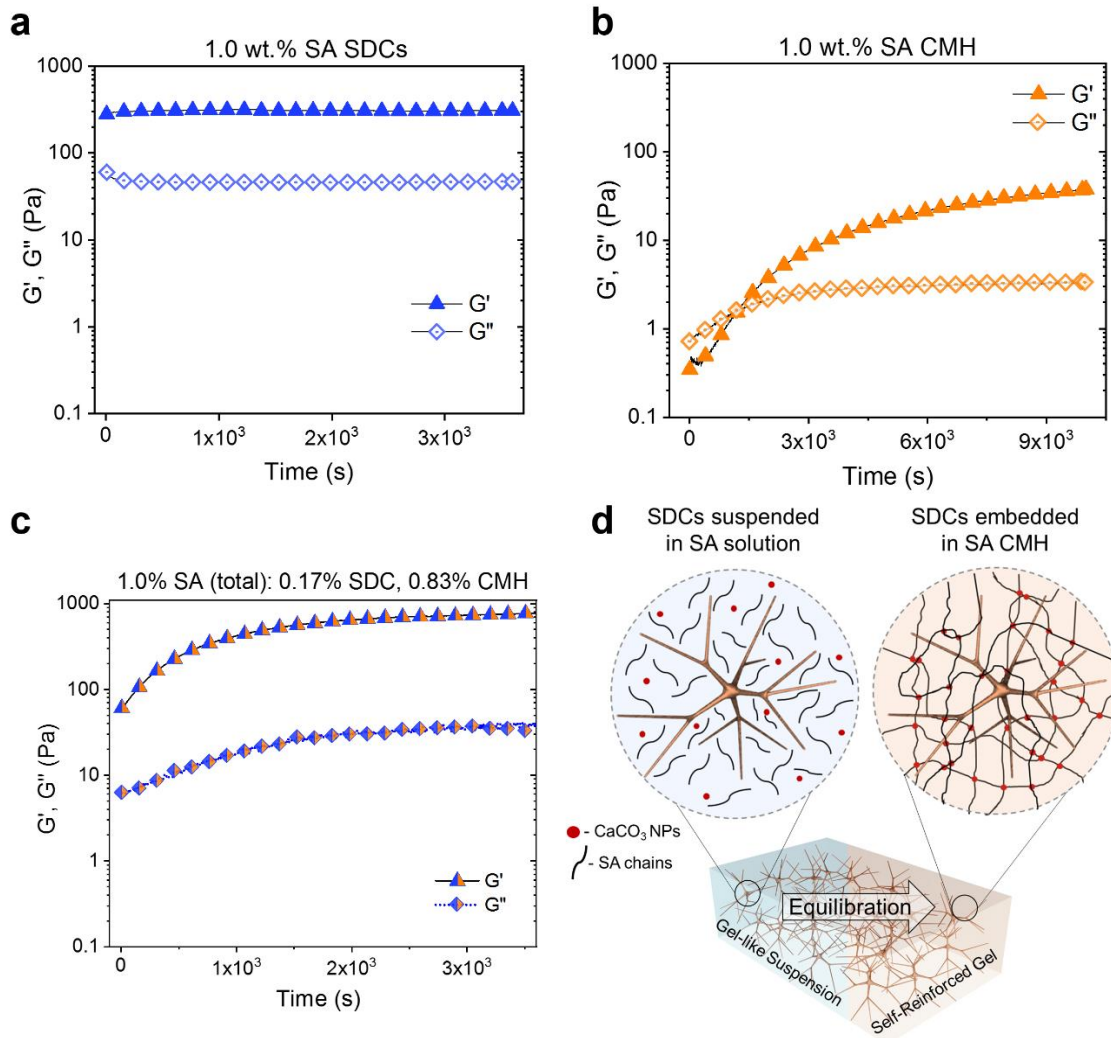


**Figure 2.8.** Time-dependent gelation of SA SDC suspensions, SA CMHs, and SA HHGs. Time sweeps indicating  $G'$  and  $G''$  (1 rad/s, 1% strain) of (a) 1.0 wt.% SA SDC suspension in water, (b) 1.0 wt.% SA CMH following GDL addition and (c) 1.0 wt.% total SA (0.17 wt.% SDC, 0.83 wt.% CMH) HHG following GDL addition. (d) Schematic showing the time-dependent transition of a HHG from a colloidal gel to a self-reinforced homocomposite via CMH crosslinking. HHG formulations show immediate, elastic-solid behavior from the colloidal network and further stiffen with the ionic crosslinking of the molecular network.

The temporal evolution of the HHG is directly linked to the kinetics at which its constituent SDCs and CMH assemble into networks. The HHG initially solidifies due to the gelation of the mechanically rigid SDC network. It then forms a sturdier hydrogel over time as the interpenetrating

CMH molecular network becomes crosslinked by  $\text{Ca}^{2+}$  ions released *in situ* (Figure 2.8c & d). The final value of  $G'$  of the HHG system is  $\sim 3\times$  larger than that of the pure SDCs, in agreement with the mechanical data reported in Figure 2.7. These material properties reveal controlled initial yield stresses and slow buildup of hydrogel elasticity over time. This makes them particularly suitable as 3D printable materials for making of intricate and sturdy hydrogel architectures.

### 2.3.7 3D printing with HHGs

The homocomposite approach allows precise control over the properties of the mixture in a way that enables 3D printing via extrusion, which has traditionally been challenging with hydrogel precursors. Notably, neither of the two components of the composite gel are viable as printing inks on their own. Pure SDC suspensions are mechanically stable upon extrusion and maintain their shape upon removal of an applied stress. However, suspensions made of SDC particles alone cannot be crosslinked by GDL- $\text{CaCO}_3$  addition to produce a stiff elastic material by bridging active -COOH- sites on neighboring SDCs (Figure A7). Conversely, non-crosslinked CMH solutions are unsuitable for extrusion additive printing because they slowly form solid gels by GDL- $\text{CaCO}_3$  crosslinking (Figure 2.8b), a solidification process that requires time on the order of hours to days. By making a homocomposite ink using these two distinct forms of alginate, we present a type of bespoke, extrudable hydrogel material in which the time-independent yield stress and solidification time can be tuned on demand. As the 3D printer applies a pressure drop that is greater than the yield stress of the HHGs, the extruded shape is preserved by the rapid gelation of the SDC network (Figure 2.8c).

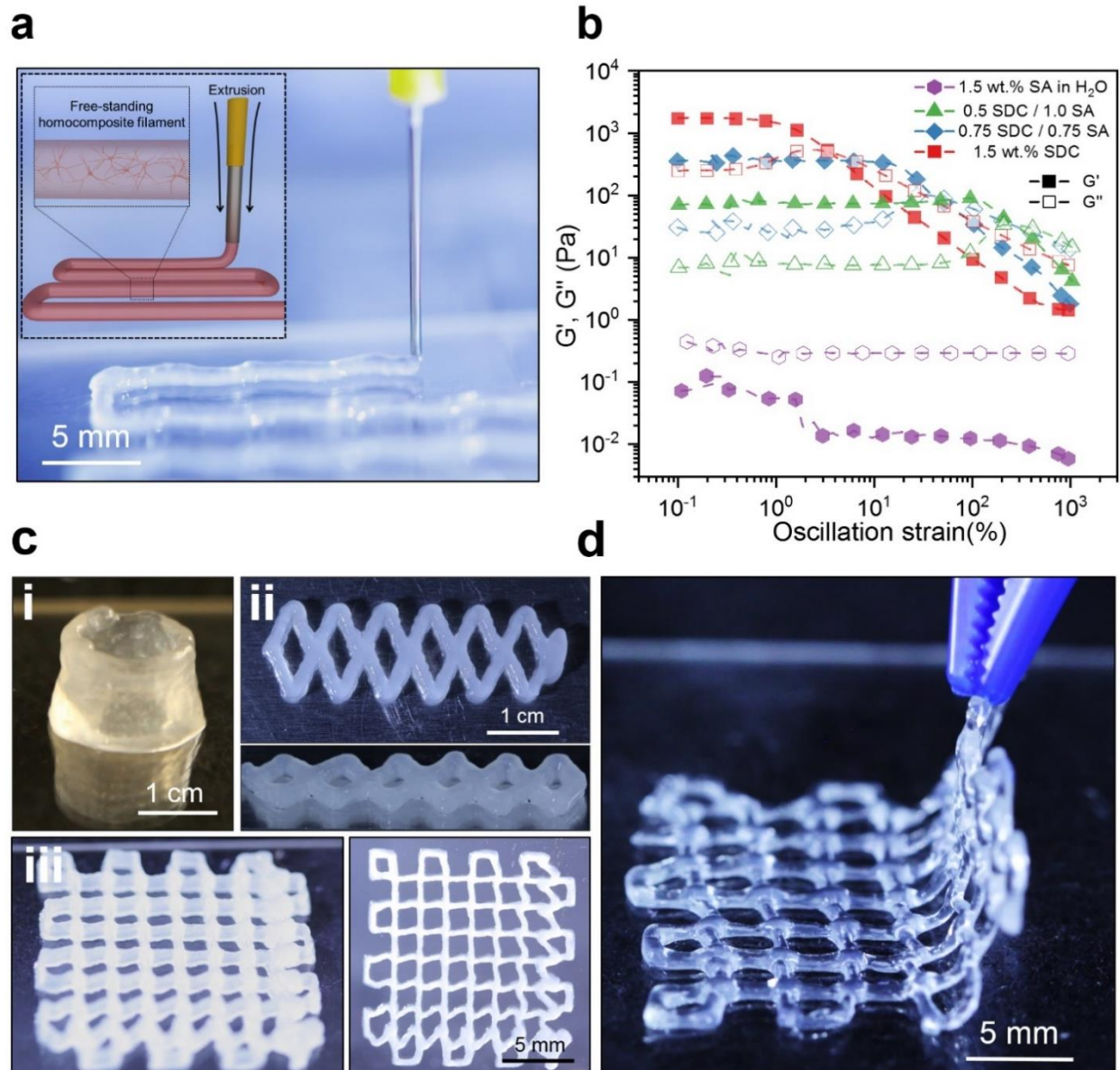


**Figure 2.9.** 3D Printing with homocomposite hydrogels. (a) Schematic illustration and image of 3D printing of SA SDC filled sodium alginate ink. (b) Complex modulus vs. stress curves for 1.5 total wt.% SA and SDC/SA HHG mixtures containing CaCO<sub>3</sub> nanoparticles, prior to GDL addition measured at 6.23 rad/s. (c) Images of extruded HHG paste that has been layered in 3D (0.75 wt.% SDC, 0.75 wt.% CMH): (i) 10 layers from a 18G nozzle, (ii) 3 layers from a 16G nozzle, (iii) 5 layers from a 25G nozzle. (d) removal of the equilibrated hydrogel design from the substrate. HHG formulations have the ability to flow upon extrusion, maintain their shape due to the colloidal yield stress, and result in a strongly self-reinforced structure following completion of the secondary ionic crosslinking reaction.

To demonstrate the extrudability and shapeability of such hydrogels combining colloidal and molecular networks, HHG formulations with total alginate concentration of 1.5 wt.% were loaded into a 3D printer operating by pressure-driven extrusion (Figure 2.9a). The homocomposite systems were amenable to 3D printing in ambient conditions without necessitating a crosslinker bath or yield stress medium to maintain its shape. Notably, the  $G'$  of 1500 Pa of pure SDC suspension is nearly four orders of magnitude larger than that of the CMH mixture at the same concentration prior to GDL addition (0.5 Pa, Figure 2.9b).

The mixing of SDCs and CMHs results in the emergence of yield stress at all ratios tested. At small strains, the network remains a solid-like material due to the van der Waals interactions. As the strain increases beyond the yield point, the physical entanglements between the SDC fibrils are overcome and the yielded material can be extruded. Despite maximal HHG gel stiffness emerging at lower relative SDC/CMH ratios (Figure 2.8c), HHG formulations with greater relative SDC contents produced more pristine filaments with improved filament layering. The maximum  $G^*$  obtained at a 1/1 SDC/CMH ratio is consistent with the results of equilibrated 1.0 wt.% HHGs, which show a similar maximum  $G^*$  at that ratio (Figure A8). The increased yield stress of 1.5 wt.% SA HHGs enabled smooth and consistent HHGs extrusion for 3D printing.

The process of 3D printing of a homocomposite hydrogel by direct extrusion in air is demonstrated in Figure 2.9a and 2.9c. The HHG formulation is extruded through a nozzle (25G, 0.26 mm ID) at 140 kPa and the gel retains neatly its shape due to its yield stress ( $\approx 80$  Pa). Additive shaping of the structures in the z-direction can be achieved by overlaying consecutive layers, which were found to adhere well to the underlying ones. We were able to achieve the additive printing of  $>10$  layers of hydrogel in the vertical direction without reducing the rate of extrusion. A few examples of such vertically developed structures extruded in consecutive layers are demonstrated

in Figure 2.9c. Much higher height/width ratios can be achieved by staged extrusion, which allows additional time for gel solidification, as well as increasing the paste yield stress via the HHG composition. Following molecular crosslinking and stiffening for 60 min, the printed hydrogel shapes could be readily removed from the substrate (Figure 2.9d). Further adjustment of the relative concentrations of SA, SDCs, CaCO<sub>3</sub>, and GDL allows the formulation of printable homocomposite hydrogels with tunable properties.

## 2.4 Conclusions

Controlling the rate of precipitation during turbulent shear-based polymer precipitation allows the production of a range of particle morphologies. Though morphologically similar, the alginate and chitosan hSDCs, SDC, and cSDCs have fundamentally different cross-link chemistries comprising their fibers. The expansion of the shear-based polymer precipitation as a technique to include these different precipitation mechanisms increases the library of colloidal materials that can be produced from both biologically-derived and synthetic polymers and hydrogels to inform the design of soft materials.

We introduce a class of homocomposite hydrogels that are self-reinforced by a network of alginate SDCs interspersed within an alginate CMH network. The dispersed and adhesive nanofibrillar coronas of the SDCs lead to the formation of strong gels in SDC suspensions at very low volume fractions. They enable the formation of sturdy HHGs when interspersed in a continuous, molecular gel of the same biopolymer. The stiffness of the resulting HHG appears to be governed by the synergistic interactions of the molecular alginate network and the colloidal-scale fibrillar SDC network. These HHGs are made using SA as a common polymer, but the principle can be applied to other hydrogels of natural or synthetic origin. While methods for 3D printing with alginate have been reported previously<sup>129,145</sup>, the method presented here has a number of potential advantages, such as it does not need any bath of crosslinking medium, as well as printing with pure alginate without any additives. The HHGs in this study demonstrate two distinctive emerging concepts that can guide materials design of hydrogel classes. Firstly, the HHGs are stabilized by interpenetrating double networks at two very different length scales: molecular (nanometer scale) and colloidal (up to microscale). Second, due to the chemical uniformity of both networks, these hydrogels are both double network and homocomposite, which

enables to adjust their unusual and potentially practically useful properties. The fabrication of such designer materials is enabled by the ability of the SDCs to control media viscoelasticity and composite stiffness. The SDCs bring about rapid physical solidification due to van der Waals interaction based adhesion (or shorter: due to van der Waals interaction) between their nanofibrillar coronas. This allows extrudability and injectability which are key prerequisites for numerous applications of hydrogels. The HHGs thus present a solution to the problem which makes molecular alginates and other common gel precursors poorly suitable for shaping by extrusion processes (such as in 3D printing and injection) because of a lack of initial yield stress which renders them fluid for some time after extrusion.

While the alginate-alginate system demonstrates the advantages of homocomposite formulations, the potential of SDCs as viscoelastic modification and yield stress additives can be extended to many other systems. The SDCs are highly efficient as homocomposite fillers and their dispersion within other continuous polymer phases allows precise modulation of their viscoelasticity and composite stiffness at extremely low filler concentrations. The physical gelling of SDC as means of imparting immediate yield stress to a mixture that can be immediately 3D printed and subsequently builds up strength can also be applied in heterocomposite formulations. To illustrate how SDC reinforcing networks can be used in heterocomposite gel formulations, we constructed several examples which are described in Appendix A. The first example is a gel with liquid silicone matrix and polyvinyl alcohol SDCs that exhibits a yield stress at extremely dilute SDC concentrations and forms polydimethylsiloxane elastomer inks suitable for 3D printing by extrusion (Figure A9a). In addition, we combined the “homocomposite” approach presented herein with the well-studied alginate-polyacrylamide double network.<sup>93</sup> The resulting PAAm – SA CMH

– SA SDC triple network gel showed increased tensile strength with the inclusion of the colloidal SDC network without increasing the total alginate concentration (Figure A9b).

The SA HHG examples unveiled here have numerous potential applications such as in biomedical 3D printing<sup>120,146–148</sup>, soft robotics<sup>95</sup>, food products with 3D printed edible structures<sup>149</sup>, and haptic materials with unique mechanical responses.<sup>150</sup> They could also enhance the design of green and sustainable materials made from biodegradable polymers. The most impactful feature of their structure is that the homocomposite colloidal-molecular double network enables independent tuning of chemical composition and material properties. This approach can be transcribed to other classes of soft matter, whose functionality will be derived from their multi-scale network morphology, rather than their molecular composition. Overall, the SDCs emerge as a new class of soft colloids capable of tailoring the properties of many forthcoming liquid and solid composite materials.

### **CHAPTER 3: Porous Sheets and Membranes from Soft Dendritic Colloids**

Partially based on

S. Luiso, A.H. Williams, M.J. Petrecca, S. Roh, O.D. Velev, P.S. Fedkiw.

*J. Electrochem. Soc.* **2021**, 168, 020517.

### 3.1 Introduction

Highly porous membranes have found a multitude of applications as filtration materials, medical wipes, bioscaffolds, and lithium-ion battery (LIB) separators. Nanofiber production techniques like electrospinning, meltblowing, and wet-laying are commonly utilized to achieve mechanically robust polymeric membranes with high porosity. For most applications, both the chemical properties of the polymer comprising the nonwoven material and the physical characteristics like porosity and elasticity of the bulk membrane are paramount towards its functionality. Two specific applications of fibrous polymer sheets that are highly reliant on the properties of the polymer material are bioscaffolds and LIB separators.

Advanced *in vitro* systems for biological studies aim to close the gap between the shortcomings of common *in vitro* platforms and complex *in vivo* models by incorporating tissue level complexities in a controlled cell culture environment.<sup>151-159</sup> These systems integrate aspects of tissue relevant microstructure, morphology, and mechanics. Physiological scaffolds for cell growth mimic the extracellular matrix (ECM) characteristics of human tissue: they are soft, three-dimensional, and composed of highly fibrous components. Together, these parameters comprise a porous biocomposite material ideal for cell growth.<sup>160-162</sup> The biomechanical properties of the ECM play a role in regulating cell behavior.<sup>163,164</sup> The dimensionality of the cell scaffold as well as the degree of pore isotropy is known to affect human cell proliferation, differentiation, and toxicity. Porous 3D scaffolds yield a more physiologically relevant topography and anisotropy.<sup>165-168</sup> The stiffness of the scaffolds has been shown to influence cell mechanotransduction pathways including human mesenchymal and endothelial cell models on 2D substrates.<sup>169-176</sup> For this reason, the development of biomimetic scaffolds with tunable mechanics from the same base material could serve as a superior platform for evaluating cellular responses, such as NM toxicity.

LIBs are an essential energy storage system for a variety of applications because of their high energy-storage capabilities and long cycle life.<sup>177,178</sup> The structure and properties of the separator, which is placed between the anode and the cathode of the battery, play a critical role in cell performance. The separator must be chemically and electrochemically stable and is usually not ionically conductive by itself; the liquid electrolyte within it facilitates ion transport. A desirable battery separator is characterized by mechanical and thermal stability, and high electrolyte wettability.<sup>179</sup> Polyolefin monolayer microporous separators are the most widely used commercially and require surfactants to obtain a high electrolyte wettability.<sup>180</sup> Relative to conventional microporous polyolefin separators, fibrous polymeric membranes, such as electrospun nonwovens, have the advantage of low mass and high porosity. In addition, the fibrous mat provides structural cohesion due to its intertwined fibers.<sup>22</sup> Most polymers used to make fibrous battery separators have demonstrated lower ionic conductivity than conventional microporous separators, but polyvinylidene fluoride (PVDF) has shown high chemical stability and affinity for electrolytes commonly employed in Li-ion cells like Galwick®.<sup>21,181</sup>

Herein, we investigate a new class of porous membranes made from soft dendritic colloids (SDCs). The SDCs are made via a process which enables control over their constitutive fiber size by controlling the concentration of polymer in the injection solution or nonsolvent viscosity.<sup>65</sup> Such SDCs can be formed into cell culture membranes emulating the mechanical and morphological characteristics of human lung tissue as well as LIB separator materials. The PU SDC cell scaffolds utilized in this study were used to develop a novel biomimetic *in vitro* lung inhalation model for nanomaterial toxicological testing (Figure 3.1). Additionally, we show that porous sheets from PVDF SDCs serve as versatile and stable membranes for LIB separator applications.

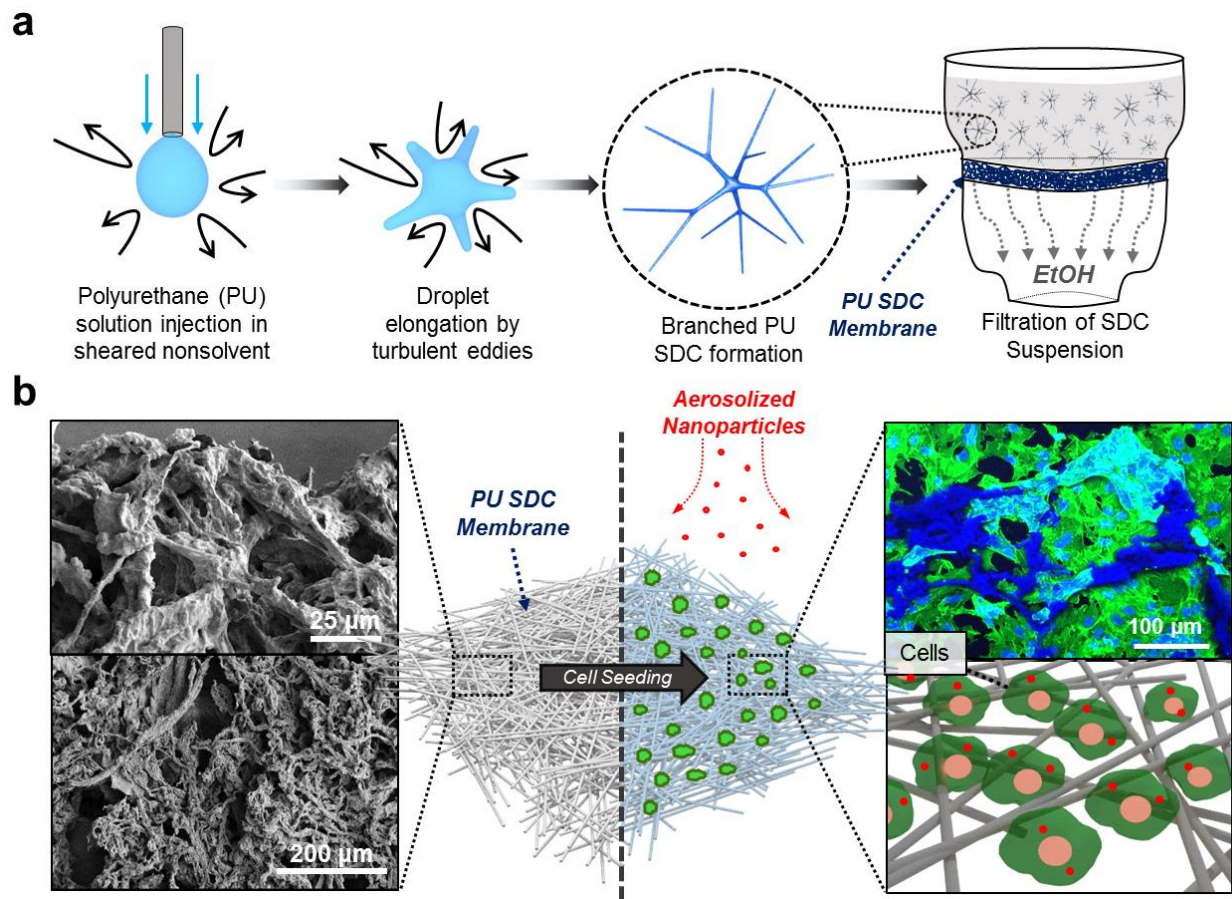


**Figure 3.1.** Schematic of soft dendritic colloid nonwoven preparation and administration of aerosolized nanomaterials on seeded nonwovens. (a) The process of PU SDC fabrication and nonwoven preparation includes multiple steps resulting in a mechanically robust mat for cell culture. (b) left, scanning electron microscopy (SEM) images illustrating membrane morphology; middle – schematic representation of aerosol exposure of cells cultured on Soft or Stiff PU SDC membranes; right top – displays a confocal image of lung epithelial cells (green) on Soft PU SDC scaffolds; right bottom – displays a schematic of cellular integration within and on-top of the PU SDC resulting in a confluent, epithelial barrier capable of maintaining air-liquid interface culture conditions.

## 3.2 Materials and Methods

### 3.2.1 Fabrication of SDCs

To make PU SDCs, a 3% (w/w) solution of polyurethane (PU, Huntsman Irogran® PS455-203) was prepared in chloroform (Sigma-Aldrich) at 90°C while stirred. Following dissolution, the PU solution was brought to room temperature and injected into the shear zone of a modified colloidal mill (IKA Magic Lab) at 20,000 RPM circulating turbulently-sheared nonsolvent medium composed of ethanol (EtOH, Koptec) and glycerol (Gly, Alfa Aesar) to produce SDCs. To prepare PVDF SDCs, polyvinylidene fluoride (PVDF, Sigma Aldrich, Mw = 530,000 Da), dimethyl sulfoxide (DMSO, Fisher Scientific) and EtOH were utilized. PVDF pellets were dissolved in DMSO by heating at 110°C for 24 hours while stirred. Following dissolution, the PVDF solution was cooled to room temperature and injected at a rate of 1 mL·s<sup>-1</sup> directly through a capillary into the shear zone of a colloidal mill set to 20,000 RPM and filled with 500 mL of EtOH. The resulting SDCs in suspension were then centrifuged for 2 minutes at 3.0 rcf and washed by redispersion in pure ethanol (8× dilution of SDC pellet volume). This process was repeated 5× to remove remaining solvent and nonsolvent from the suspensions.

### 3.2.2 Preparation of porous SDC membranes

SDC membranes were prepared by filtering a 1.0 % (w/w) SDC suspension in EtOH using a vacuum filtration apparatus (Millipore, HVLP 0.45 µm filter, 35 mm head). Following filtration and drying, the membranes were peeled from the filter and dried for 24 hours at 60°C.

### 3.2.3 Mechanical and optical characterization of SDC membranes

Dendricolloids and SDC membranes were visualized using both optical microscopy (Olympus BX-61) and field emission scanning electron microscopy (FEI Verios 460L SEM). Membrane thickness was determined using a handheld micrometer (Marathon). Mechanical characterization

of the membranes was performed using a universal testing machine (Instron 5943). with 15 mm × 10 mm samples of varying thickness and a crosshead speed of 15 mm•min<sup>-1</sup> and 2 mm•min<sup>-1</sup> for PU and PVDF SDC membranes, respectively.

### 3.2.5 Capillary flow porosimetry and porosity

Pore size analysis was performed with a capillary flow porosimeter (Porous Materials Inc.). Samples were first wetted with Galwick<sup>®</sup> ( $\gamma_{LG} = 15.9 \text{ dynes}\cdot\text{cm}^{-1}$ ) and pore diameters were calculated using the Young–Laplace equation (Equation 3.1), with  $D$  as the pore diameter,  $p$  as the extrusion pressure, and  $\theta$  as the contact angle of Galwick ( $\sim 0^\circ$  assumed).

$$D = 4\gamma_{LG} \cos \theta / p \quad (3.1)$$

This technique provides the population of pores with a specific diameter at each applied pressure. By applying the equations used to calculate the number average molecular weight ( $M_n$ ), weight average molecular weight ( $M_w$ ), and polydispersity index ( $\text{PDI} = M_w/M_n$ ) to the porosimetry results, the number average pore size ( $P_n$ ), weight average pore size ( $P_w$ ), and heterogeneity index ( $\text{HG} = M_w/M_n$ ) were determined. Porosity was then back calculated using weight, density, and thickness.

### 3.3 Results

#### 3.3.1 Morphology of polyurethane SDCs

Porous, ultrasoft polymeric membranes were prepared by first fabricating soft dendritic colloids (SDCs) from a biocompatible polyurethane (PU) using a pure ethanol (EtOH) nonsolvent as previously described (Figure 3.2a).<sup>65</sup> The resulting Stiff PU SDCs showed the characteristic branched-fibrous structure as the previously reported SDCs but had a more globular morphology with larger and more clustered fibers (Figure 3.1a). The addition of 20% vol. glycerol (Gly) to the ethanol nonsolvent during the formation process clearly resulted in Soft PU SDCs with more expressed fibers of smaller diameter (Figure 3.2b).

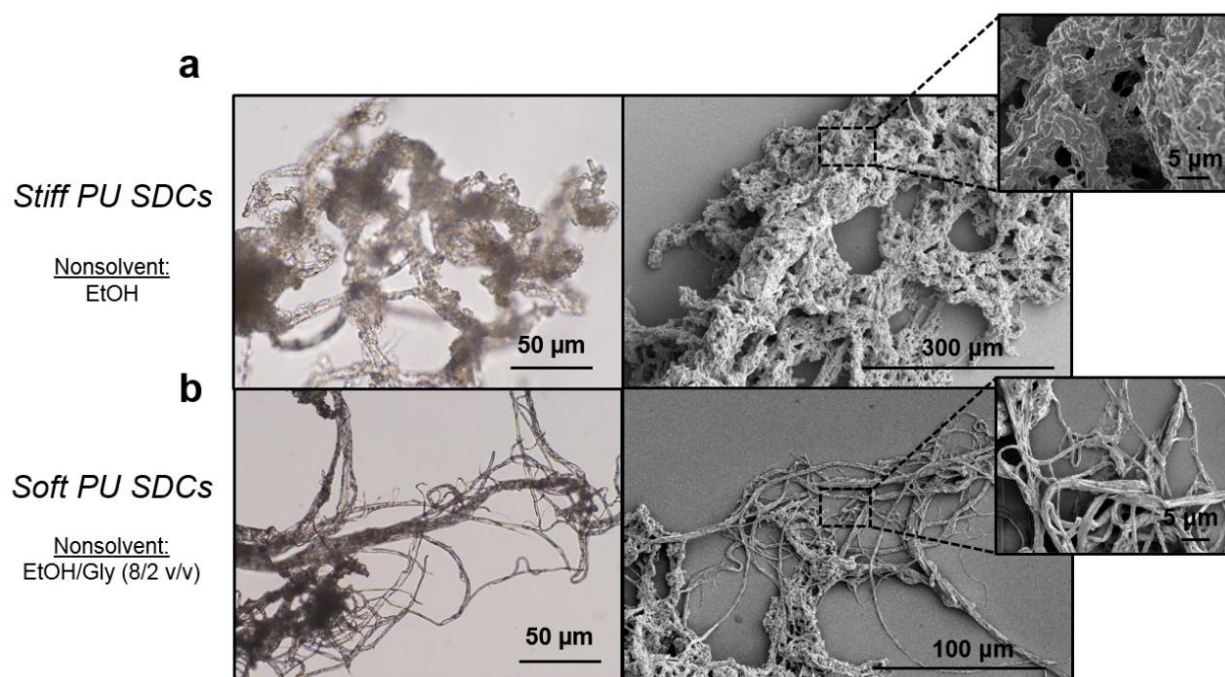


**Figure 3.2.** Glycerol addition to the nonsolvent provides polymer processing control over the morphology of the Soft and Stiff PU SDC mats. Optical and scanning electron micrographs of PU SDCs prepared with (a) 100% EtOH and (b) 80/20 EtOH/Glycerol (v/v) nonsolvent media. The addition of just 20 vol.% glycerol to the nonsolvent medium reduces the fiber size in the produced SDC.

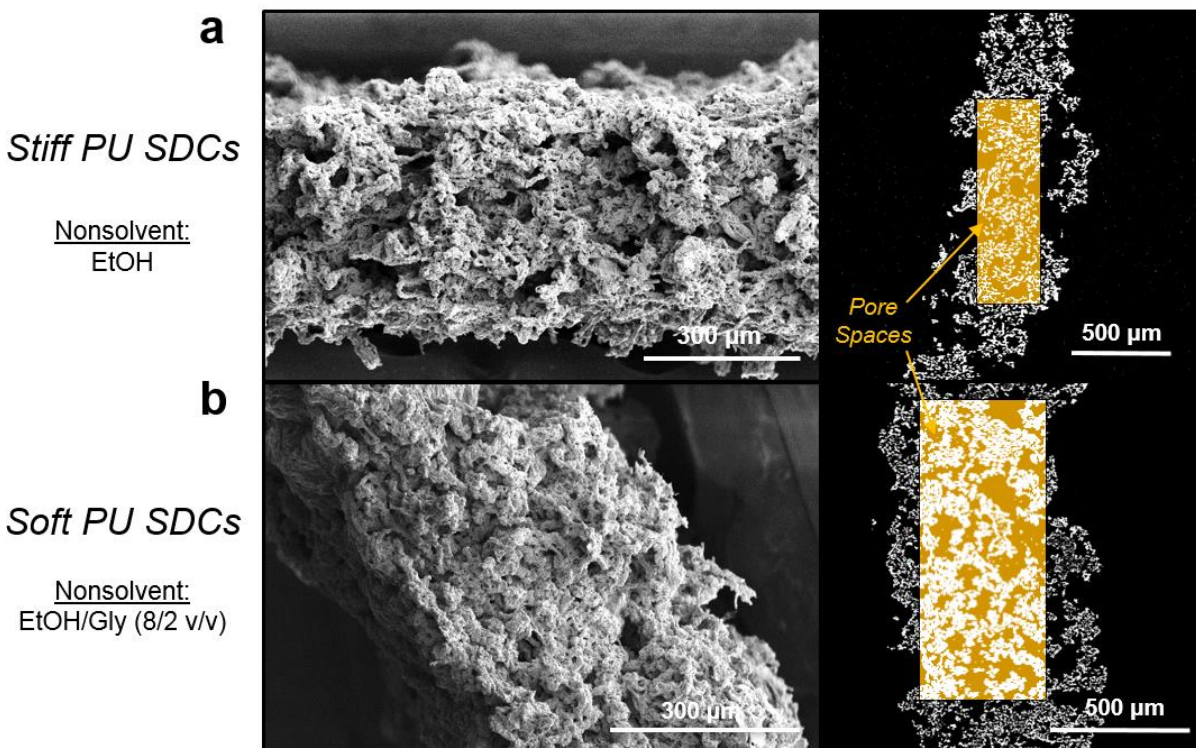


**Figure 3.3.** Morphological characterization of Stiff and Soft PU SDC membranes. Analysis of PU SDC membranes by scanning electron microscopy (left) and X-ray nanotomography (right) of samples prepared using nonsolvents composed of (a) 100% EtOH (Stiff PU SDCs) and (b) 80/20 (v/v) EtOH/Gly (Soft PU SDCs). Highlighted portions within the membranes indicate how porosity data was calculated from 3D reconstructions.

### 3.3.2 PU SDC nonwovens optical and internal structure characterization

The SDCs are produced in suspension, hence the resulting particles are easily assembled into mechanically robust nonwoven sheets of high porosity and surface area by layering. Following the particle washing step, PU SDC in EtOH suspensions are simply vacuum-filtered and dried to yield highly soft and elastic PU SDC membranes. Cross-sectional scanning electron micrographs of both PU SDC nonwovens (Figure 3.3) as well as the internal 3D structure enabled us to measure the fraction of pore space of the PU SDC nonwovens using X-ray nanotomography. Because of the highly anisotropic shape of the pores in the SDC nonwovens, we analyzed the minimum, average, and maximum pore Feret diameters using Dragonfly software (Table 3.1).

**Table 3.1.** Porosity and pore Feret diameters of Soft and Stiff PU SDC nonwovens analyzed using Zeiss Xradia micro-CT.

	<b>Porosity (%)</b>	<b>Min. Feret Diameter (<math>\mu\text{m}</math>)</b>	<b>Avg. Feret Diameter (<math>\mu\text{m}</math>)</b>	<b>Max. Feret Diameter (<math>\mu\text{m}</math>)</b>
Stiff PU SDC	70.1	207.77	1072.24	1891.87
Soft PU SDC	70.2	282.22	1322.04	1662.87

When producing these ultrasoft polymer membranes for long-term cell culture, repeated-strain effects such as membrane creep and subsequent tensile modulus relaxation are of concern. To investigate the mechanical resilience of both PU SDC membranes, a series of experiments were performed in which Soft and Stiff SDC membranes were subjected to cyclic strain, while the elastic moduli, as well as the magnitude of membrane creep, were recorded each strain cycle. A representative stress-strain curve for cyclic, 30% strain shows how these values drift in the course of undergoing cyclic strain (Figure 3.4a). The tensile moduli and membrane creep for Soft and Stiff PU SDC membranes were then evaluated using a cyclic strain ramp up to 50% strain for five cycles (Figure 3.4b-c). The Stiff PU SDC membrane displays tensile moduli (~ 750 kPa) that are 3-fold larger than the Soft PU SDC membranes (~ 250 kPa).

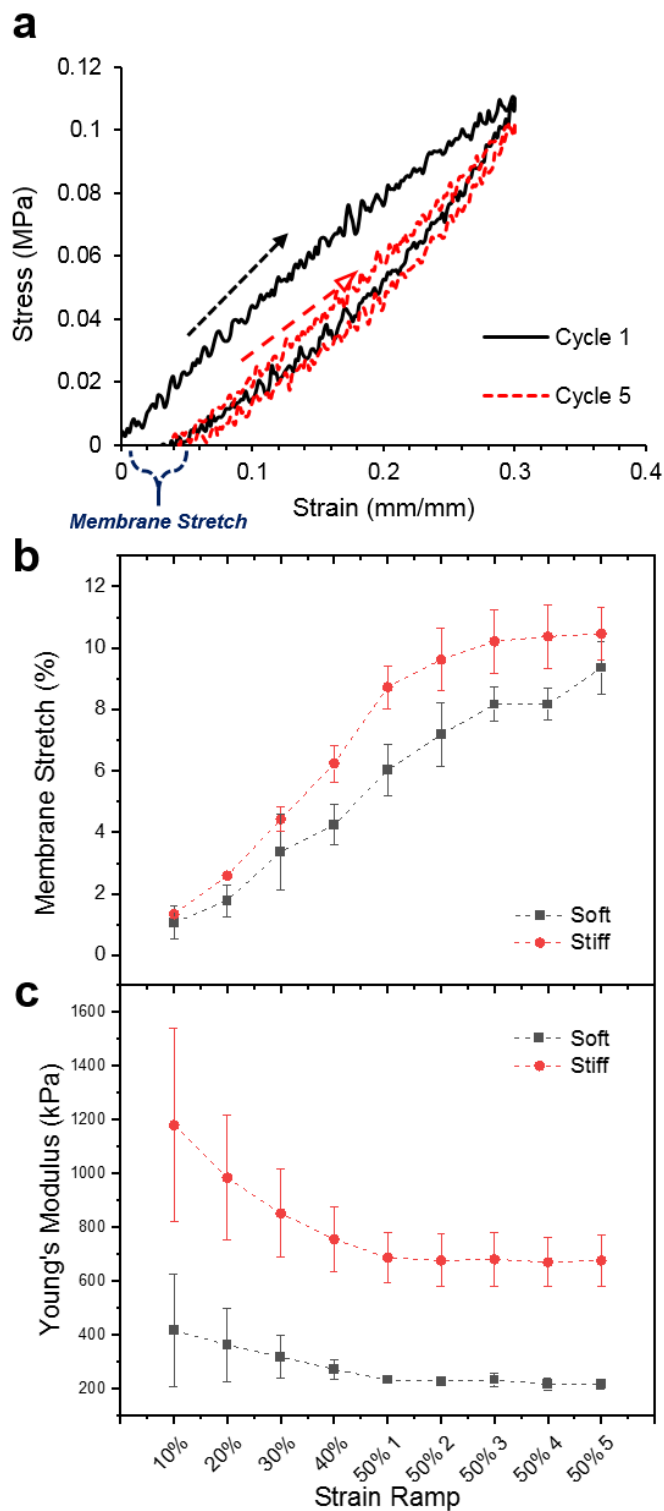


**Figure 3.4.** Mechanical properties of Stiff and Soft PU SDC membranes. (a) Representative cyclic PU SDC membrane strain indicating elastic modulus relaxation and membrane stretch after cyclic 30% strain. (b) Membrane creep and (c) Elastic modulus of Soft and Stiff PU SDC nonwovens with ramping, indicating cycling strain up to 50% (n=3). PU SDCs produced with smaller fibers result in softer nonwoven membranes.

### 3.3.3 PVDF SDC and NS membrane fabrication

In the lower concentration 5 wt.% PVDF in DMSO injection solution, the resulting particles have the characteristic highly branched, fibrous SDC structure (Figure 3.5a-c). An increase to 12.5 wt.% PVDF in DMSO injection solution results in the formation of thin, but highly porous nano-sheet (NS) particulates (Figure 3.5g-i). Particle morphology affects membrane formation during the filtration step. As the concentration of PVDF increased from 5% to 10 wt.%, the SEM images reveal that the membranes transition from an entirely fibrous network to a mixed-morphology to a nano-sheet morphology, with pore sizes ranging from 10 to 500 nm (Figure 3.5c, f, i). At a PVDF concentration of 12.5 wt.%, the resulting NS particles are almost entirely sheet-like with few fibers present. Cross-sectional scanning electron micrographs reveal that the membranes are of uniform thickness with a continuous pore networks through the material. SDC fibrous particles show a homogeneous pore size with relatively larger pores, where pore size and distribution on the membrane surface and its cross-section are similar, as seen from Figure 3.5 and Figure B1. NS particles tend to assemble in a specific directional way, in which the nano-sheets are parallel to the membrane surface (Figure 3.6). This organization creates a homogeneous network of very small pores (~50 nm, Figure 3.5i) on the surface, but not throughout the membrane, leading to a surface with smaller pores than the cross-section. SEM images reveals that the combination of fibers and nano-sheets in the mixed-morphology creates a disrupted pore network in all directions which is still characterized by a narrow pore distribution (Figure 3.5f)

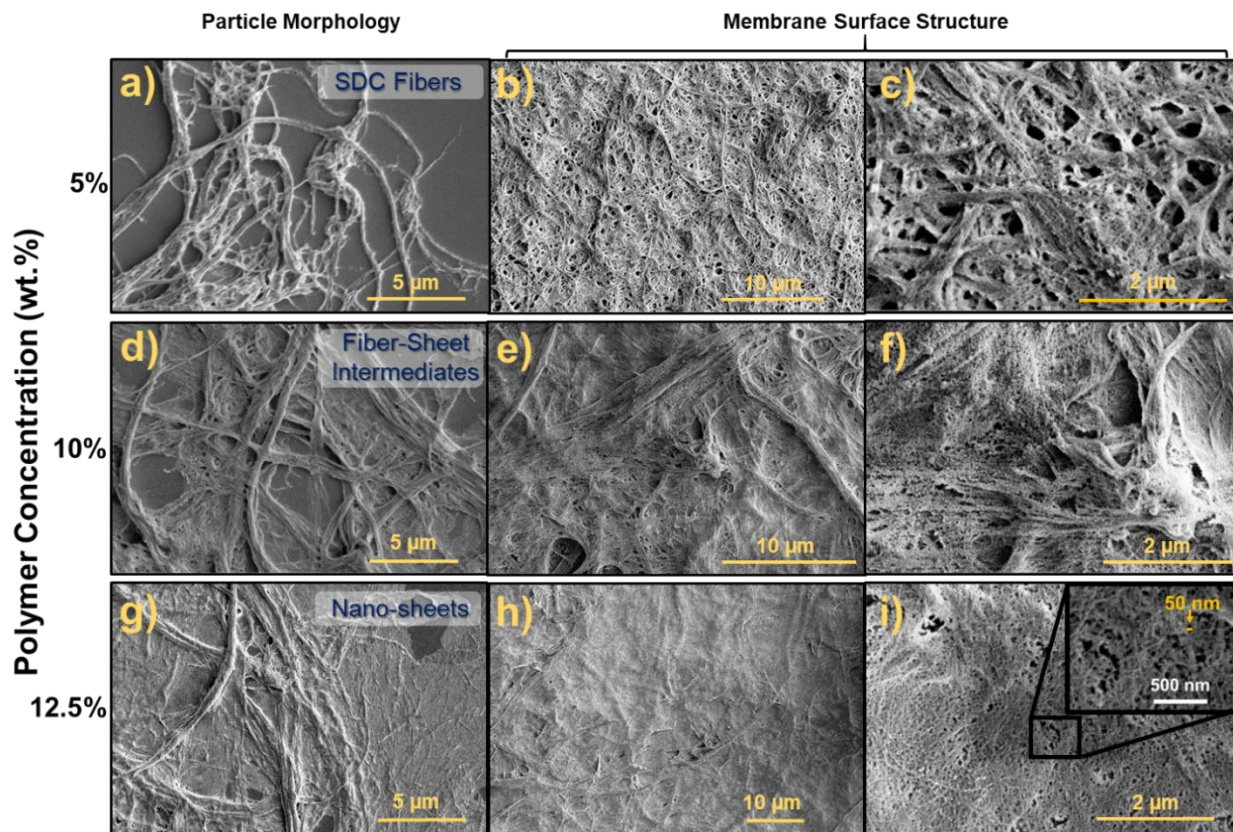


**Figure 3.5.** Microscopy of PVDF particles and their membranes. SEM images of particles and the surface features of membranes showing variation in particle morphologies, and membrane features at different magnifications of SDC fibrous (a, b, c), fibrous-NS intermediates (d, e, f) and NS membranes (g, h, i).

The morphology transition is possibly a result of the increase in polymer solution viscosity requiring more energy for droplet deformation by the nonsolvent while maintaining a similar rate of polymer precipitation, resulting in the exfoliation of thin sheets at the solvent-nonsolvent interface, shown schematically in Figure 3.6. Regardless of the morphology of the resulting particulates, the PVDF suspensions can be filtered to form porous membranes with different thicknesses (15 μm minimum).

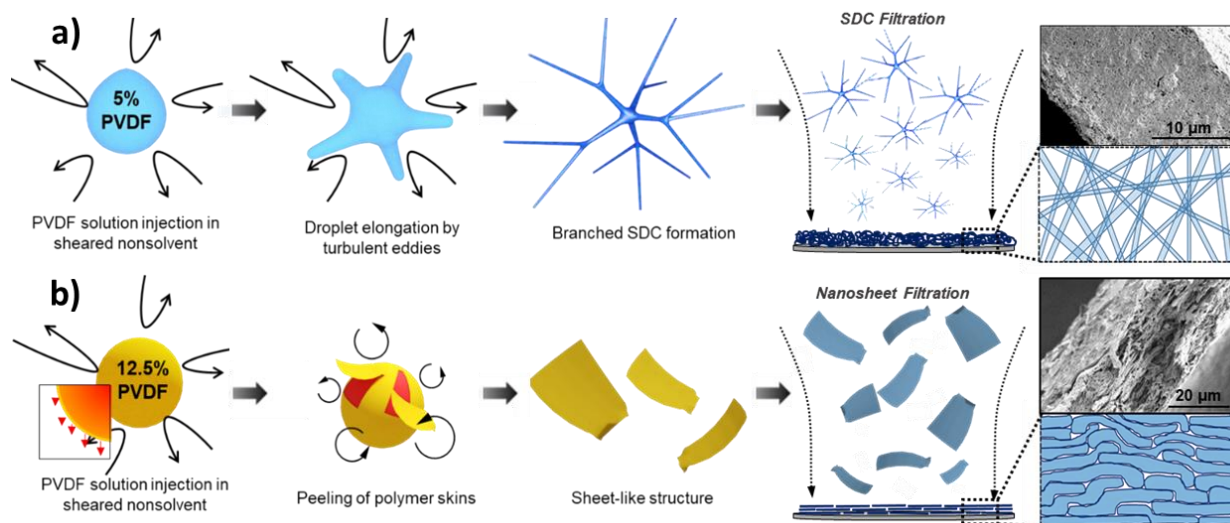


**Figure 3.6.** Schematics of shear-driven polymer precipitation showing the formation of SDC and NS membranes. (a) fibrous SDC particle fabrication and membranes from 5 wt.% PVDF in DMSO, and (b) the formation of NS particles and membranes from 12.5 wt.% PVDF in DMSO following solution injection into a turbulent EtOH flow.

### 3.3.4 Physical properties of PVDF SDC membranes

The shrinkage of PVDF SDC membranes after exposure to 90°C for 1 hour was 5.1%, comparable to that of Celgard® 2500. PVDF SDC shrinkage at 130°C and 150°C was 8.5% and 16.2%, respectively. The results shown in Figure B2 indicate that the membranes are stable at high temperatures (no wrinkles or folding) and the shrinkage is within battery operation tolerance (5% at 90°C for 1 hour).<sup>182</sup> While SDCs membranes may be suitable for this purpose, we did not investigate layered separators in this study.

A typical stress-strain curve of a PVDF SDC fibrous-NS mixed-morphology shown in Figure 3.7 indicates mechanical properties similar to those displayed by electrospun mats with elastic response and brittle fracture.<sup>22</sup> The elastic modulus of the material was 347 MPa, with >30% strain before fracture and just 0.7% offset at 1000 psi (yield stress is 5 MPa), which indicates these membranes are suitable for roll-to-roll manufacturing. We established that as the concentration of

PVDF in the injection solution increases, the elastic modulus, tensile strength, and elongation at break of the resulting membranes increase (Figure 3.7b), indicating that the membranes with more sheet-like particle morphology are more mechanically robust than those with fibrous morphology.

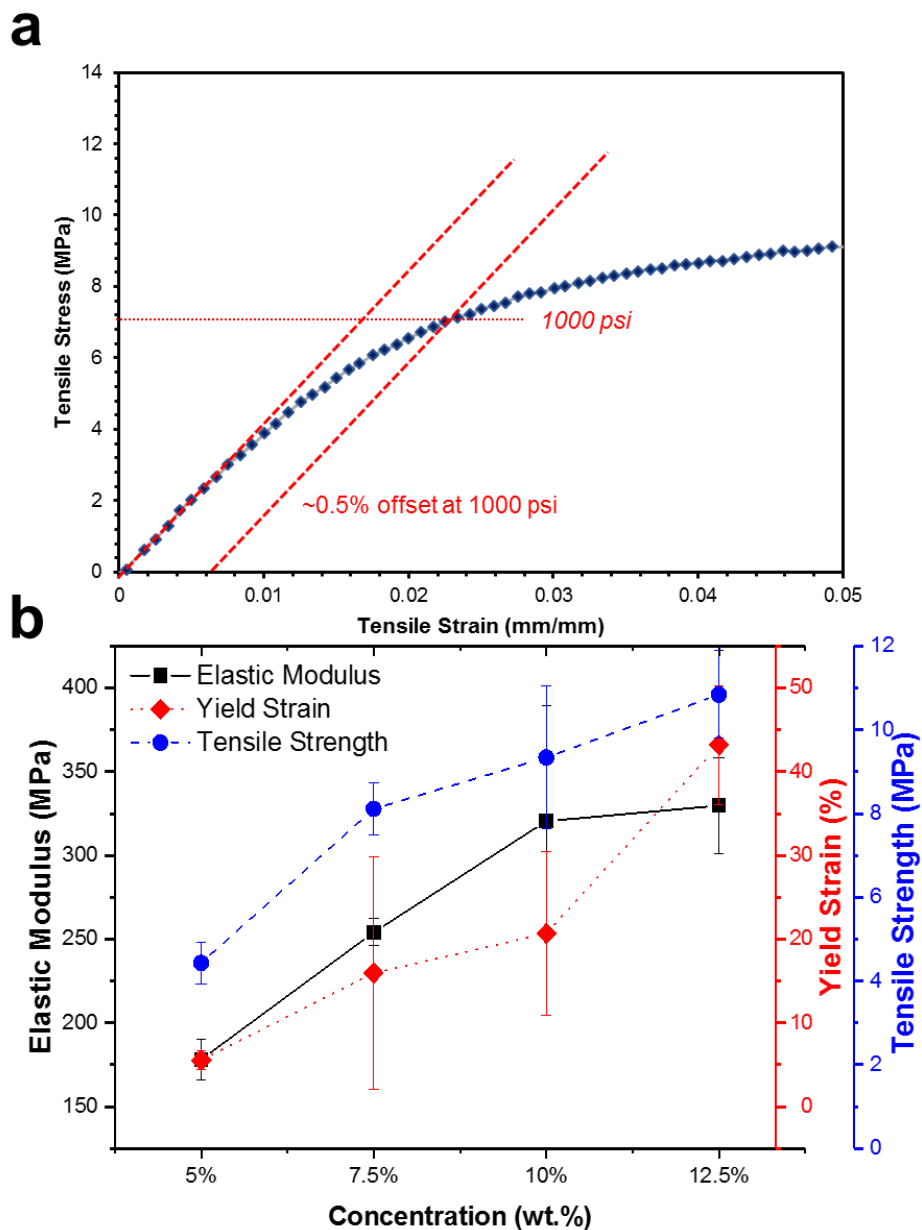


**Figure 3.7.** Mechanical properties of PVDF SDC membranes. (a) Stress-strain curve of a 48- $\mu$ m thick PVDF SDC membrane. (b) Elastic modulus, elongation at break, and tensile strength of PVDF SDC membranes dependent on the concentration of the injection solution for particle formation.

The porosities of the PVDF membranes are within the 70-80% range (Table 3.2). This range of porosity is higher than commercially available microporous battery separators (Celgard<sup>®</sup> 2500 porosity is 55%) promotes high electrolyte uptake and ionic conductivity while retaining mechanical integrity of the separator. Table 3.2 shows the average pore size and pore heterogeneity (HG) for SDC membranes obtained using capillary flow porosimetry. SDC fibrous membranes show the lowest pore size (233 nm), but their pore-size distribution is wide with an HG of 1.42. The NS morphology membranes show a slightly higher average pore size (286 nm) but a comparable distribution with a HG index equal to 1.49. The mixed-morphology membranes show a high average pore size and a narrow distribution.

**Table 3.2.** Number-average pore size ( $P_n$ ), weight-average pore size ( $P_w$ ), and heterogeneity index ( $HG = M_w/M_n$ ) of PVDF SDC membranes.

Morphology	Porosity (%)	$P_n$ (nm)	$P_w$ (nm)	HG
SDC Fibrous	78	233	331	1.42
SDC Fibrous-NS	77	451	555	1.12
NS	76	286	426	1.49

### 3.4 Conclusions

Biological research is moving away from animal models and adopting *in vitro* methods. The need for physiologically relevant *in vitro* tissue models for toxicological or other biological assessments is in high demand. The emerging advanced models are diverse, ranging from commercially available full thickness differentiated human tissues, to custom built tissue engineered models derived in single laboratories. There is a demand for better models and the ability to tailor tissue conditions for specific exposures or analyses. Commonly, a significant biomaterials challenge in the field is the dependency on structure-function relationships in materials that limit the ability of these materials to be tuned in their bulk state without altering other physiochemical parameters. Therefore, novel polymer processing techniques are needed that provide the ability to tune mechanics, microstructure, and morphology of the same bulk material independently, while providing a high degree of tailoring. Similarly, structure-property relationships are increasingly gaining interest in the design of LIB separator materials. Here we report a novel technique to create polymeric scaffolds from PU with tunable physical and mechanical properties for physiological cell culture bioscaffolds and LIB separator materials from PVDF.

Shear-driven polymer precipitation is gaining traction as an innovative and versatile technique that can manufacture tailored polymeric nanomaterials including microrods, nanofibers, SDCs, and thin sheet-like particles from both synthetic and biopolymer materials.<sup>60,62,65</sup> PU is commonly used in medical devices due to its low elastic modulus and high degree of biocompatibility. The SDCs were produced in a rapid and scalable precipitation process (Figure 3.1, Figure 3.6). The phenomena involved include the rate of polymer precipitation dictated by the chemical potential gradient between the solvent and nonsolvent phases as well as the hydrodynamic characteristics of the turbulent flow and injection solutions, which are impacted by

the viscoelasticities of the solvent and nonsolvent phases.<sup>66</sup> The addition of 20 vol.% Gly to the EtOH nonsolvent affects the chemical potential gradient controlling the rate of polymer precipitation at the polymer – nonsolvent interface compared to that of a pure EtOH nonsolvent, but it also increases the viscosity of the nonsolvent nearly 5-fold.<sup>183</sup> The PU SDCs prepared using EtOH as nonsolvent exhibited thicker fibers than the previously reported SDCs composed of other synthetic polymers, yet had the same characteristic, branched-fiber structure. Microscopy of these particulates reveals that these thicker fibers appeared to be analogous to aggregated “braids” of smaller fibers (Figure 3.2).

Similarly, we show morphological control over the PVDF particulate morphologies by adjusting the concentration of the polymer in the injection solution rather than the composition of the nonsolvent medium, with lower relative concentrations of PVDF at 5 wt.% in DMSO producing more fibrous SDCs and higher concentrations of 12.5 wt.% producing NS particulates (Figure 3.5). It is notable that at 5 wt.% in DMSO, the PVDF is liquid with low viscosity, but an increase to 12.5 wt.% begins to gel the PVDF in DMSO injection solution after it undergoes dissolution at 110°C and cooling to room temperature. We hypothesize that the injected solutions viscosity increase isn't as readily templated by the streamlines of the nonsolvent medium, instead producing polymer “skins” at the solution – nonsolvent interface that are readily exfoliated.

While the control of fiber diameter displayed here is a common feature in both melt-blowing and electrospinning, shear-driven precipitation is a versatile technique which is capable of producing many further controlled particle morphologies beyond nanofibers including nano-scale sheet particulates and ribbons.<sup>65</sup> Membranes prepared from SDC form porous membranes that are cohesively connected by the SDC fiber sub-contacts (Figs. 3.3, 3.7). The mechanical entanglement of the PU SDC fibers resulted in continuous mat with highly anisotropic pores in

both geometry and size, offering a favorable environment for cell attachment and proliferation.<sup>166,184</sup> The PVDF particulate and membrane pore sizes, however, were both much smaller, with pore sizes in the range of hundreds of nanometers (Table 3.2). Analysis of the PU SDC membranes by X-ray nanotomography revealed that the Soft and Stiff PU SDC substrates had a pore volume of ~70%, very similar to that of the PVDF membranes despite the difference in scale of their pore sizes. This high porosity in PU SDC membranes may further benefit cellular response, as many similar nanofibrous membranes produced most commonly by electrospinning see decreased cell invasion and sub-optimal cell response due to the smaller pore size of electrospun nanofiber matrices.<sup>162</sup> X-ray nanotomography also allows visualization of the internal, disordered pore network of the nonwoven with features ranging from microns to hundreds of microns. The analysis reveals that the pores of the Soft SDC nonwovens exhibited a slightly higher average Feret diameter (1072  $\mu\text{m}$ ) than those composed of Stiff SDCs (1322  $\mu\text{m}$ ) despite the smaller diameter of their fibrillar features (Table 3.1). Thus, the SDCs described here offer a novel solution to developing mechanically robust, highly porous, biocompatible, and tunable substrates for future in vitro investigations of cellular biology. Future improvements in the thickness and reduction of pore size could further enhance these scaffolds.

The low elastic moduli of PU SDC nonwovens indicate that they are very soft materials with moduli below 1 MPa and surprisingly good mechanical integrity. After 5 cycles of 30% strain, representative stress-strain curves show that both Soft and Stiff PU membrane exhibited elastic modulus relaxation and some membrane creep, although the ability of SDC membranes to withstand 5 cycles of supraphysiological stress from 50% strain proved the integrity of the SDC membrane as tissue substrates (Figure 3.4). Despite their identical chemical composition, the Soft PU nonwovens exhibited much lower tensile moduli that leveled off at ~200 kPa compared to the

Stiff PU membranes with moduli that reached ~750 kPa (Figure 3.4c). Both the Soft and the Stiff PU SDC membranes exhibited tensile elastic moduli within the range of healthy (0.5 – 250 kPa, human lung) and diseased (50 – 900 kPa, human fibrosis) tissue, respectively.<sup>185</sup> Membrane elasticity similar to aligned or randomly oriented electrospun fiber mats decreased with increasing individual fiber diameter.<sup>186</sup> For both Stiff and Soft PU SDC nonwovens, the tensile moduli of membranes during the strain ramp were nearly 2× larger than those reached after the membranes underwent 50% cyclic strain.

We hypothesize that the smaller fibers of the Soft PU SDCs may form weaker networks that are more easily ruptured than those of the Stiff PU SDCs. The biocompatibility, softness, and porosity of the fibrillar SDC nonwovens makes them potentially valuable biomimetic cell scaffold materials for soft, physiological tissues.<sup>187</sup> Moreover, the tunability of the processing technique provides a means to selectively optimize scaffold mechanics and microstructure independent of chemistry, thus providing a consistent and controllable platform for biological investigations.<sup>161</sup>

This method can also be conveniently and efficiently adapted for producing LIB separators not only because of the scalability of the process, but also the versatility by which nanofibrous and sheet-like particles can be produced from a variety of polymers. Producing these extremely high aspect ratio particles from different polymers allows the facile formation of membranes with a network of fibers or sheets tortuous enough for high electrochemical stability in LIBs, and has the potential to be easily adapted to other battery technologies as well. All PU and PVDF particle morphologies formed membranes with 70-80% porosities. The membranes comprised of more fibrous particles show less ordered pore networks in both the PU and PVDF systems. In PVDF membranes, the sheet-like membranes showed better mechanical properties with nearly 100% increases in tensile strength and elastic modulus and yield increasing nearly five-fold compared to

the PVDF SDC membranes (Figure 3.7). This data indicates that the layered NS membrane morphology is capable of dissipating far more energy before undergoing brittle fracture compared to more fibrous architectures.

Overall, SDCs can form the basis of novel fibrillar materials with tailored microstructural and mechanical parameters necessary for applications requiring emulating human physiology and biological responses. The morphology of the membranes determines the performance and can be adjusted to the specific application, *e.g.* by purposefully mixing particles of two distinct morphologies, mixing SDCs of different polymers in suspension prior to filtration (Chapter 4), or layering SDCs within the membrane, a technique commonly utilized in LIB materials.<sup>188</sup> The inherent versatility in choice of polymer offered by the shear-driven precipitation technique enables the high-throughput development of similar SDC membranes produced from other polymers including biodegradable and bio-derived polymers. This allows making membranes of tailored mechanical and physical properties that can find any number of addition to their utilization as synthetic tissue substrates to measure cell toxicology.<sup>189,190</sup>

## **CHAPTER 4: Soft Dendritic Colloid Superhydrophobic and Anti-Icing Surface Coatings**

## 4.1 Introduction

The engineering of surfaces with advanced wetting, self-cleaning, anti-corrosive, and anti-icing properties has been a topic of intense research interest for decades.<sup>191–194</sup> The research studies aimed to produce superhydrophobic surfaces have focused on modifying and reducing the surface energy of the substrate as well as achieving the desired surface roughness to trap air pockets between the water droplet and the surface to force droplets into a Cassie-Baxter state.<sup>195–197</sup> Polymeric coatings seeking to mimic the “lotus leaf effect” with low surface energies and hierarchical surface roughness produced by microphase separation, sol-gel processes, and electrospinning can commonly achieve superhydrophobicity with apparent water contact angles greater than  $150^\circ$  and low tilt angles that promote water droplet roll-off.<sup>17,198–200</sup>

A common strategy to fabricate surfaces with anti-icing properties has been to utilize these hierarchical, superhydrophobic surface architectures to reduce ice accumulation by decreasing the contact area between the surface and impinging water droplets and delaying the thermal conduction between the surface and the droplet that lead to heterogeneous ice nucleation.<sup>19,201–206</sup> Coating architectures with hierarchical features on both the micro- and nano-scales have been found to maximize liquid repellency promoting droplet roll-off, delay ice nucleation in static water droplets, and in some cases reduce ice adhesion strength.<sup>207–210</sup> Chemically-modified polymeric coatings are often limited by their low scalability and can be subjects to fouling of the coating or mechanical abrasion, which lead to reduced functionality.<sup>211</sup> To mitigate this deterioration, one strategy is to create materials of low surface energy throughout the bulk coating material as opposed to confined at the surface so that mechanical abrasion and coating exfoliation do not remove the thin hydrophobic surface layer and instead, only reveals more hydrophobic material and maintains superhydrophobicity.<sup>212,213</sup>

Here, we present novel classes of nanofibrous polymeric surface coatings and porous, nanofibrous sheets made of soft dendritic colloids (SDCs). SDCs are a hierarchically structured nanomaterial with branched fibers spanning up to three orders of magnitude in length surrounding the core of the particulate. A major advantage to utilizing SDCs compared to other nanofiber production methods is that SDCs inherently are produced in suspension as opposed to being confined to a 2D fiber mat as a byproduct of their production. Dispersing SDCs in a volatile medium such as ethanol (EtOH) followed by simply casting that suspension on a surface is a method that could be adapted to easily produce porous coatings that exhibit strong physical adhesion regardless of surface geometry. Given time for evaporation of the volatile alcohol medium, SDC suspension casting enables the facile formation of highly porous and nanofibrous surface coatings (Figure 4.1). The characteristic morphology of SDCs results in a robust, self-assembling adhesive network due to a mechanism analogous to the contact-splitting phenomenon exhibited by gecko lizards.<sup>65</sup>

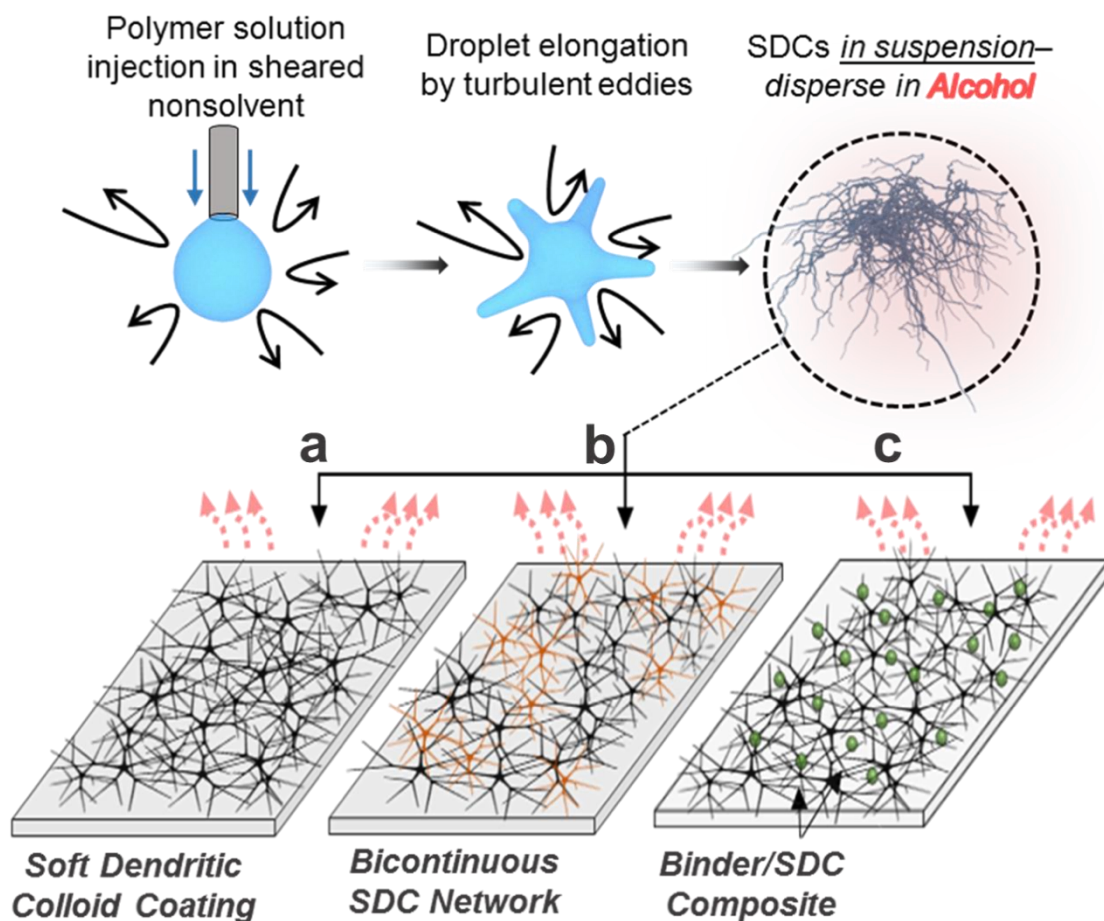


**Figure 4.1.** Schematic of SDC coating formation. Diagrams illustrating SDC production, re-suspension in alcohol, and the casting of (a) pure SDC, (b) bicontinuous network SDC, and (c) SDC/binder composite surface coatings.

Here, we show that SDC coatings can be prepared from a range of polymers of varying chemical compositions and that the wetting properties and mechanical characteristics of the SDC coating are dependent on the polymer comprising the SDCs. Moreover, the topographically overlapping fibers, inherent to SDC coatings, amplify the hydrophobicity or hydrophilicity of the surface with SDC coatings produced from hydrophobic and hydrophilic polymers capable of exhibiting superhydrophobicity and superhydrophilicity, respectively. SDC coatings comprised of hydrophobic polymers exhibit anti-icing properties, including increased ice nucleation time and decreased ice adhesion strength. However, SDC adhesion and superhydrophobicity show mutual

exclusivity for SDC coatings composed of a single polymer evidenced by the mechanical properties of nonwoven sheets prepared from the SDCs. To mitigate the inherent inverse relationship between strong mechanical integrity and superhydrophobicity, the formation of bicontinuous SDC networks and adding an emulsified, elastomeric polydimethylsiloxane binder are presented as two strategies to improve the desired SDC coating properties.

## 4.2 Materials and Methods

### 4.2.1 SDC fabrication and coating casting

SDCs from polystyrene (PS, Sigma-Aldrich,  $M_w = 230$  kDa), polyester (PES, Eastman Ecdel 9966), and polyvinyl alcohol (PVOH, Mowiol 18-88, 100 kDa) were fabricated using the polymers, solvents, and nonsolvents systems listed in Table C1. PVOH SDCs were further cross-linked with glutaraldehyde following suspension in acetone to render them insoluble in water (Appendix C). Following fabrication, the resulting SDCs were centrifuged at 3.0 rcf for 2 minutes to form a concentrated pellet, the supernatant was discarded, and the SDCs were resuspended in ethanol (EtOH, Koptec) to 8× the pellet volume. This was repeated 3× to remove remaining nonsolvent from the dispersion. SDC coatings were prepared by casting 1.0 wt.% SDC suspensions in EtOH over the substrate and drying in a 50°C oven for 24 hours.

### 4.2.2 Polydimethylsiloxane binder for SDC coatings

Polydimethylsiloxane/SDC composite coatings were prepared by mixing polydimethylsiloxane (PDMS, Sylgard 184) base with its curing agent (10:1 ratio) and leaving at room temperature for 10 mins before emulsifying the PDMS in EtOH at (1 wt.% PDMS) using a 1 cm stir bar at 1200 rpm. Immediately prior to casting, the PDMS emulsion was added to the 1.0 wt.% SDC suspension in EtOH, mixed for 1 min using a Vortex mixer and cast onto the substrate. The drying process at 50°C served to both remove the alcohol medium and cure the PDMS microdroplets within the composite. Coating thickness was determined by removing the coating with a razor blade and measuring the thickness using a handheld micrometer (Marathon).

### 4.2.3 Wetting and anti-icing properties of SDC coatings

Contact angle measurements were determined by dispensing 10  $\mu$ L water droplet using a goniometer (First Ten Angstroms). Contact angle hysteresis was calculated by subtracting the

receding from the advancing contact angles measured by adding and removing water from the deposited droplet and video analysis of the contact angles by First Ten Angstroms software. Ice nucleation times were calculated by depositing 10  $\mu\text{L}$  of Milli-Q water onto substrates equilibrated on a  $-10^\circ\text{C}$  Peltier plate (Linkam PE-94), videotaping the droplet nucleation process, and using image analysis to measure heterogeneous ice nucleation time. Ice adhesion strengths were calculated by adopting a previously utilized method in which hydrophobic polypropylene tips (Fisherbrand 0.1-10 mL, 4 mm diameter, 50  $\mu\text{L}$  water) were utilized as ice molds. Following deposition of water into the molds, SDC coatings on aluminum substrates were placed on the Peltier plate maintained at  $-10^\circ\text{C}$  for 10 minutes. Adhesion strength was determined by attaching a force gauge (HF-30N) to a modified syringe pump (NE-4000) and removing the ice mold at a speed of 0.5 mm/second. The ice adhesion strength was calculated by Equation 4.1, where  $P_{ad}$  is the adhesion strength and  $d$  is the diameter of the ice mold.<sup>214</sup>

$$P_{ad} = \frac{4F_{ad}}{\pi d^2} \quad (4.1)$$

#### 4.2.4 Microscopy of SDC Coatings

Optical microscopy (BX-61, Olympus) and field emission scanning electron microscopy (Verios 460L, FEI) were performed to visualize particle and coating structures. Electron microscopy was performed after sputter coating 7 nm of a gold/palladium alloy on the surface of the SDC or coating.

#### 4.2.4 SDC sheet formation for mechanical analysis

A useful method of comparing the durability and toughness of SDC coatings is to form a mechanically robust and porous sheet from the SDC matrix comprising the coating. This was achieved by filtering SDC suspensions in EtOH onto a polyvinylidene fluoride filter (0.45  $\mu\text{m}$ ,

Durapore). Once filtered, SDC sheets were dried for 24 hours at 50°C to remove residual EtOH and were cut into 10 mm strips. The mechanical properties of the nonwovens were then measured using a common testing machine (Instron 5943) with a crosshead speed of 5 mm·min<sup>-1</sup>.

## 4.3 Results

### 4.3.1 Wetting properties of SDC coatings

Scanning electron micrographs shown in Figure 4.2 illustrate the structures of SDCs and SDC-coated glass slides from each polymer, where it is seen that the entangled fibers of adjacent SDCs form a highly porous, continuous fiber network on the substrate. This fibrous coating architecture results in surface topography with multi-scaled features on the micro- and nano-scale, a characteristic of superhydrophobic and liquid-repellent surfaces.<sup>210</sup> To investigate the effect of SDC surface roughness on the wetting behavior, the water contact angle (WCA) was first determined on thin uniform films composed of polystyrene (PS), polyester (PES), and polyvinyl alcohol (PVOH) prepared by spin-coating and compared to those of SDC coatings prepared from the same polymers (Table 4.1). The large difference in the static contact angle of a water droplet on thin films and SDC coatings composed of the same polymer shows that this surface topography amplifies the wetting properties of the coating consistent with the Wenzel model<sup>215</sup>, with PS and PES SDC coatings exhibiting more hydrophobic behavior, while the hydrophilic PVOH SDC coating becomes superhydrophilic, actively spreading the water droplet after deposition.

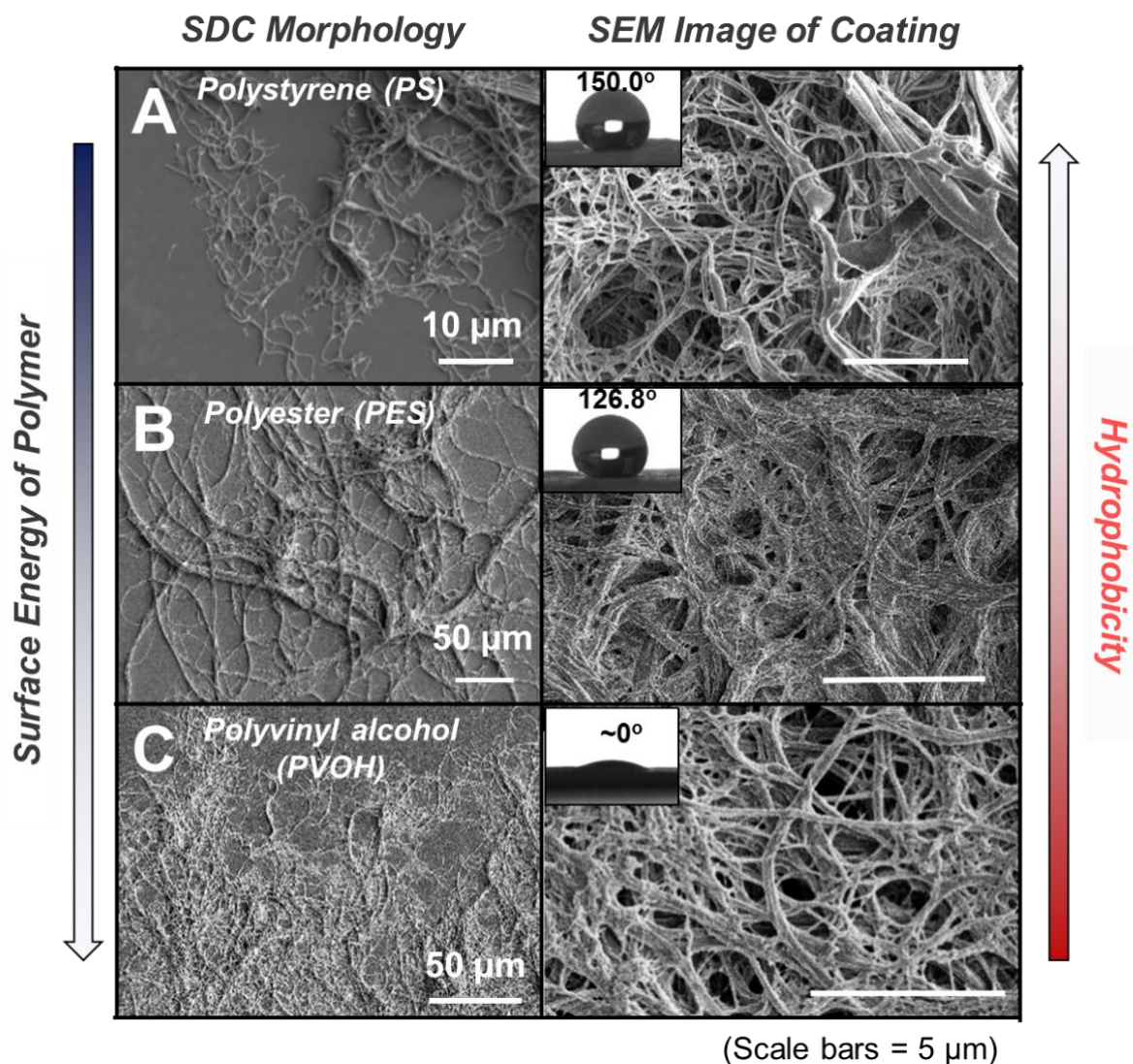


**Figure 4.2.** Microscopy of PS, PES, and PVOH SDCs and their coatings. Scanning electron micrographs of (a) PS, (b) PES, and (c) PVOH SDCs and SDC coatings with inset images showing representative water contact angle on each coating.

**Table 4.1.** Summary of data for water contact angle on thin films and SDC coatings of different polymers and porosities of SDC coatings.

Polymer	Thin Film WCA (°)	SDC Coating WCA (°)	Porosity (%)
Polystyrene (PS)	100.7 ± 1.8	150.1 ± 5.0	92.49 ± 1.35
Polyester (PES)	75.5 ± 1.2	126.8 ± 5.7	80.47 ± 1.10
Polyvinyl alcohol (PVOH)	57.4 ± 5.6	~ 0	23.18 ± 5.07

The simplest model of cohesion and adhesion, the Dupré equation, describes how the work of cohesion and adhesion between two species is directly related to the surface energy of one or both materials.<sup>216</sup> With lower surface energies, the more hydrophobic PS and PES SDCs show decreased cohesion within the bulk network and yield higher coating porosities with values over 80%. A useful way to quantify the durability of SDC coatings is to prepare nonwoven SDC sheets by filtering SDC in EtOH suspensions onto filter pads and removing the SDC coating from the surface after drying. Tensile analysis can then be directly performed on the SDC sheet and the mechanical properties like elastic modulus and toughness of the SDC nonwovens can be correlated to the coatings prepared from the same SDCs (Figure C1). The data shown in Table 4.2 outline the SDC nonwovens' mechanical properties for PS, PES, and PVOH SDC sheets.

**Table 4.2.** Mechanical properties of porous SDC sheets composed of PS, PES, and PVOH.

Polymer	Modulus (MPa)	Strength (kPa)	Toughness (kPa)	Elongation (%)
PS SDC	7.84 ± 1.16	120 ± 20	1.74 ± 0.60	2.40 ± 0.51
PES SDC	30.6 ± 14.8	277 ± 11	604 ± 113	29.8 ± 4.16
PVOH SDC	110 ± 2.22	295 ± 78	62.5 ± 39.8	3.41 ± 1.17

The results of the tensile analysis of the SDC sheets show that the PS SDC network, while quite hydrophobic, is very soft with very low toughness. The tensile moduli of the PES and PVOH SDC nonwovens seem to follow an inverse trend with the porosities data shown in Table 4.1. This trend suggests that the surface energy of the material comprising SDCs determines the cohesive packing of fibers within the film and suggests that generally, lower surface energy polymers will yield SDCs coatings with higher porosities, but lower stiffness and toughness.<sup>217,218</sup> While the PVOH SDC nonwoven displays the maximum stiffness (110 ± 2.22 MPa), the PES SDC nonwoven shows greatly increased toughness (604 ± 113 kPa) compared to those of PS and PVOH.

This is likely due to the PES being far above its  $T_g$  of  $-40^\circ\text{C}$  and the PES polymer exhibiting much higher elasticity at room temperature compared to the glassy PS and PVOH polymers. Following these considerations, strong adhesion and superhydrophobicity for pure SDC coatings show mutual exclusivity, with SDCs composed of low surface energy polymers making coatings with weaker adhesion to the substrate and cohesion throughout the network, rendering them more prone to mechanical abrasion, but also exhibiting higher superhydrophobic properties.

#### 4.3.2 Bicontinuous Soft Dendritic Colloid Networks

The formation of bicontinuous nanofibrous networks by simply mixing SDC in EtOH suspensions of different polymers prior to coating deposition is a technique that could improve and tailor the resulting coating properties. The properties of these systems were investigated based on a model system consisting of a blend of PS and PVOH SDCs because PS SDCs show superhydrophobic behavior (Figure 4.3a), but lack durability, while PVOH SDC form mechanically robust networks, but have high hydrophilicity. The electron micrograph of a bicontinuous PS/PVOH SDC (50/50 w/w) coating in Figure 4.3b shows that the highly entangled fibers of the bicontinuous network are visually indistinguishable. The mechanical properties of bicontinuous PS/PVOH SDC networks were analyzed by performing tensile analysis on SDC sheets of the same composition. The composite PS/PVOH nonwoven exhibits a tensile modulus roughly  $3\times$  and toughness roughly  $5\times$  larger than that of the PS SDC nonwoven, while the elongation at break is not affected significantly (Fig 4.3c-d).

The apparent water contact angles were determined by goniometry and the droplet ice nucleation times were defined as the time necessary to see heterogenous ice formation completely permeate a  $10\ \mu\text{L}$  water droplet. When measured using lap shear strength testing (Appendix C), the PS/PVOH SDC blends exhibit adhesion trends that follow an approximately linear relationship

between the adhesion values recorded for pure PS and PVOH SDCs (Figure C3). However, the relationship between both the droplet freezing times and the apparent contact angles in Figure 4.3e do not follow the same linear trend. Both the apparent contact angle and the droplet freezing time values for a coating composition of 75/25 (w/w) PS/PVOH SDCs are nearly the same as those of the pure PS SDC coating. At this composition, the adhesion of the coating measured by lap shear strength increased nearly 50% compared to that of PS SDCs alone.

The blended PS/PVOH SDC network achieves surface wetting and ice retardation properties that nearly match that of a PS SDC coating, while also gaining the benefits of high mechanical integrity due to the incorporation of PVOH SDCs into the SDC network. The ice adhesion strengths to SDC and SDC composite coatings were determined as described previously (Figure C4).<sup>214,219,220</sup> The pure PS SDC coating showed very low toughness, such that the removal of the ice mold resulted in coating damage and tearing off from the aluminum substrate (labeled adhesive failure), while the pure PVOH SDC coating had both increased ice adhesion and nucleation rate as the droplet had large contact area with the cooled substrate as it spread over it. The bicontinuous PS/PVOH (75/25 w/w) SDC coating, however, saw an ice nucleation time consistent with the pure PS coating, but exhibited a five-fold reduction in ice adhesion strength (~200 kPa) compared to the aluminum substrate control (Figure 4.3f).

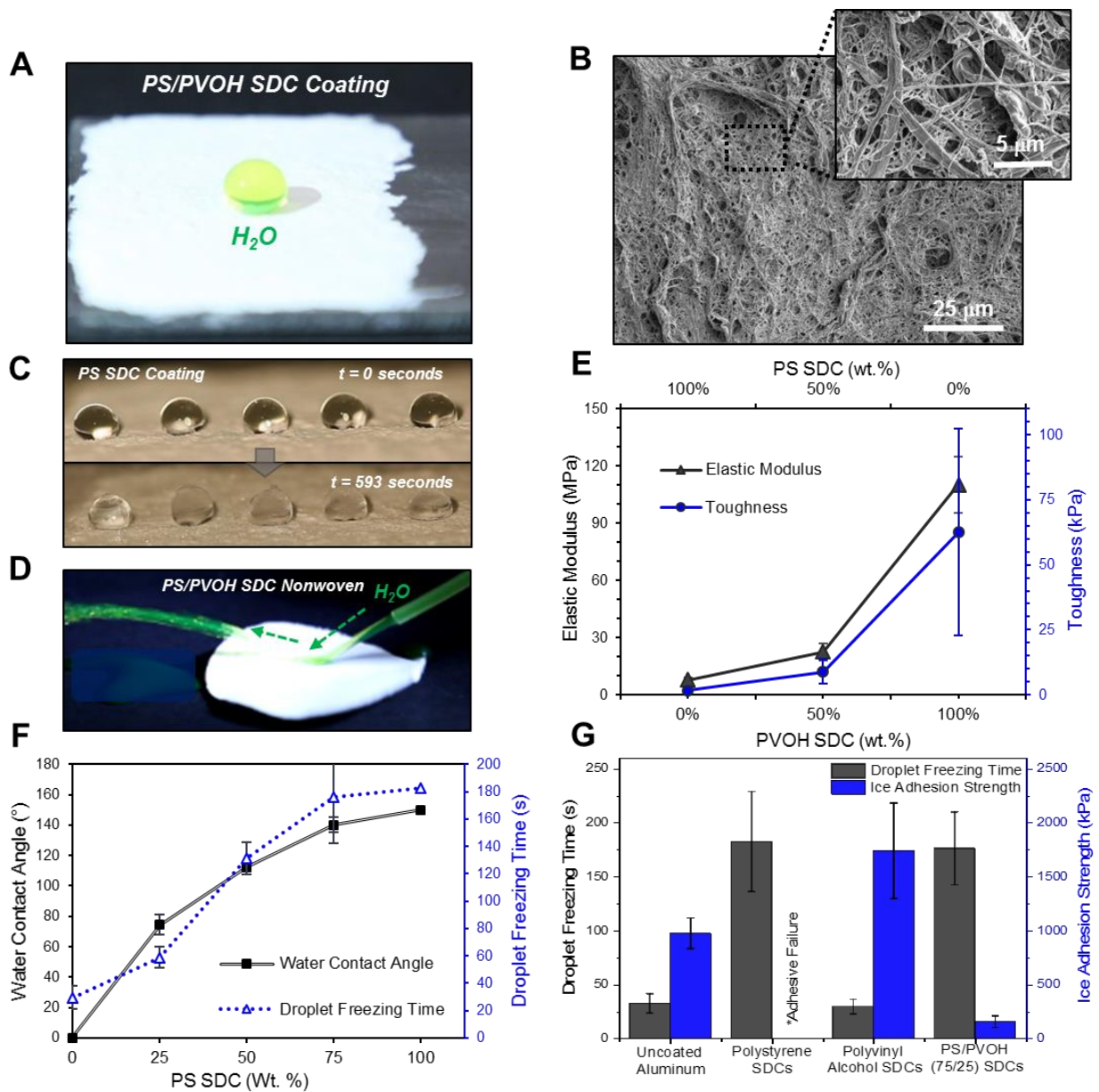


**Figure 4.3.** Wetting and anti-icing properties of PS/PVOH bicontinuous SDC coatings. (a) Picture and (b) SEM images of a PS/PVOH (50/50) blended SDC coating. Pictures of (c) Heterogenous nucleation of water droplet on a PS SDC coated Al substrate and (d) demonstration of water repellency of a PS/PVOH SDC nonwoven. (e) Elastic modulus and toughness of PS/PVOH SDC nonwovens of varying composition. (f) Apparent contact angle (black) and droplet freezing time (blue) vs. PS wt.% for PS/PVOH bicontinuous networks of  $2 \text{ mg/cm}^2$  ( $n=10$ ). (g) Droplet freezing time (black) and ice adhesion strength (blue) aluminum, PS, PVOH, and PS/PVOH SDC coatings of  $2 \text{ mg/cm}^2$  ( $n=10$ ).

### 4.3.3 Polydimethylsiloxane microdroplet binder for SDC coatings

PES SDCs exhibit excellent durability and high WCAs ( $>125^\circ$ ) both in the form of surface coatings and porous SDC sheets (Fig 4.4a-b). The addition of an elastomeric polydimethylsiloxane (PDMS) binder to an SDC coating could also be a way to improve the hydrophobic and anti-icing properties of SDC coatings. The addition of the PDMS slightly decreases the apparent WCA of the PES/PDMS SDC coating, but the contact angle hysteresis (CAH) of the composite coating reaches a minimum at 30 wt.% PDMS (Figure 4.4e). Because PDMS (WCA  $\sim 90^\circ$ ) is slightly more hydrophobic than the PES thin film (WCA =  $75.5 \pm 1.2^\circ$ ), we hypothesize that at low concentrations, the PDMS microdroplets within the coating decrease the average surface energy of the heterogenous coating, but also incrementally reduce the surface roughness created by the overlapping SDC fibers. The scanning electron micrographs shown in Figure 4.4c-d elucidate that as the PDMS concentration in the coating increases, small PDMS droplet moieties appear distributed at fiber-fiber and fiber-substrate interfaces. At higher concentrations of PDMS, the addition of the elastomeric binder suppresses the fiber surface roughness and the CAH begins to increase beyond its minimum value seen at 30 wt.% PDMS (Figure 4.4e). A low CAH has been shown to be a design parameter indicator for surfaces with low ice adhesion strengths, so the anti-icing properties of this formulation were investigated further.<sup>196</sup>

The pure PES SDC coating demonstrated a nearly  $3\times$  increase in the droplet freezing time compared to the uncoated aluminum control, but only resulted in a minor reduction in ice adhesion strength. However, the PES/PDMS composite showed greatly increased droplet freezing times and decreased ice adhesion strength ( $\sim 400$  kPa) compared to any SDC coating composed of a single polymer. The increase in droplet freezing time with the mass (and thus, thickness) of the deposited PES and PS SDC coatings was roughly linear (Figure C5), with PS SDCs showing a more efficient

anti-icing effect by significantly delaying water droplet freezing times. This suggests that SDC coatings exhibit anti-icing properties through both hydrophobic and insulation effects, as heat flow through the highly porous PS and PES SDC coatings (Table 4.1) would be greatly reduced, with the more porous PS SDC coating displaying a greater reduction than the PES SDC coating.

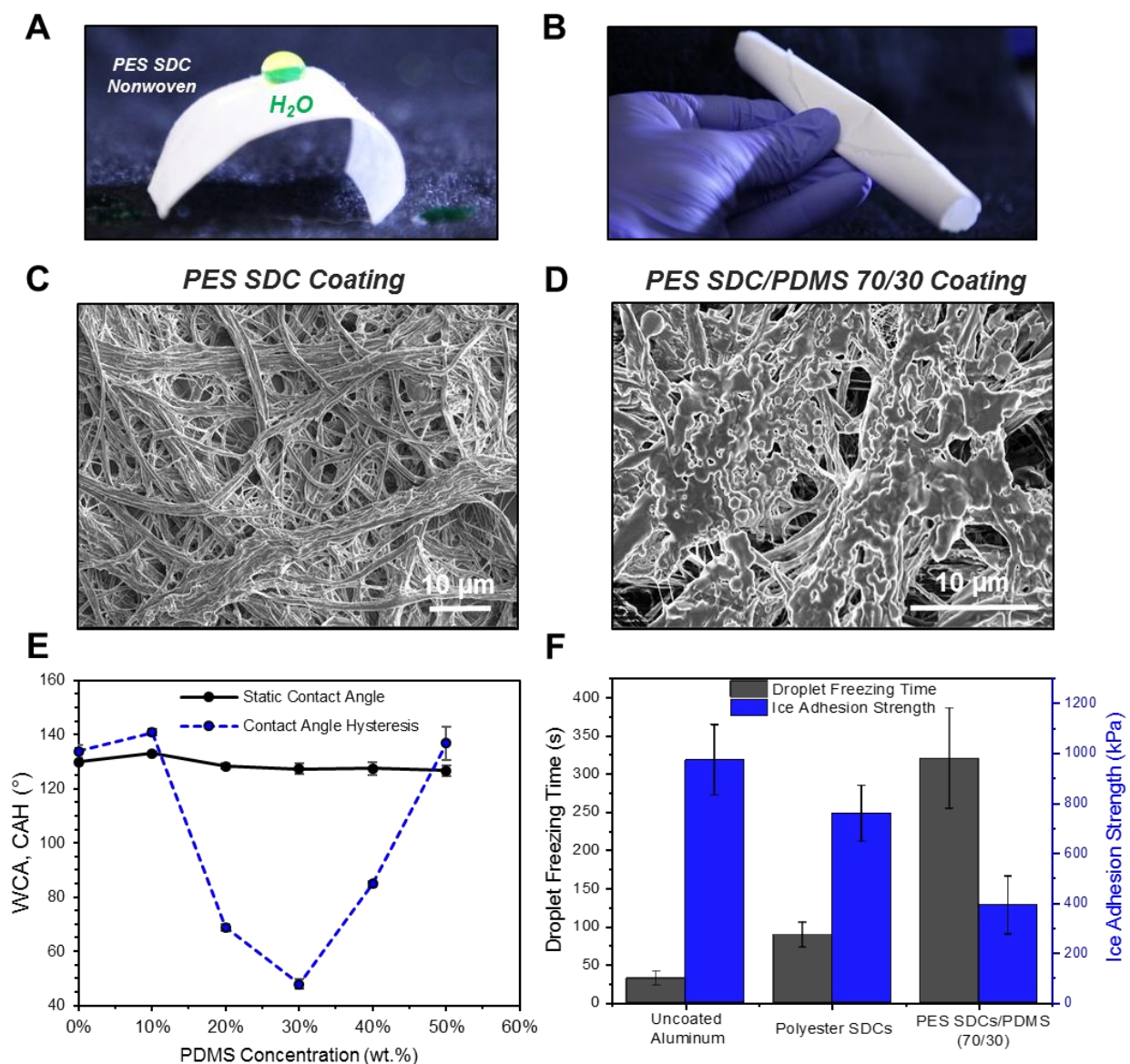


**Figure 4.4.** Wetting and anti-icing of PES SDC/PDMS composite coatings. (a) Pictures of PES SDC membranes. (b) Pictures of water droplets on a PES/PDMS coating. (c) PES SDC/PDMS (70/30 w/w) coating and (d) PES SDC coating scanning electron micrographs. (e) Static WCA and contact angle hysteresis on PES SDC/PDMS coatings of varying composition (n=5) (f) Droplet freezing time and ice adhesion strength for uncoated aluminum, a PES SDC coating, and a PES SDC/PDMS (70/30) composite coatings. ( $2 \text{ mg/cm}^2$ , n=5).

#### 4. 4 Conclusions

We investigated the wetting behavior and anti-icing potential of SDC surface coatings composed of polymers of different chemical properties. The highly branched fibrous structure of the SDCs allows them to physically adhere strongly to nearly any surface regardless of its topography. The SDC networks also display strong cohesion, allowing the scalable production of surface coatings and nonwovens from an enormous library of polymer materials. We show that the hierarchical morphology of the SDC coatings amplify their wetting properties depending on the chemistry of the material comprising the SDCs, due to the surface roughness granted by the overlapping fibers. Low surface energy polymers result in more hydrophobic SDC coatings with higher porosity, but low toughness.<sup>204,205</sup> Higher surface energy polymers generally produce superhydrophilic SDC coatings with lower porosity and hydrophilic behavior, but higher toughness and resistance to mechanical abrasion.

The strong adhesion and superhydrophobicity of pure SDC coatings may be somewhat mutually exclusive, but this inherent design challenge can be mitigated by two strategies presented here; making either bicontinuous SDC coatings comprised of a blend of polymer SDCs, or addition of an elastomeric microdroplet binder. Concurrently, we show that SDC and SDC composite coatings show anti-icing properties, namely – increased ice nucleation time due to reduced contact area and heat transfer from the surface to the droplet and decreased ice adhesion strength.<sup>221</sup> Coupled with the increased droplet roll-off due to the highly hydrophobic surfaces increased droplet. As the technique of shear-driven polymer precipitation is expanded further to produce novel, nanostructured materials from more polymer materials, the principles discussed herein will provide insights into the choice of polymer(s) comprising the SDC coatings to result in coatings with tailored surface and mechanical properties.

Many electrospun nanofiber coatings achieve improved superhydrophobic and anti-icing performance through the incorporation of colloidal nanoparticles to the fibers. While that approach was not discussed herein, the shear-driven precipitation technique can achieve facile incorporation of colloidal particles into unidirectional nanofibers and we hypothesize that composite SDCs containing hydrophobic and/or ceramic nanoparticles could be fabricated by dispersing these materials in the polymer injection solution.<sup>62</sup> Furthermore, SDC coatings can undergo some abrasion and surface exfoliation without undergoing fouling, as the SDC material in the bulk coating is chemically and topographically identical to that at the surface.<sup>212,213</sup> Ultimately, the highly controllable wetting and anti-icing properties of SDCs, combined with the scalability of their production, and the library of different polymer chemistries from which SDCs can be fabricated, enable the fabrication of a multitude of high-performance SDC coatings for both large-scale and specialty applications.

## **CHAPTER 5: Layer-By-Layer Polyelectrolyte Nanocoatings for Food-Grade Barrier Films**

## 5.1 Introduction

Many food and pharmaceutical products are negatively affected by environmental factors such as heat, light, humidity, oxygen, and microbial activity.<sup>222</sup> One approach to alleviate this problem has been the development of coatings applied onto packaging or directly onto the product surface to prolong the product's viability and delay mechanical, chemical, or biological fouling. For direct coating application on food products, the necessity of the coating to be edible limits the number of materials that can be used to comprise the coating.<sup>223–225</sup> Several different techniques have been identified as scalable and viable means to produce edible barrier coatings one of the most prominent of which is layer-by-layer film deposition (LbL). LbL is a technique that has been used extensively to produce polyelectrolyte multilayers (PEMs).<sup>68,226</sup> To construct these films, a substrate is dipped into a cationic polymer solution followed by rinsing and dipping in the polyanionic solution. The cationic polymer molecules adsorbed on the substrate in the first step interact with the polyanionic molecules of the second solution through Coulombic interactions to form a bilayer (BL).<sup>32</sup> As this process is repeated, the result is the formation of a multilayered polyelectrolyte composite film.

The incorporation of inorganic additives can produce LbL films with unrivaled barrier properties, however, these coatings are very brittle and not suited for applications requiring biocompatibility or stretchability.<sup>227</sup> All-polymer polyelectrolyte films can be fabricated from synthetic polymers such as branched polyethyleneimine and polyacrylic acid that have excellent oxygen barriers due to the dense, electrostatically-bound complexation that reduces the free volume within the coatings and limits oxygen diffusion.<sup>77,228</sup> Multilayered films constructed by hydrogen bonds are more capable of stretching than those assembled by ionic interactions due to the H-bond ability to more readily break and reform compared to ionic interactions.<sup>71,229,230</sup>

Chitosan (CS) is a polysaccharide that is produced from the deacetylation of chitin, which is a primary component of crustaceous shells. CS has been used extensively in biomedical and food science applications due to the primary amine functionality resulting from the deacetylation of the glucosamine groups on the polymer backbone.<sup>82,83,231</sup> Another ionic, biologically-derived polysaccharide is alginate (Alg), which is extracted from brown algae.<sup>225,232,233</sup> Because of the opposite charges located on the saccharide backbones of each of these polymers, the pair is suitable for polyelectrolyte LbL film deposition and has found applications such as edible polyelectrolyte multilayer coatings and even free-standing membranes, however, the application of these polymers as a polyelectrolyte oxygen barrier has not been reported.<sup>86,88,89,234–236</sup>

The Henderson-Hasselbalch equation describes the pH behavior of solutions of weak acids and bases dependent on the  $pK_a$  of the acid or base. This equation can be modified to calculate the total charge ( $C_p$ ) for a chain of  $i$  charged monomers with  $n_{iA}$  anionic functionalities of  $pK_{iA}$  and  $n_{iB}$  basic of  $pK_{iB}$  such as proteins and polyelectrolytes dependent on the number and  $pK_a$  values of the ionic functionalities present on the polymer (Equation 5.1).<sup>237</sup>

$$C_p = -\sum_{iA} n_{iA} (1 + 10^{-(pH-pK_{iA})})^{-1} + n_{iB} (1 + 10^{(pH-pK_{iB})})^{-1} \quad (5.1)$$

The percent charge of an average polyelectrolyte molecule and the change in percent charge of that molecule between two pH values can then be determined by Equations 5.2 and 5.3, respectively.

$$\%Charge = \frac{C_p}{C_{pMAX}} \quad (5.2)$$

$$\Delta\%Charge = \%Charge_{pH_{final}} - \%Charge_{pH_{initial}} \quad (5.3)$$

Herein, we first present a model of polyelectrolyte film deposition that emphasizes the pH-responsive activity of both polyelectrolytes and the role of each solution pH in interacting with the adsorbed polymers. We then utilize this model to show that the rate of growth of CS-Alg

polyelectrolyte multilayer films is highly sensitive to their pH and through calculation of the charge states of the polymers, the growth rate of the films is highly controllable and closely follows the change in percent charge of each polymer when dipped in the solution of oppositely charged polyelectrolyte. We also show that the rate of film growth can be further increased by simply heating the deposition solutions to decrease the need to deposit multitude of layers. Furthermore, we show that these films are very stiff, yet are also capable of 10% strain before the coatings begin to wrinkle or crack. Finally, we show that these coatings have outstanding oxygen barrier properties at low relative humidity that exceed any edible coatings that have been reported earlier.<sup>238</sup>

## 5.2 Materials and Methods

### 5.2.1 Materials

Chitosan (CS, low molecular weight (50,000 – 190,000 Da), 75 – 85% deacetylated, Sigma-Aldrich) was used as the polycation. Alginic acid from sodium salt (Alg, Sigma) was used as the polyanion. The chitosan was dissolved in 1.0 vol.% acetic acid (Fisher) in deionized water (Millipore) at a concentration of 0.1 wt.% and stirred overnight to complete dissolution. Alginate solutions were prepared at a concentration of 0.2 wt.% in deionized water. The pH of the polymer solutions were adjusted by gently adding 1.0 M hydrochloric acid (Fisher Scientific) or 1.0 M sodium hydroxide (Alfa Aesar) until the desired pH was obtained.

### 5.2.2 Substrate preparation

Silicon wafers (P/B(100) 406-480um SSP TEST) were purchased from University Wafer (South Boston, MA) and used as deposition substrates for thin-film characterization. The wafers were prepared for film deposition by washing with 20 mL acetone, 20 mL of isopropyl alcohol, 50 mL of water, and dried with a stream of purified air. Polyethylene terephthalate (PET, 7 mil) sheets were used as the substrate to characterize the barrier properties of LbL films.

### 5.2.3 Layer-by-layer deposition

Prepared substrates were first dipped in the chitosan, thoroughly rinsed with deionized water, dried with purified air, and dipped into the alginate solution with variable dipping times. Increased deposition temperature was achieved by placing both solutions on a hot plate along with 1 cm stir bar and magnetically stirred at 100 rpm during deposition.

#### 5.2.4 Film characterization

The thickness of the films on Si-wafers was measured using an  $\alpha$ -SE spectroscopic ellipsometer (J.A. Woollam, Lincoln, NE). Atomic force microscopy was performed using an Asylum MFP-3D classic atomic force microscope (Asylum Research, Morrisville, NC). The oxygen barrier property was measured with Oxtran 1/50 (MOCON, Minneapolis, MN) in accordance with ASTM D-3985 at 23°C and variable relative humidity (RH). Water permeability values were obtained using a Permatran 1/50 (MOCON, Minneapolis, MN) in accordance with ASTM E398 with variable RH. The stretchability was examined by straining the LBL films deposited on PU rubber (McMaster-Carr 40A) by Instron 5943 universal testing machine (Instron, Norwood, MA). The nanoscale film morphology was visualized by a Scanning Electron Microscope (FE-SEM, FEI Varios 460L) after Pt sputter coating (~ 7 nm). Nanoindentation was performed using a Hysitron Ubi-1 Nanoindenter with 50  $\mu$ N indents. Water contact angles were obtained by goniometry (First Ten Angstroms) with 5  $\mu$ L droplets. Transmittance of the coatings was determined by depositing films on a glass slide and using a clean slide as the reference in a Jasco V550 spectrophotometer.

The oxygen permeability values of the LbL coatings (thickness =  $d_{LbL}$ ) ( $P_{LbL}$ ) on PET substrates (thickness of  $d_{PET}$ ) were determined from oxygen transmission rate using Equation 5.4 below, where  $P_{PET}$  and  $P_{Total}$  are the oxygen permeability values of the PET substrate and the total laminate material, respectively and  $\Phi_{LbL}$  and  $\Phi_{PET}$  equal  $d_{LbL}/d_{Total}$  and  $d_{PET}/d_{Total}$ , respectively.<sup>239</sup> Water vapor permeabilities for the LbL films were also calculated by Equation 5.5.<sup>240</sup>

$$P_{LbL} = \frac{P_{Total}\Phi_{LbL}}{1 - \frac{P_{Total}\Phi_{PET}}{P_{PET}}} \quad (5.4)$$

$$WVP_{LbL} = \frac{d_{LbL}}{\left(\frac{d_{Total}}{WVP_{Total}}\right) - \left(\frac{d_{PET}}{WVP_{PET}}\right)} \quad (5.5)$$

## 5.3 Results

### 5.3.1 Charge cycle of polyelectrolyte layer-by-layer films

The pH of polyelectrolyte solutions is the primary system parameter governing the film growth of polyelectrolyte LbL films.<sup>75</sup> Here, we introduce a simple model that correlates the charge behavior of polyelectrolytes at different pH values to the growth behavior of PEMs. By using the  $pK_a$  values of the charged functional groups on both polyelectrolytes, it is possible to predict trends in the growth of the resulting PEM. The key insight that this model imparts is the dynamic change in charge and subsequent change in conformation of polymer chains that are already adsorbed onto the substrate acting as grafted polymers. Generally, polycation chains will become more charged when exposed to a lower pH and conversely, polyanion chains will become more charged when their environmental pH is increased.

When a substrate is first dipped into a polycationic solution, the polymer adsorbs to the substrate in its pH-governed conformation. Following rinsing and drying, the substrate is then dipped into the polyanionic solution, where two phenomena occur simultaneously. The adsorbed polycationic molecules comprising the outer layer of the coating will begin to react to the conditions of the anionic solution while the polyanionic molecules interact and bind to those polycationic chains at their respective charge states and conformations to form the first bilayer (BL). If the pH of the polyanionic solution is less than that of the polycation (Figure 5.1a-b), the previously adsorbed polycationic molecules will see an increase in the number of positive charges on the chain and reach a linear conformation resulting from electrostatic repulsion. The introduction of these new charges on the previously adsorbed polyelectrolyte chain introduces new active sites and facilitates further complexation with the opposing polyelectrolyte. Following rinsing and drying, the substrate is exposed to the higher pH polycationic solution, at which point

the outermost polyanionic layer will see the introduction of new charges of that polymer as the polyanion equilibrates to the higher pH of the polycationic solution. This introduction of new charges on the previously adsorbed layer drives exponential growth of these films until the limits of inter-layer diffusion have been reached and the film will grow in a quasi-linear profile. If the pH at which the polyanion is introduced is the same as that of the polycation (Figure 5.1c), neither polymer undergoes any change in charge in the other polyelectrolyte solution and the film growth is highly linear. If the pH of the polyanionic solution is higher than that of the polycation (Figure 5.1d), the previously adsorbed polycation molecules will see charge decrease when dipped in the polyanion solution and the resulting growth will be linear and slower than the same-pH system.

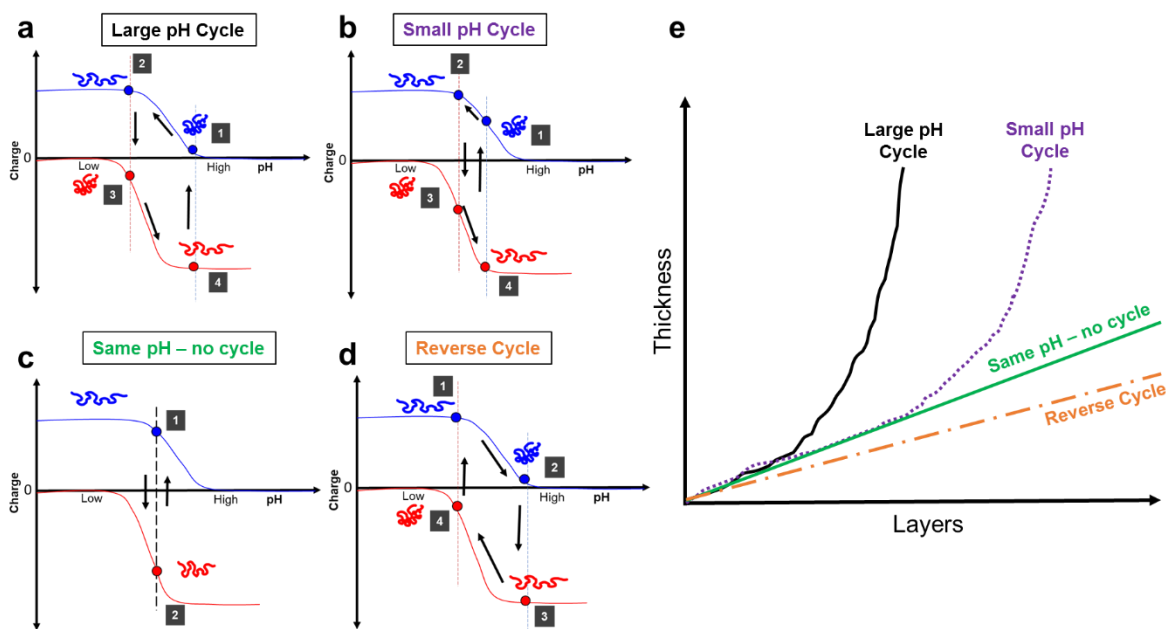


**Figure 5.1.** Schematics of the charge cycle driving polyelectrolyte film growth for polyelectrolytes. (a) Large forward pH cycle ( $\text{pH}_{\text{cation}} \gg \text{pH}_{\text{anion}}$ ), (b) small forward pH cycle ( $\text{pH}_{\text{cation}} > \text{pH}_{\text{anion}}$ ), (c) same pH ( $\text{pH}_{\text{cation}} = \text{pH}_{\text{anion}}$ ) and (d) reverse cycle ( $\text{pH}_{\text{cation}} < \text{pH}_{\text{anion}}$ ) depending on the relative pH values of the polycation and polyanion solution. (e) Expected film growth trend for these different schemes.

### 5.3.2 Charge cycle analysis of chitosan and alginate biopolyelectrolytes

The structures of the chitosan (CS) and alginate (Alg) are shown in Figure 5.2a and their  $pK_a$  values were estimated to be 6.5 and 3.2, respectively<sup>90,232</sup>. Using Equation 5.1, the average charge per molecule of the CS and Alg solutions over the entire pH range was calculated (Figure 5.2b). To qualitatively investigate the conformational behavior of the polyelectrolytes at varying pH, dynamic light scattering (DLS) measurements were performed over a range of pHs and the derived count rates of the solutions were recorded (Fig 5.2c). At higher pH values at which Alg is more charged, the derived count rate of the solution reaches a minimum due to the molecular nature of the ionically charged Alg solution. Similarly, at low pH values where CS is highly charged, the CS solution also reaches a minimum and levels off.

In their highly charged states, both CS and Alg assume highly linear conformations corresponding with the low derived count rate values obtained by DLS. As the polyelectrolytes lose charge, the derived count rate of both solutions increased, indicating more coiled polymer conformations that effectively scatter more light. Alg solutions below a pH value of 4 formed aggregates (Figure 2c). To mitigate any technical challenges, Alg solutions were maintained at a pH of 4 or greater despite the faster film growth seen at lower pH values. Similarly, CS solutions adjusted to pH above 6.5 exhibited instability and precipitated from solution, necessitating all CS solutions to be maintained at or below pH 6. These two constraints present a pH window between values of 4 and 6, where both polyelectrolytes are stable in solution. Finally, Equation 5.3 was used to calculate the average percent charge of the bulk CS and Alg solutions over the operational pH range (Fig 5.2d).

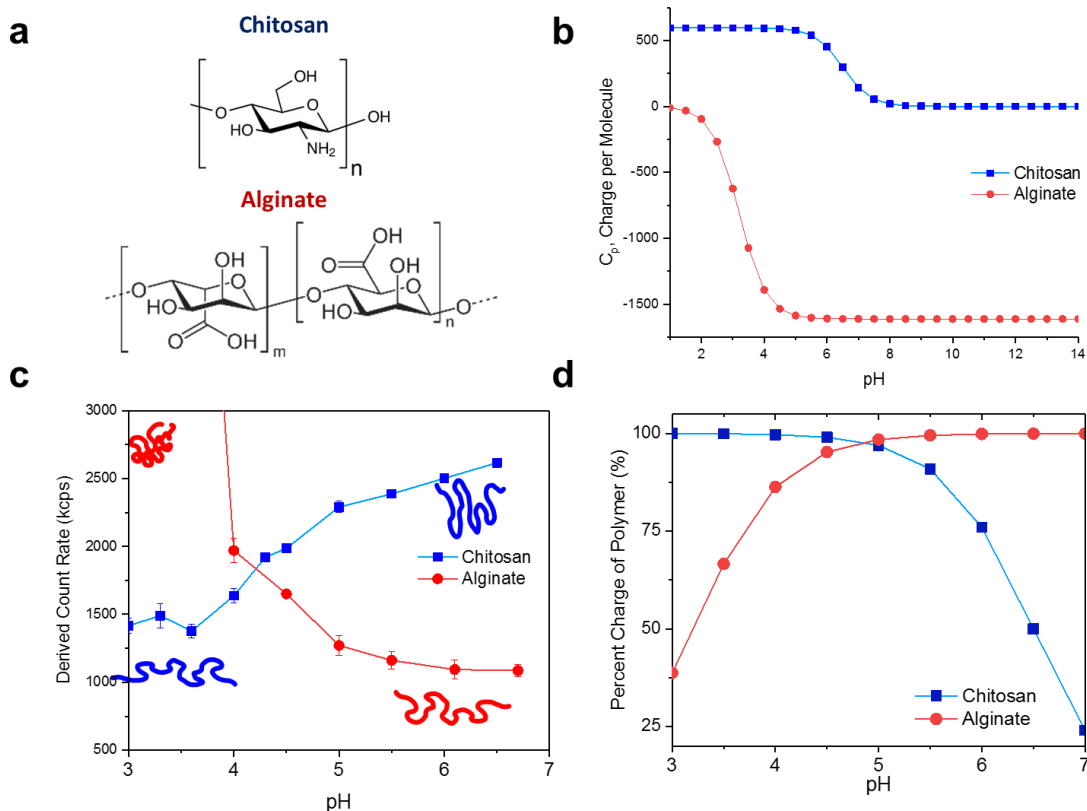


**Figure 5.2.** Charge and conformation of chitosan and alginate. (a) Molecular structures of chitosan and alginate biopolyelectrolytes; (b) calculated charge of average polyelectrolyte molecules of chitosan alginate vs. pH; (c) percent charge and average molecule charge of CS and Alg in the pH range of interest (alginate %charge normalized to negative value) and (d) derived count rates of CS and Alg solutions vs. pH obtained using dynamic light scattering.

To illustrate this charge cycle and its application in CS-Alg PEM systems, a forward cycle of CS<sub>6</sub> – Alg<sub>4</sub> and a “reverse” cycle of CS<sub>4</sub> – Alg<sub>6</sub> are shown in Figure D1 along with schematics for all possible growth regimes. CS-Alg PEM growth was analyzed by maintaining one polyelectrolyte solution and systematically changing the pH of the oppositely charged polymer by first holding the CS solution at pH 6 with varying Alg pH (Figure 5.3a-b) followed by maintaining the Alg solution at pH 4 and systematically varying the CS pH (Fig 5.3c-d). The growth trends for all films deposited at room temperature are linear, indicating low interlayer diffusion of the polyelectrolytes.<sup>241</sup> Both sets of experiments illustrate that the systems in which the pH<sub>CS</sub> is greater

than  $\text{pH}_{\text{Alg}}$  show faster film growth and that as the pH distance between the two polyelectrolyte solutions increases (larger forward charge cycles, Figure D1), as does the average BL thickness. In both sets of experiments, the reverse charge cycles (where  $\text{pH}_{\text{Alg}} > \text{pH}_{\text{CS}}$ ) show the slowest growth. The total  $\Delta\% \text{Charge}$  ( $\Delta\% \text{Charge}_{\text{Alg}} + \Delta\% \text{Charge}_{\text{CS}}$ ) was plotted against the average BL thickness for room temperature growth data obtained and a strong correlation is seen regardless of the specific pH values, further proving that the charge cycle is the dominant phenomenon driving the growth of these films (Figure 5.4).

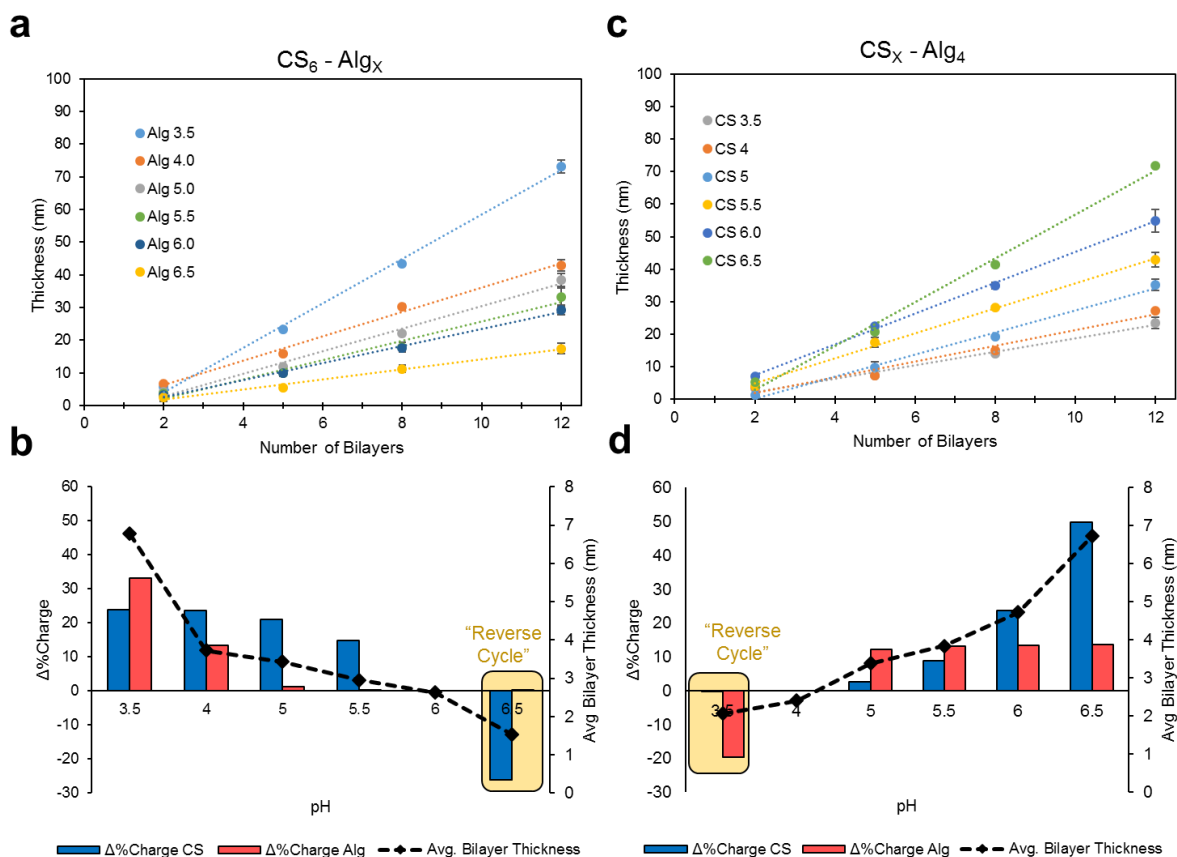


**Figure 5.3.** Polyelectrolyte multilayer growth of CS-Alg films. (a) Film growth profiles at 2, 5, 8, and 12BL and (b) average BL thickness (dashed line) and  $\Delta\% \text{Charge}$  (bars) for each CS<sub>6</sub> – Alg<sub>x</sub> LbL system. (c) Film growth profiles at 2, 5, 8, and 12BL and (d) average BL thickness (dashed line) and  $\Delta\% \text{Charge}$  (bars) for each CS<sub>x</sub> – Alg<sub>4</sub> LbL system. All data obtained at RT with 45 second dips.

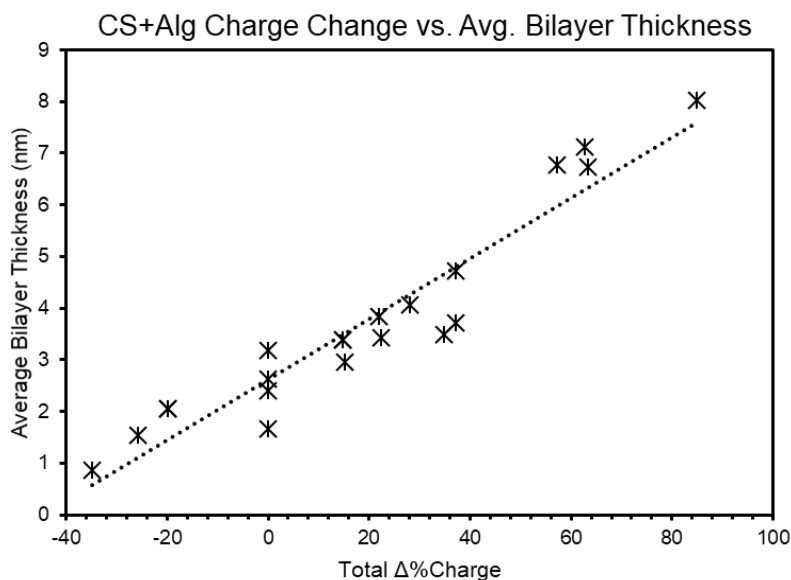


**Figure 5.4.** Average bilayer thickness vs. total  $\Delta\%Charge$  ( $\Delta\%Charge_{CS} + \Delta\%Charge_{Alg}$ ) for CS-Alg films of different pH systems at room temperature with 45 second dips.

For same-pH systems, there is no charge cycle for either polyelectrolyte and the resulting growth profiles are highly linear. For these systems, conformational effects dominate the resulting film thickness instead of charge, as the slowest film growth was seen for CS<sub>5</sub> – Alg<sub>5</sub>, the pH at which both polymers are nearly fully charged and adopt highly linear conformations. For same pH systems where either polymer is less charged, film growth increased, suggesting that the polymer chains at lower charge states are more coiled in their molecular conformation. The adsorption of these molecules leads to a thicker average layer (Figure D2).

While the trends in the growth rate of the CS-Alg systems are highly dependent on the change in charge of each polyelectrolyte when dipped in the opposing polyelectrolyte system, the relative rate of growth for this particular polyelectrolyte system at these conditions is slow when compared to similar LbL systems. The formation of a moderately thick ( $\sim 1 \mu\text{m}$ ) PEM is estimated to require over 200 bilayers for even the fastest growing system with the largest charge cycle (CS<sub>6</sub> – SA<sub>4</sub>). Because of the manufacturing burden that accumulating hundreds of bilayers for a single

coating requires, we began varying environmental conditions of the polyelectrolyte solutions to optimize the film growth rate. Both altering the molecular weight of the CS and adding of NaCl to the polyelectrolyte solutions at various concentrations did not accelerate CS-Alg PEM growth (Figure D3) and were not further investigated as a route to hasten film growth.

### 5.3.3 Effect of temperature and exposure time on CS-Alg PEM growth

The modulation of solution temperature resulted in a drastic change in the growth rate of the film. Previous studies have hypothesized that an increase in solution temperature increases the level in inter-layer diffusion of the polyelectrolytes due to swelling of the film by water at increased temperature (Figure 5.5a) and this effect accounts for the increased growth rate with temperature.<sup>241,242</sup> Changing the solutions conditions from room temperature (RT, 22°C) to 45°C only resulted in a marginally thicker film after 12 bilayers, but further increases to 60°C and 75°C resulted in significant increases in growth rate. The films prepared in polyelectrolyte solutions at 75°C reached a thicknesses over 500 nm in just 12 BL. This thickness is over 3× higher than the one of the corresponding 60°C sample and about 10× higher than the thickness of the same CS-Alg PEM produced at 20°C, which is shown in Figure 5.5b. Next, CS<sub>6</sub> –Alg<sub>4,5,6</sub> films were prepared at RT and 60°C to confirm that that charge cycle still dominates film growth and that an increase in temperature does amplify the growth rate of the film, but the relative growth rates at each temperature are still dependent on the charge cycle behavior of the polyelectrolytes. As seen from the plots in Figure 5.4c, at RT (dashed lines) each system shows slow growth with decreasing Alg solution pH, yielding higher growth rates. An increase in the solution deposition temperature of each system to 60°C significantly increases the growth rate of each CS – Alg system, however, the charge cycle-dependent growth trends observed at RT are still present at 60°C.

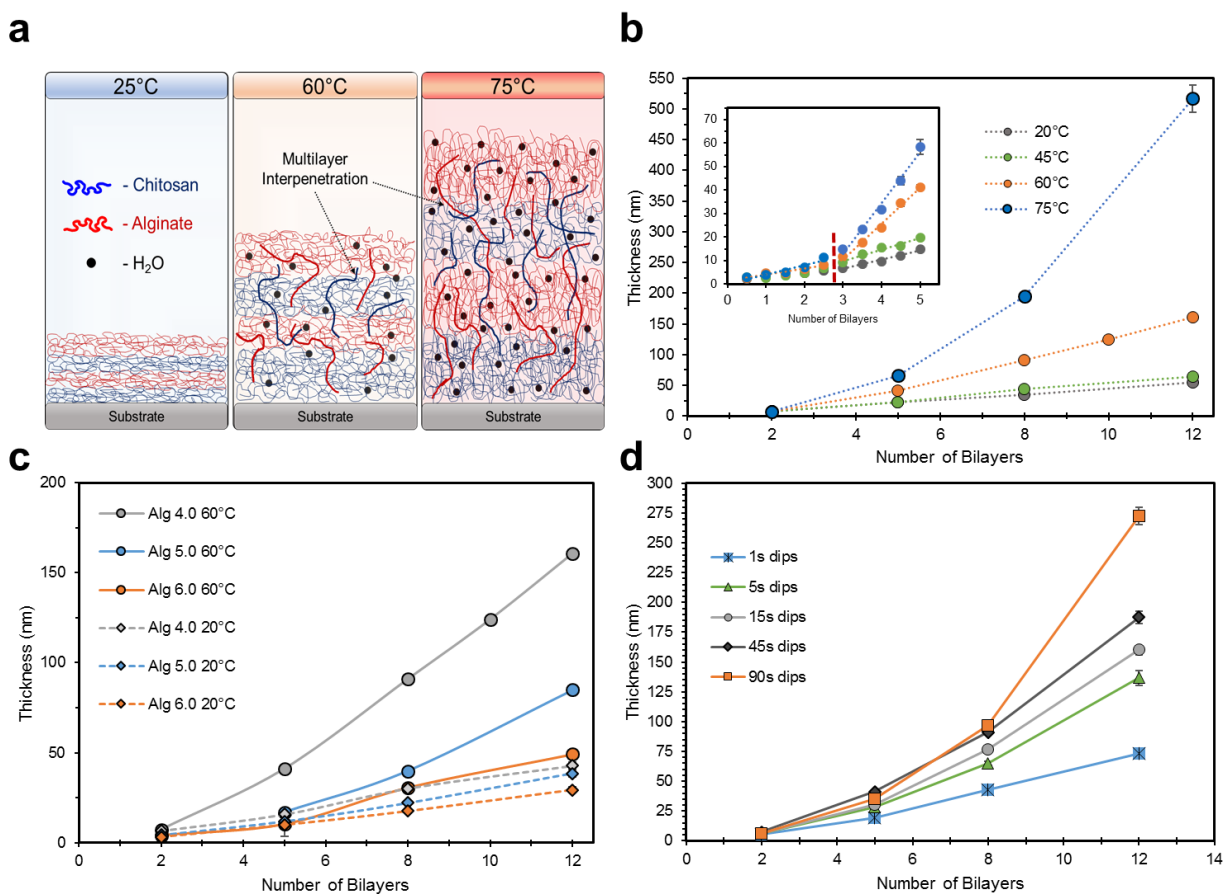


**Figure 5.5.** Effect of the environmental parameters - temperature, pH, and dipping time on CS-Alg polyelectrolyte multilayer growth. (a) Schematic illustrating the swelling of the multilayer film by H<sub>2</sub>O at increased temperature leading to increased polyelectrolyte interlayer penetration and growth; (b) Film thickness vs. bilayer number for CS<sub>6</sub> – Alg<sub>4</sub> systems prepared at various solution temperatures with inset graph showing thickness for each layer of the first 5 bilayers; (c) Film thickness vs. bilayer number for CS<sub>6</sub> – Alg<sub>X</sub> (X = 4,5,6) with RT solutions (dashed) and 60°C solutions (d) Film thickness vs. bilayer number for CS<sub>6</sub> – Alg<sub>4</sub> films prepared at 60°C with varying dipping time.

Films prepared using the CS<sub>6</sub> – Alg<sub>4</sub> system at 60°C with varied dipping times saw a strong dependence of growth on the dipping time shown in Figure 5.5d. A clear trend also presents itself indicating linearity in the growth profiles of films with shorter dip times. As the deposition time increases, the growth trends of these films shift into exponential profiles. This suggests that the primary adsorption step involving simple electrostatics between the oppositely charged polyelectrolytes happens very rapidly, while the interactions that give rise to the more exponential

growth, namely interlayer diffusion due to swelling of the multilayer with temperature (Figure 5.5a), are slower and require more time to reach equilibrated state. It has been suggested that films where exponential growth of the PEM occurs incorporate more water into the swollen film and result in softer films with higher permeability values.<sup>243</sup> We performed nanoindentation to compare the reduced moduli of CS-Alg PEMs prepared using a forward pH charge cycle and a same-pH pair with no charge cycling. The CS-Alg film prepared with an inherent charge cycle system exhibited lower reduced moduli compared to these of the same-pH CS<sub>4</sub>-Alg<sub>4</sub> film, suggesting that the charge cycle films may have more retained internal water content and lower moduli (Figure D4). Nevertheless, with just a 5 second dipping time, the thickness of the film after 12 bilayers was 75% of the thickness of the sample obtained with 45 second dips, indicating that reduction of exposure time of the substrate with the sample can vastly reduce the total time of production without significantly reducing the thickness of the resulting film.

#### 5.3.4 Surface characterization of CS-Alg PEM films

The choice in pH of both the CS and Alg solutions govern not only the rate of multilayer growth, but also the surface properties of the resulting film. Specifically, the conformation of the polyelectrolyte during their adsorption process determines the surface roughness of the resulting dried film. As shown in Figure 5.6a, the surfaces of the CS-Alg multilayers in which the CS solution was maintained at pH 6 show higher roughness with decreasing Alg pH. This trend is confirmed by analyzing the root-mean-squared (RMS) roughness values of consecutive layers of these systems that only differ by the pH of the Alg solution. These layers (13 – 16) were chosen for analysis to ensure that film growth had progressed beyond the nucleation and growth phase. In Figure 5.6b, it is shown quantitatively that the roughness of the CS<sub>6</sub> – Alg<sub>x</sub> films increases with decreasing alginate pH, supporting the idea that at lower solution pH values, the Alg chains adopt

and adsorb in a more compactly coiled conformation, yielding higher surface roughness (Figure D5). Interestingly, the roughness values of the films do not show high variance between the alternating CS and Alg layers, but instead the roughness trend is maintained with each adsorbed layer.

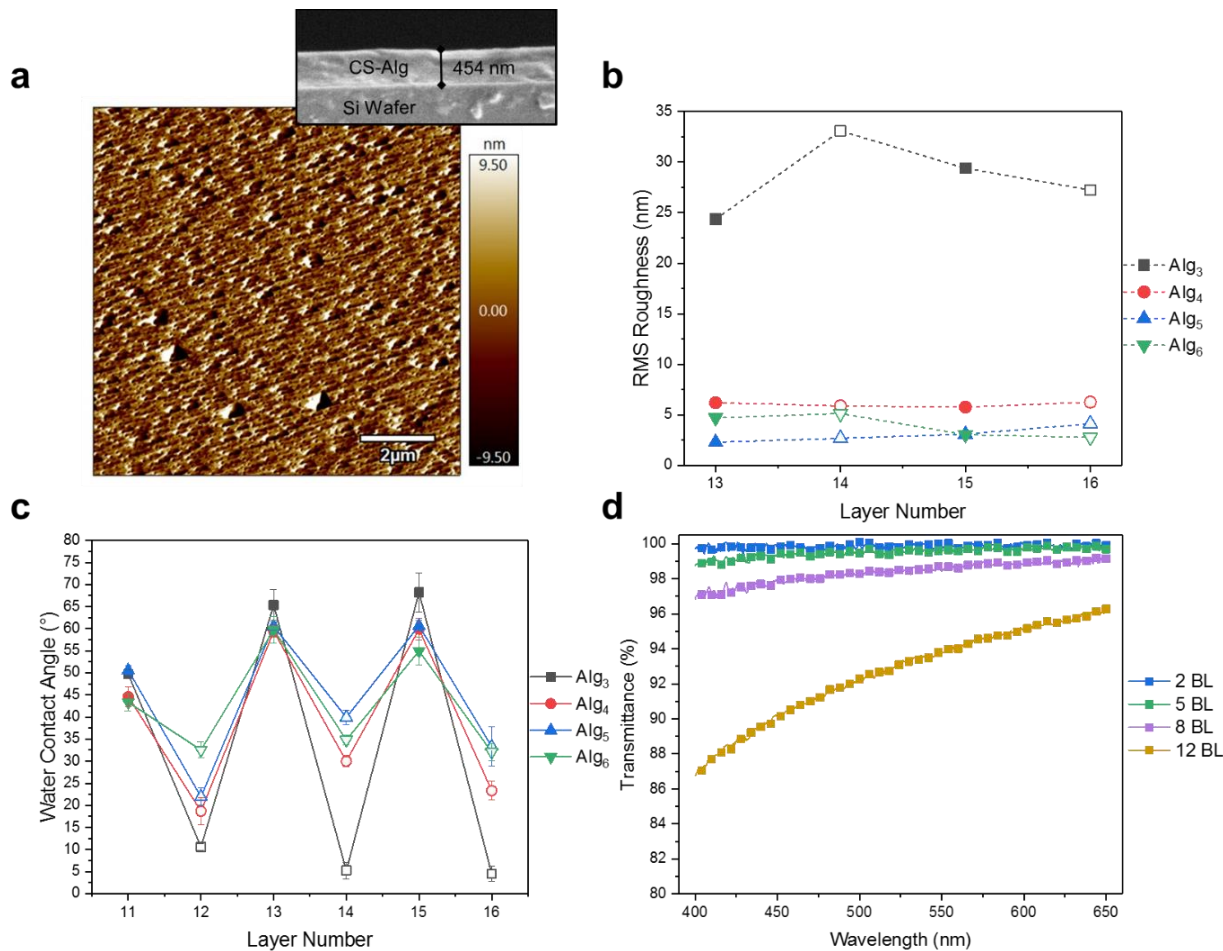


**Figure 5.6.** Physical properties of CS – Alg PEM coatings. (a) AFM image of a CS<sub>6</sub> – Alg<sub>4</sub> (60°C,45s dip time) film surface with an inset SEM image of a CS<sub>6</sub> – Alg<sub>4</sub> cross-sectional PEM. (b) Root mean squared roughness and (c) water contact angle of CS<sub>6</sub> – Alg<sub>3,4,5,6</sub> films (60°C, 45s dips) for alternating, complete layers of CS (filled) and Alg (unfilled). (d) Transmittance of CS<sub>6</sub> – Alg<sub>4</sub> films of varying thickness over the visible light spectrum (400 – 650 nm).

The affinities of each layer of these films to water were then analyzed by measuring the water contact angle (WCA) on every layer of each system (Figure 5.6c). For all systems, the CS

layers exhibit more hydrophobicity than the Alg layers as expected. Furthermore, the larger the difference in pH between the CS and Alg solutions during film deposition (largest charge cycle), the greater the swing in WCA between each consecutive layer, with the CS layers exhibiting higher WCA and the Alg layers showing very hydrophilic behavior. The differences in WCA between films of the same layer number and the amplification of the hydrophobic/hydrophilic behavior of the film depending on the deposition pH of the Alg solution is affected by the surface roughness of the films, with rougher films showing higher WCA for CS layers, but lower WCA for Alg layers. However, the charge state of the polyelectrolytes upon their adsorption also playing a role, as less charged, coiled polyelectrolytes may readily engage in hydrogen bonding with water than their highly charged counterparts thus lowering the WCA.

Finally, the optical transmittance of a CS<sub>6</sub> – Alg<sub>4</sub> film was analyzed against the number of increasing bilayers, and it was found that after 12 BL (~200 nm thickness) assembled on a glass slide, the film showed >90% transmittance over the range of visible light compared to the clean glass control (Figure 5.6d). To determine the behavior of the coating under strain, an elastic polyurethane sheet was coated using the CS<sub>6</sub> – Alg<sub>4</sub> system at 60°C and it was determined using scanning electron microscopy that the film did not show cracking following 10% strain, however, after 20% strain, cracks appeared in the film (Figure D6).

### 5.3.5 Barrier characteristics analysis of CS-Alg PEM films

The CS-Alg PEM shows unprecedented efficacy as barrier coatings that are composed only of biopolymers. To analyze the oxygen and water vapor barrier properties of the CS-Alg films, 30 BL (60°C, 45s dips, ~450 nm thickness) were constructed on PET. Their oxygen transmission rate (OTR) values were recorded at varying relative humidity (RH) (Figure 5.7a) and the water vapor transmission rate (WVTR) (Figure 5.7b) values were obtained at 90% RH. At low RH, The CS-

Alg PEM drastically reduced the OTR of the composite to a value below  $1 \text{ cm}^3\text{m}^{-2}\text{day}^{-1}\text{atm}^{-1}$  compared to an OTR value above 20 for the uncoated sample. However, increasing RH values induces swelling of the film by  $\text{H}_2\text{O}$ , increases the free volume of the composite, and increases the permeation of oxygen through the film. Nevertheless, at 50% RH, a strong oxygen barrier resilience is still present with the OTR of the composite film increasing to 10. At a 90% RH, the film no longer acts as a strong oxygen barrier and the OTR of the composite is similar to that of the uncoated PET substrate. The oxygen and water vapor permeability values of the LbL multilayers were decoupled from those of the PET substrate as previously described and a comparison of these values to other edible, biomaterial-based coatings is shown in Table 5.1 and Table 5.2.

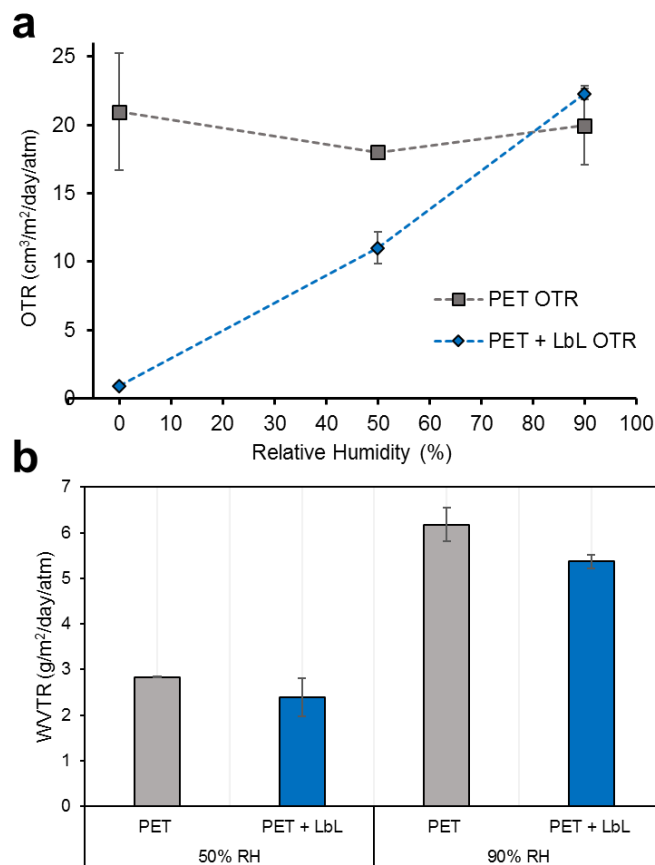


**Figure 5.7.** Barrier properties of  $\text{CS}_6 - \text{Alg}_4$  LbL coatings. (a) Oxygen transmission rate and (b) water vapor transmission rates of pure PET and 30 BL  $\text{CS}_6 - \text{Alg}_4$  LbL-coated PET.

**Table 5.1.** Oxygen barrier properties and comparison of biopolymer coatings at 0% RH.

<b>0% RH</b>	<b>(<math>10^{-16} \text{ cm}^3 \text{ cm} / (\text{cm}^2 \text{ s Pa})</math>)</b>		
<b>Sample</b>	<b>Permeability of Coating</b>	<b>Comparison</b>	<b>Reference</b>
PET 0% RH	42.6	8463	-
LbL 0% RH	0.00503	1	-
BPEI/PAA	0.00032	0.064	77
CS/CNCs	1.944	386	244
Soy Protein Isolate	199	39554	245
HPC/PEG	179	35607	246
Chitosan	0.137	27.2	247
Amylose	0.1157	23.0	248

**Table 5.2.** Oxygen barrier properties and comparison of biopolymer coatings at 50% RH.

<b>50% RH</b>	<b>(<math>10^{-16} \text{ cm}^3 \text{ cm} / (\text{cm}^2 \text{ s Pa})</math>)</b>		
<b>Sample</b>	<b>Permeability of Coating</b>	<b>Comparison</b>	<b>Reference</b>
PET 50% RH	36.6	7268	-
LbL 50% RH	0.125	24.9	-
Corn Zein/Soy Protein	81.0	16099	249

To visualize the effect that an edible oxygen barrier using this LbL composition can have on the aging of fruit, a bundle of Dole® Organic bananas was purchased and half were given a CS<sub>6</sub>—Alg<sub>4</sub> 25.5 BL coating (60°C, 5s dips) and stored adjacent to each other at 22°C, 50% RH. Juxtaposed pictures of representative coated and uncoated bananas are shown in Figure 5.8.

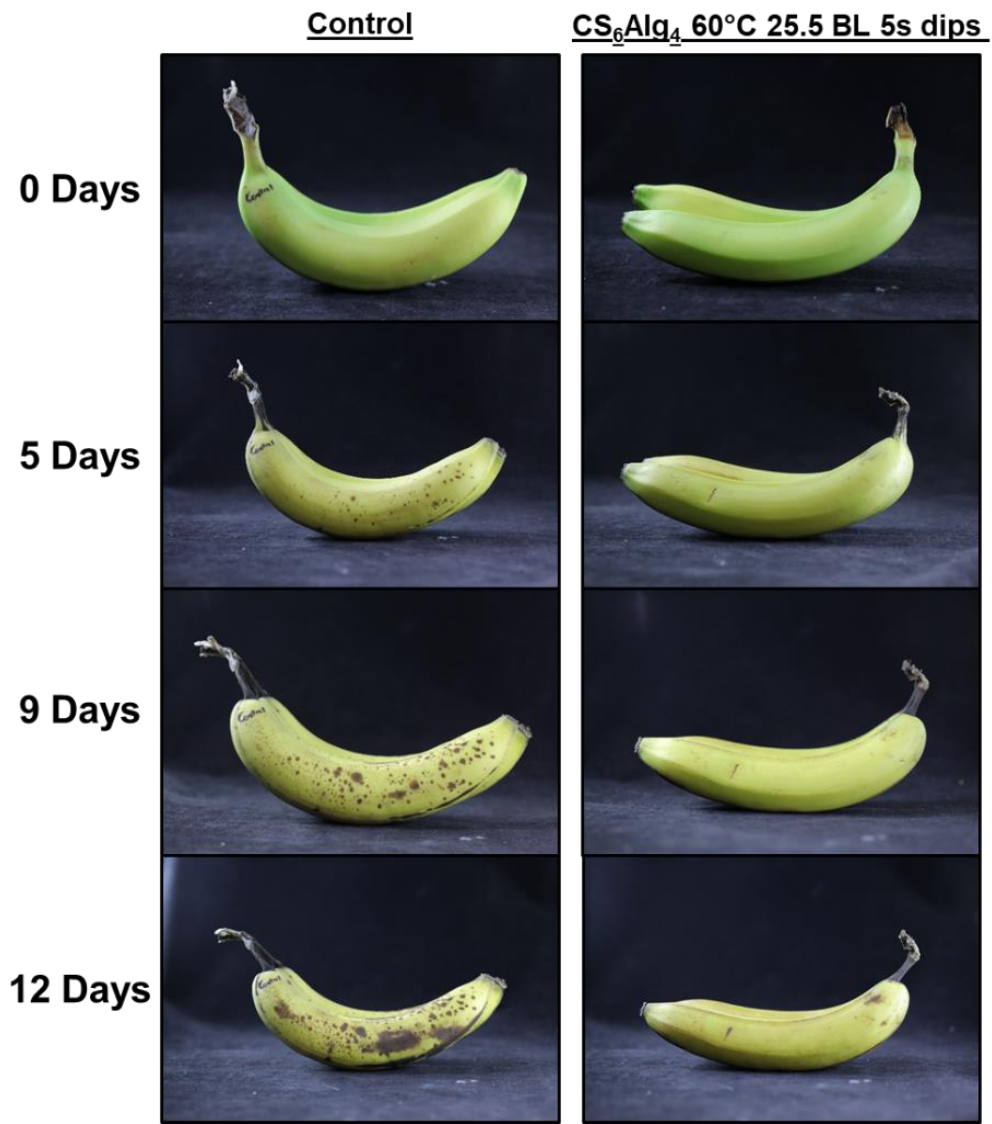


**Figure 5.8.** Pictures of an untreated (left, control) bananas and bananas coated with 25.5 BL of CS<sub>6</sub> – Alg<sub>4</sub> at 60°C (~280 nm thickness) with a 5 second dip time.

## 5.4 Conclusions

The charge profiles of polyelectrolytes govern the conformation of the polymer chains.<sup>89</sup> As the net charge of the molecules increases, the ionic groups on the backbones of both CS and Alg exhibit electrostatic repulsion which gives the total molecule a linear conformation. As the polymer molecules become less charged, the nonionic groups within the chains could also engage in intrachain hydrogen bonding resulting in a more coiled chain conformation.<sup>250</sup> Here, we show that PEM growth is driven by the change in charge of the previously adsorbed polyelectrolyte layer as it “reacts” to the pH of the other polyelectrolyte solution and helps to account for the exponential growth profiles seen by many polyelectrolyte systems with forward charge cycles (Figure 5.1). By adjusting the pH of the polyelectrolyte solutions to the same pH, neither polymer undergoes a change in charge state upon immersion into the opposite polyelectrolyte solution, resulting in a linear growth profile and a uniform BL thickness that is instead governed by the conformation of each polyelectrolyte at that pH (Figure D2).

Films prepared with a large pH cycle will be primarily composed of rigid electrostatic bonds between the interacting polymers due to the introduction of new charges that drive these films into the exponential growth regime. PEMs prepared with highly ionic architectures have found application as oxygen barrier coatings, however, these films are brittle, typically incapable of being stretched without cracking and thus unsuitable for packaging applications requiring strain or thermoforming.<sup>77,251</sup> As the difference in pH between the polycationic and polyanionic solution decreases, the magnitude of the charge introduced on a polyelectrolyte when exposed to the other polyelectrolyte solution will decrease until the pH of the two solution will be the same (Figure 5.2, Figure D2). While the charge cycle governs the growth rate, the surface properties (Figures E5, E6) of CS-Alg PEMs, the exposure time in each polyelectrolyte solution and temperature are

parameters that greatly affect the PEM growth rate with increases in either parameter leading to faster PEM growth. However, even at an elevated temperature of 60°C, the magnitude of the charge cycle ( $\text{pH}_{\text{CS}} - \text{pH}_{\text{Alg}}$ ) still governed the trend in the film growth rate (Figure 5.4).

CS-Alg PEMs have good mechanical properties with highly reduced moduli values, but are able to maintain some stretchability offered by the decreased charge densities of CS and Alg compared to synthetic polyelectrolytes, that allow hydrogen bonding to occur and facilitate elasticity of the coating architectures (Figs. E5, E7). The surface properties of these films including roughness and wettability are also highly dependent on the topmost layer of the coating (Figure 5.5, Figure D6). CS-Alg PEMs prepared at 60°C are very effective oxygen barriers, especially at low RH values. While the all-polymer CS-Alg PEM has an  $\text{O}_2$  permeability that is roughly 6% of that achieved by the branched polyethyleneimine – polyacrylic acid system at a RH of ~ 0%, this value is still over 20× lower than other comparable food-grade coatings (Figure 5.6, Tables 5.1, 5.2). At a more typical RH value of 50%, the PEM's ability to limit  $\text{O}_2$  diffusion was reduced because the ambient water caused swelling in the polymer coating, however, the CS-Alg PEM still reduced the total OTR through the PET to half of that of the plain PET sample (Figure 5.6).

Being prepared from biologically-derived, sustainably sourced, and food-grade polymers like CS and Alg enables the direct application of these PEMs to food products. To illustrate this, we coated two bunches of bananas that were originally from the same batch with 25.5 BL of the CS-Alg PEM and stored these two sets of bananas at the same conditions (RT, ~ 50% RH). As can be seen in Figure 5.7, the CS-Alg PEM-coated bananas saw a significant reduction in brown spots after two weeks of observation (Figure 5.7). These results highlight that by investigating the molecular architectures of PEMs, we can design food-grade and highly sustainable packaging materials and coatings that can prolong food viability and reduce waste.

## **CHAPTER 6: Summary and Future Work**

The overarching goal of my dissertation is to broaden the technical horizons of the shear-based polymer precipitation technique by both furthering the collective understanding of how tailored polymer nanomaterials can be produced using the technique and by exploring diverse applications for these materials. The utilization of polymer nanomaterials produced by techniques like electrospinning has increasingly gained interest academically, but often use techniques that are highly energy intensive and often lack commercial scalability and are limited to producing fiber morphologies. Herein, the principles underlying the formation of new classes of polymer soft materials - soft dendritic colloids (SDCs) and nanosheets (NSs) by the continuous and scalable turbulent shear-based nanomanufacturing technique are primarily explored.

In Chapter 1, several naturally occurring nanomaterials are presented followed by an overview of common techniques by which biomimetic polymer nanomaterials are produced to achieve similar material architectures and bulk properties. Applications of engineered nanomaterials are discussed along with the key material properties that enable their advanced functionalities like polymer chemistry, feature size, and pore structure. The new nanomanufacturing technique of shear-based polymer precipitation, which can produce nanofibers using a laminar nonsolvent flow, is introduced. The transition to a turbulent nonsolvent flow is then discussed along with the system parameters that govern the resulting particulate morphologies with a focus on the production of SDC and NS particles.

In Chapter 2, an expansion of the capabilities of the shear-based polymer precipitation technique including ionic hydrogel cross-linking and complexation of oppositely charged polyelectrolytes is presented. The addition of these precipitation mechanisms by which particles with the characteristics SDC and NS morphologies can be fabricated drastically increases the number of polymers that are compatible with this technique along with the collection of colloidal

particulates that can be produced. It is expected that SDCs can be produced by techniques that utilize other rapid precipitation mechanisms such as temperature-induced phase separation, UV photopolymerization, or interfacial polymerization.<sup>252</sup> Several researchers in Velev group continue to study the parameters that control the morphologies of the particles produced by shear-based polymer precipitation and are expanding applications of SDCs as packaging additives and as microplastic remediation materials. Biopolymer alginate – chitosan cSDCs readily form highly durable membranes as well as aerogels after being freeze-dried. These porous biomaterials are promising scaffolds for future cell culture, wound healing, and controlled-release materials (Figure 6.1).<sup>92,253</sup>

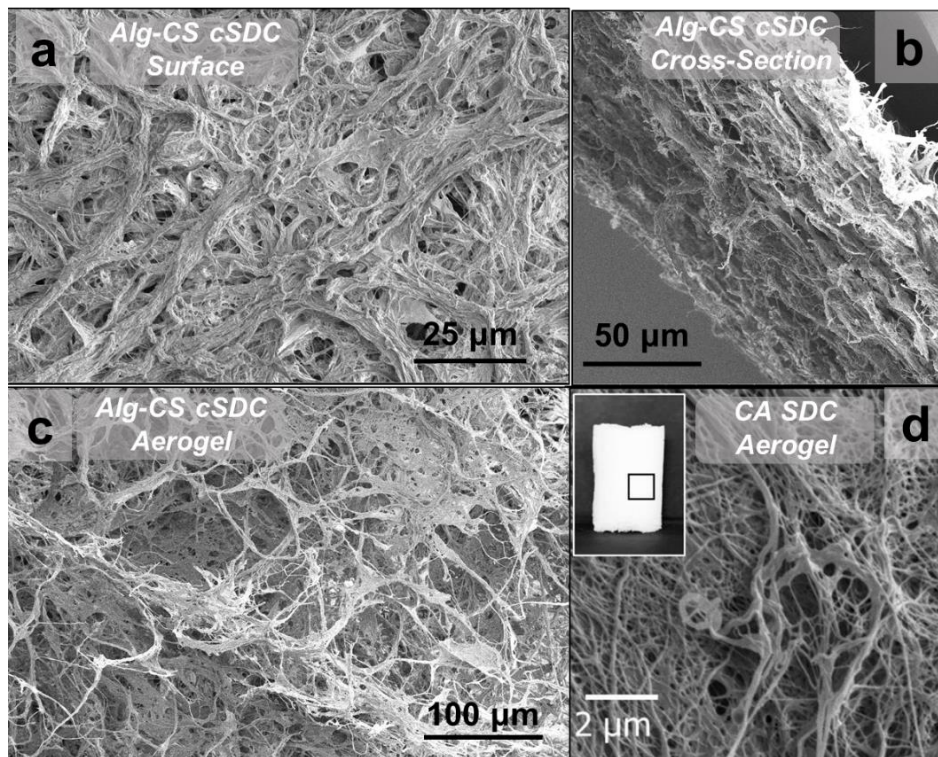


**Figure 6.1** Nanofibrous biopolymer membranes and aerogels made from soft dendricolloids. Scanning electron micrographs of (a) the surface and (b) a cross-section of an Alg-CS cSDC membrane and (c) and an Alg-CS cSDC aerogel prepared by freeze-drying a 1 wt.% cSDC suspension. (d) A cellulose acetate SDC aerogel prepared by freeze-drying a 1 wt.% SDC suspension in water.<sup>65</sup>

The development of a new class of homocomposite hydrogel materials is then described.<sup>120</sup> The hydrogel SDCs discussed in this chapter are prepared from alginate hydrogel, which is precipitated by rapid ionic cross-linking by calcium ions in an aqueous phase. The viscoelastic properties of SDC suspensions are investigated and compared to molecular alginate hydrogels at the same alginate concentrations. SDC suspensions can efficiently induce gel-like behavior resulting from the abundance of adhesive sub-contacts throughout the bulk suspension, similar to an effect previously described with hydrogel microfibers.<sup>45</sup> Additionally, we explore a homocomposite system in which alginate SDCs are dispersed in a molecular alginate matrix.

The colloidal SDC network has a synergistic stiffening effect on the molecular alginate network within the homocomposite hydrogel. The formation of colloidal-molecular network hydrogels results in a three-fold to five-fold higher elastic and complex moduli when analyzed by tensiometry and rheometry, respectively. These homocomposite formulations exhibit pronounced gel-like behavior with yield stresses from the SDC network even prior to cross-linking the molecular network.<sup>45</sup> The yield stress allows for the extrusion and 3D printing of these alginate-only formulations without necessitating a precipitation bath by allowing the extruded homocomposite formulation to maintain its shape while the secondary molecular network is forming.<sup>129</sup> This novel alginate hydrogel systems presented here can find applications in soft robotics, biomedical materials, and food products.<sup>137,149</sup> This chapter provides guidance for the preparation and applications of such homocomposite materials. Because SDCs can be produced from a large number of polymers including other biomaterials and hydrogel-forming polymers, this section highlights the efficiency with which the branched-nanofiber SDC morphology can uniquely impart the making of viscoelastic suspensions and mechanical enhancements to elastic hydrogel materials and will inform the future design of such soft materials moving.

In Chapter 3, the application of SDCs as porous membranes is investigated. Dry SDC membranes are prepared by filtering SDC suspensions. By investigating two very different applications necessitating porous polymer materials – bioscaffolds for lung cell models, and lithium ion battery separators – this chapter discusses the structure-property relationships between SDCs and their resulting membranes. These relationships are investigated using very soft biocompatible polyurethane (PU) polymer for bioscaffold applications and polyvinylidene fluoride (PVDF) for lithium ion battery separator materials. In the PU SDC system, the addition of just 20 vol.% glycerol to the nonsolvent increases the nonsolvent shear stress and produces PU SDCs with smaller features and more defined fibers. In the PVDF system, the particulate morphologies are controlled instead by varying the concentration of polymer in the injection solution with PVDF SDCs produced at low polymer concentrations with a transition to PVDF NSs at high concentrations.<sup>37</sup> While both the PU and PVDF SDC systems produce mechanically robust and highly porous (~ 70%) membranes, we show that the elastic modulus of PU SDC membranes can be controlled by the SDC morphologies, with smaller fibers yielding softer membranes (~ 200 kPa), while the PU SDCs with larger fibers produce stiffer membranes (~ 800 kPa). A similar trend is seen in the PVDF system, with the more fibrous PVDF SDCs membranes exhibiting decreased stiffness, tensile strength, and elongation compared to the membranes prepared from PVDF NSs.<sup>254</sup> Shear-based polymer precipitation emerges as a technique by which high performance nanofiber membranes with controlled features can be scalably and economically produced for many applications in which polymer nonwovens are currently utilized.<sup>20,255</sup>

Looking forward, the Velev group is interested in increasing the biomimicry of the PU SDC bioscaffolds by embedding magnetically-actuated and 3D printed meshes into the PU SDC membranes. By doing so, these SDC membranes will not only mimic physiological stiffness and

topography but will also allow the untethered actuation of the membrane during lung cell culture studies consistent with cyclic strain experienced in the respiratory system.<sup>256</sup> The Velev group also seeks to further the use of SDCs as basis for battery separator materials. Not only can the PVDF SDC separators presented here be optimized further with improved membrane structures or layered SDCs specifically for lithium-ion battery applications, but many other existing and emerging battery technologies require the use of a porous polymer separator and the principles discussed here can underlie their design.<sup>188,257</sup>

The application of SDCs in advanced coatings, with a specific emphasis on their wetting properties, is presented in Chapter 4. To systematically investigate the wetting properties of SDC coatings, three different polymers are used as model coating systems: polystyrene (PS), polyester (PES), and polyvinyl alcohol (PVOH). These polymers were chosen due to their varying affinities to water, with PVOH being highly hydrophilic, PS being hydrophobic, and PES having intermediate wetting properties. By comparing the contact angles of droplets on spin-coated thin films of these three polymers to the water contact angle on SDC surface coatings for the same three polymers, it is shown that the overlapping fiber surface topography inherent to SDC coatings amplifies the wetting properties depending on the polymer comprising the SDCs.<sup>191,206</sup> Because of this effect, the PS SDC coating exhibits superhydrophobicity with low tilt angle while the PVOH SDC coating has a  $\sim 0^\circ$  contact angle with the droplet actively spreading over its superhydrophilic surface. The surface energy of the polymer comprising the SDC coating not only governs its wetting behavior, but also dictates the porosity of the coating and the adhesion between the coating and the substrate.

The low surface energy of PS and the hierarchical topography of the PS SDC coating endows it superhydrophobicity. This property also results in weaker adhesion to the substrate and

less cohesive packing of the fibers within the bulk coating evidenced by a higher porosity (~ 90%), while the high surface energy PVOH SDC coating adheres strongly with lower porosity (~ 20%). The mechanical properties of membranes prepared by filtering suspensions of each polymer SDC are directly analyzed by tensile analysis and correlated to the coating properties.

The droplet freezing times and the strength of ice adhesion on SDC-coated aluminum substrates are then investigated to determine the potential of SDC coatings in anti-icing applications. The PS SDC coating is superhydrophobic, but its weak adhesion results in the tearing of the coating from the substrate prior to removal of the ice mold from the surface while PES SDC coatings show a moderate increase in ice adhesion strength and PVOH SDCs increase ice adhesion strength. In this way, the superhydrophobicity of pure SDC coatings show mutual exclusion with the coating's adhesion to the substrate and durability. To mitigate these technical challenges, two strategies are investigated to improve the SDC coating wetting and adhesion properties simultaneously: 1. Blending of SDCs from different polymers to form bicontinuous SDC networks, and 2. Adding a polydimethylsiloxane (PDMS) microdroplet binder. We show that both PS/PVOH bicontinuous SDC coatings and the PES/PDMS composites retain hydrophobicity and exhibit anti-icing properties.

One major advantage to using SDC coatings is that the chemical and topographical features are not limited to the surface of the coating. Therefore, mechanical abrasion of the SDC coating does not necessarily diminish its hydrophobic properties as the hierarchical fibers are present throughout its bulk.<sup>258</sup> Coupled with Chapter 3, Chapter 4 will aid in the design of future SDC coatings and porous membranes with targeted porosity, mechanical characteristics, and wetting properties. Many previously reported polymeric superhydrophobic coatings and lithium-ion battery separators incorporate inorganic TiO<sub>2</sub> and SiO<sub>2</sub> nanoparticles into the polymer matrix to

further optimize the surface roughness and increase the water contact angle or improve the thermal properties of the composite.<sup>21</sup> Incorporating nanoparticles within the SDC surface coatings could be another direction for future investigation, although the shear-driven polymer precipitation technique has already shown its compatibility with nanoparticle incorporation.<sup>62</sup> Preliminary experiments have already demonstrated the successful addition of magnetic iron oxide nanoparticles into SDC fibers to produce magnetically-responsive SDC suspensions and nonwovens, as illustrated in Figure 6.2.

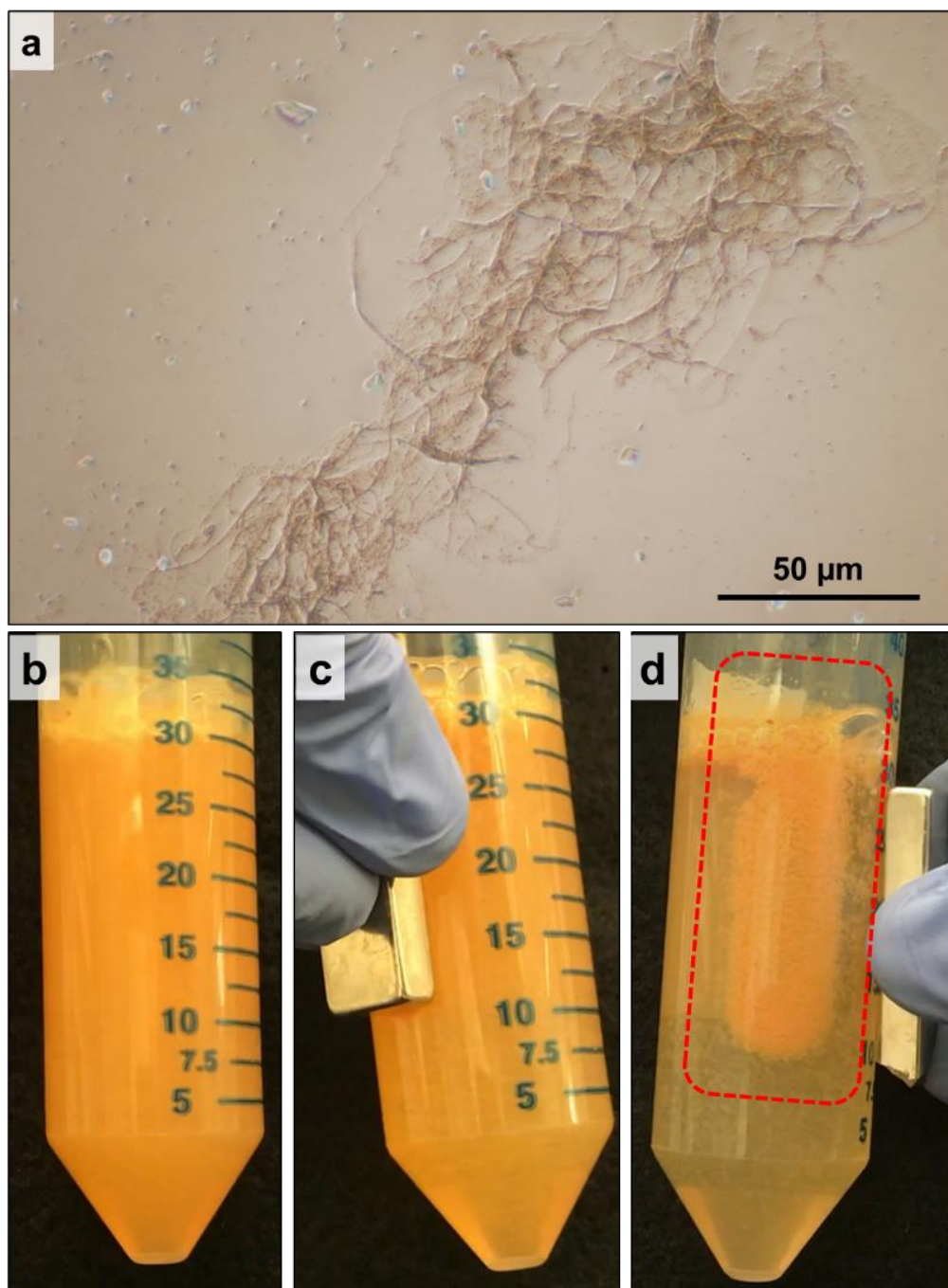


**Figure 6.2** Incorporation of magnetic iron oxide nanoparticles into cellulose acetate SDCs. (a) Phase contrast microscope image of a cellulose acetate SDC containing iron oxide nanoparticles embedded into its fibers. (b) A dispersed cellulose acetate/iron oxide composite SDC suspension in water followed by (c) application of a magnet to wall of the tube. (d) Efficient separation of the magnetic SDCs at the location of the applied magnet with noticeable loss in suspension turbidity.

This principle could be expanded further beyond magnetic applications to incorporate nanoparticles that improve nonwovens' thermal properties or catalytic particles that would benefit from the high surface areas offered by SDC materials. Additionally, there are current research projects in the Velev group seeking to produce SDCs either from a conductive polymer or to incorporate a conductive nanomaterial like graphene for use in composites for soft bioelectronics and sensors as well as nonwoven materials for superconductor applications.

Chapter 5 is also focused on special nanocoatings, where polyelectrolyte layer-by-layer (LbL) deposition technique is utilized to deposit polyelectrolyte multilayer (PEM) nanocoatings for oxygen barrier applications. Here, we show that the same complexation that allows the formation of polyelectrolyte composite SDCs can be utilized to develop composite nanocoatings with highly tuned roughness, wetting, and barrier properties. The idea of “charge cycling” in PEM systems is investigated by performing simple charge calculations derived from the Henderson-Hasselbalch equation between average polyelectrolyte chains at each solution pH. These calculations are shown to correlate very well to the growth rates in the chitosan – alginate (CS – Alg) system. While charge cycling governs the growth rate of the CS – Alg PEM, the relative growth rate of this system is low compared to PEMs of synthetic polyelectrolytes. By increasing the temperature of the polyelectrolyte solutions to 60°C, the growth rate of the PEM is significantly increased, because the increased temperature induces swelling of the PEM and allows for more interlayer diffusion of the polyelectrolyte chains, which has been shown to drive coating growth. Even at increased deposition temperatures, the degree of charge cycling that either polyelectrolyte undergoes continues to govern the relative growth rate.

The physical properties of CS – Alg coatings are then investigated, and it is shown that the surface roughness and water contact angle of the PEM are strongly dependent the conformation of

the polymer chains on the surface, with less charged and more coiled conformations of each polymer yielding higher surface roughness. The oxygen and water vapor permeabilities of CS – Alg coated polyethylene terephthalate sheets are analyzed and it is shown that they exhibit impressive barrier properties at low relative humidity values. While previously described synthetic PEMs studies have reported oxygen permeabilities 20× lower than the nanocoatings presented here, the CS-Alg PEMs show lower oxygen permeability than comparable biopolymer coatings found in the literature.<sup>77</sup> Even at an increase to 50% RH that causes swelling of the CS-Alg PEM and reduces the efficacy of the PEM,<sup>89</sup> a significant oxygen barrier resistance by the coating is still observed.<sup>223</sup> We further illustrate the benefits of using food-grade biopolyelectrolytes by coating bananas with the CS-Alg system, storing them for two weeks, and showing reduced browning in the coated bananas. This result indicates the potential for this type of biopolymer PEM coating to be directly applied to pharmaceutical and food products, thereby prolonging their shelf life, and diminishing the need for single-use polyolefin packaging materials.

The results overall present the big picture of how the design of new morphologies of colloidal polymer and biopolymer structures enable numerous advanced properties of functional soft materials. Cumulatively, the research presented within this dissertation serves as a toolkit to inform the design of colloidal polymer nanomaterials for use in coatings, membranes, suspensions, gels, and advanced composites.

## REFERENCES

1. Geim, A. K., Dubonos, S. V., Grigorieva, I. V., Novoselov, K. S., Zhukov, A. A. & Shapoval, S. Y. *Nat. Mater.* **2**, 461–463 (2003).
2. Autumn, K. & Peattie, A. M. *Integr. Comp. Biol.* **42**, 1081–1090 (2002).
3. Patankar, N. A. *Langmuir* **20**, 8209–8213 (2004).
4. Zan, G. & Wu, Q. *Adv. Mater.* **28**, 2099–2147 (2016).
5. Philippe Tingaut, C. E. and T. Z. *Intech Open* **32**, 137–144 (2013).
6. Hawthorn, A. C. & Opell, B. D. *J. Exp. Biol.* **206**, 3905–3911 (2003).
7. Wolf, B., Scirocco, R., Frith, W. J. & Norton, I. T. *Food Hydrocoll.* **14**, 217–225 (2000).
8. Fernández Farrés, I. & Norton, I. T. *Food Hydrocoll.* **40**, 76–84 (2014).
9. Xue, J., Wu, T., Dai, Y. & Xia, Y. *Chem. Rev.* **119**, 5298–5415 (2019).
10. Hassan, M. A., Yeom, B. Y., Wilkie, A., Pourdeyhimi, B. & Khan, S. A. *J. Memb. Sci.* **427**, 336–344 (2013).
11. Zhang, L. & Webster, T. J. *Nano Today* **4**, 66–80 (2009).
12. Kumbar, S. G., James, R., Nukavarapu, S. P. & Laurencin, C. T. *Biomed. Mater.* (2008) doi:10.1088/1748-6041/3/3/034002.
13. Ohan S. Manoukian, Rita Matta, Justin Letendre, P. C. & Augustus D. Mazzocca, and S. G. K. in *Biomedical Nanotechnology* (eds. Petrosko, S. H. and & Day, E. S.) (Springer US, 2017).
14. Blocher, W. C. & Perry, S. L. *Wiley Interdiscip. Rev. Nanomedicine Nanobiotechnology* **9**, 76–78 (2017).
15. Thoniyot, P., Tan, M. J., Karim, A. A., Young, D. J. & Loh, X. J. *Adv. Sci.* **2**, 1400010 (2015).
16. Shewan, H. M. & Stokes, J. R. *J. Food Eng.* **119**, 781–792 (2013).
17. Nuraje, N., Khan, W. S., Lei, Y., Ceylan, M. & Asmatulu, R. *J. Mater. Chem. A* **1**, 1929–1946 (2013).
18. Golovin, K., Kobaku, S. P. R., Lee, D. H., DiLoreto, E. T., Mabry, J. M. & Tuteja, A. *Sci. Adv.* **2**, (2016).
19. Feng, B. L., Li, S. H., Li, Y. S., Li, H. J., Zhang, L. J., Zhai, J., Song, Y. L., Liu, B. Q., Jiang, L., Feng, L., Li, S. H., Li, Y. S., Li, H. J., Zhang, L. J., Zhai, J., Song, Y. L., Liu, B. Q., Jiang, L. & Zhu, D. B. *Adv. Mater.* **14**, 1857–1860 (2002).
20. Morin, B., Hennessy, J. & Arora, P. *Advances in Technical Nonwovens* (Elsevier Ltd, 2016). doi:10.1016/B978-0-08-100575-0.00011-5.
21. Yanilmaz, M., Lu, Y., Dirican, M., Fu, K. & Zhang, X. *J. Memb. Sci.* **456**, 57–65 (2014).
22. Li, Y., Li, Q. & Tan, Z. *J. Power Sources* **443**, 227262 (2019).
23. Saad, W. S. & Prud'Homme, R. K. *Nano Today* **11**, 212–227 (2016).
24. Richter, A. P., Bharti, B., Armstrong, H. B., Brown, J. S., Plemmons, D., Paunov, V. N., Stoyanov, S. D. & Velev, O. D. *Langmuir* **32**, 6468–6477 (2016).
25. Lee, H., Inoue, Y., Kim, M., Ren, X. & Kim, I. S. *Polymers (Basel)*. **10**, (2018).
26. Li, D. & Xia, Y. *Adv. Mater.* **16**, 1151–1170 (2004).
27. Shang, L., Yu, Y., Liu, Y., Chen, Z., Kong, T. & Zhao, Y. *ACS Nano* **13**, 2749–2772 (2019).
28. Bresee, R. R. & Qureshi, U. A. *Int. Nonwovens J.* **14**, (2005).
29. Hassan, M. A., Yeom, B. Y., Wilkie, A., Pourdeyhimi, B. & Khan, S. A. *J. Memb. Sci.* **427**, 336–344 (2013).
30. Haase, M. F., Stebe, K. J. & Lee, D. *Adv. Mater.* **27**, 7065–7071 (2015).

31. Alghoraibi, I. & Alomari, S. *Handbook of Nanofibers* (2019). doi:10.1007/978-3-319-53655-2\_11.
32. Das, B. P. & Tsianou, M. *Adv. Colloid Interface Sci.* **244**, 71–89 (2017).
33. Affinito, J. D., Gross, M. E., Coronado, C. A., Graff, G. L., Greenwell, E. N. & Martin, P. M. *Thin Solid Films* **290–291**, 63–67 (1996).
34. Xiao, F.-X., Pagliaro, M., Xu, Y.-J. & Liu, B. *Chem. Soc. Rev.* **45**, 3088–3121 (2016).
35. Gucht, J. van der, Spruijt, E., Lemmers, M. & Cohen Stuart, M. A. *J. Colloid Interface Sci.* **361**, 407–422 (2011).
36. (Springer Nature).
37. Ren, Y., Yu, C., Chen, Z. & Xu, Y. *Nano Res.* **14**, 2023–2036 (2021).
38. Berglund, L., Noël, M., Aitomäki, Y., Öman, T. & Oksman, K. *Ind. Crops Prod.* **92**, 84–92 (2016).
39. Czaja, W., Romanovicz, D. & Brown, R. malcolm. *Cellulose* **11**, 403–411 (2004).
40. Huang, Z. M., Zhang, Y. Z., Kotaki, M. & Ramakrishna, S. *Compos. Sci. Technol.* **63**, 2223–2253 (2003).
41. Metzner, A. B. *J. Rheol. (N. Y. N. Y.)* **29**, 739–775 (1985).
42. Raghavan, S. & Khan, S. *J. Colloid Interface Sci.* **185**, 57–67 (1997).
43. Mandelbrot, B. B. *American Journal of Physics* vol. 51 (W. H. Freeman and Company, 1983).
44. Dvornic, P. R. & Uppuluri, S. *Dendrimers Other Dendritic Polym.* **1**, 331–358 (2002).
45. Perazzo, A., Nunes, J. K., Guido, S. & Stone, H. A. *Proc. Natl. Acad. Sci. U. S. A.* **114**, E8557–E8564 (2017).
46. Shesan, O. J., Stephen, A. C., Chioma, A. G. & Neerish, Revaprasadu and Rotimi, S. E. in *Composites from Renewable and Sustainable Materials* 1–30 (IntechOpen, 2019). doi:10.5772/57353.
47. Rose, S., Prevoteau, A., Elzière, P., Hourdet, D., Marcellan, A. & Leibler, L. *Nature* **505**, 382–5 (2014).
48. Hanemann, T. & Szabó, D. V. *Materials* vol. 3 (2010).
49. Al-Saleh, M. H. & Sundararaj, U. *Compos. Part A Appl. Sci. Manuf.* **42**, 2126–2142 (2011).
50. Mohan, S., Koenderink, G. H. & Velikov, K. P. *Soft Matter* (2018) doi:10.1039/C8SM00904J.
51. Moberg, T., Sahlin, K., Yao, K., Geng, S., Westman, G., Zhou, Q., Oksman, K. & Rigdahl, M. *Cellulose* **24**, 2499–2510 (2017).
52. Wang, G., Yu, D., Kelkar, A. D. & Zhang, L. *Prog. Polym. Sci.* **75**, 73–107 (2017).
53. Kizilova, N. in *Nanoplasmonics, Nano-optics, Nanocomposites, and Surface Studies* (eds. Fesenjo, O. & Yatsenko, L.) (Springer, 2014).
54. Masselter, T., Hesse, L., Böhm, H., Gruhl, A., Schwager, H., Leupold, J., Gude, M., Milwich, M., Neinhuis, C. & Speck, T. *Bioinspiration and Biomimetics* **11**, (2016).
55. Zhu, J., Yang, M., Emre, A., Bahng, J. H., Xu, L., Yeom, J., Yeom, B., Kim, Y., Johnson, K., Green, P. & Kotov, N. A. *Angew. Chemie - Int. Ed.* **56**, 11744–11748 (2017).
56. Das, C. & Gebru, A. K. (CRC Press, 2018).
57. Huang, X. *J. Solid State Electrochem.* **15**, 649–662 (2011).
58. Guillen, G. R., Pan, Y., Li, M. & Hoek, E. M. V. *Ind. Eng. Chem. Res.* **50**, 3798–3817 (2011).
59. Kriegel, C., Arrechi, A., Kit, K., McClements, D. J. & Weiss, J. *Crit. Rev. Food Sci. Nutr.*

- 48**, 775–797 (2008).
60. Alargova, R. G., Bhatt, K. H., Paunov, V. N. & Velev, O. D. *Adv. Mater.* **16**, 1653–1657 (2004).
  61. Alargova, R. G., Paunov, V. N. & Velev, O. D. *Langmuir* **22**, 765–774 (2006).
  62. Smoukov, S. K., Tian, T., Vitichuli, N., Gangwal, S., Geisen, P., Wright, M., Shim, E., Marquez, M., Fowler, J. & Velev, O. D. *Adv. Mater.* **27**, 2642–2647 (2015).
  63. Sreenivasan, K. R. & Meneveau, C. *J. Fluid Mech.* **173**, 357–386 (1986).
  64. Hultmark, M., Vallikivi, M., Bailey, S. C. C. & Smits, A. J. *Phys. Rev. Lett.* **108**, 094501 (2012).
  65. Roh, S., Williams, A. H., Bang, R. S., Stoyanov, S. D. & Velev, O. D. *Nat. Mater.* **18**, 1315–1320 (2019).
  66. Scotti, A. & Meneveau, C. *Phys. D Nonlinear Phenom.* **127**, 198–232 (1999).
  67. Zhou, H., Zhang, Z., Sun, C., Deng, H. & Fu, Q. *ACS Appl. Mater. Interfaces* **12**, 51506–51516 (2020).
  68. Decher, G. *Science (80- )*. **277**, 1232–1237 (1997).
  69. Jeong, S. I., Krebs, M. D., Bonino, C. A., Samorezov, J. E., Khan, S. A. & Alsberg, E. *Tissue Eng. - Part A* **17**, 59–70 (2011).
  70. Song, Y., Meyers, K. P., Geringer, J., Ramakrishnan, R. K., Humood, M., Qin, S., Polycarpou, A. A., Nazarenko, S. & Grunlan, J. C. *Macromol. Rapid Commun.* **38**, 1–7 (2017).
  71. Cho, C., Xiang, F., Wallace, K. L. & Grunlan, J. C. *Macromolecules* **48**, 5723–5729 (2015).
  72. Skorb, E. V. & Andreeva, D. V. *Polym. Int.* **64**, 713–723 (2015).
  73. Choi, J. & Rubner, M. F. *Macromolecules* **38**, 116–124 (2005).
  74. Schönhoff, M. & Bieker, P. *Macromolecules* **43**, 5052–5059 (2010).
  75. Fu, J., Ji, J., Shen, L., Küller, A., Rosenhahn, A., Shen, J. & Grunze, M. *Langmuir* **25**, 672–675 (2009).
  76. Boddohi, S., Killingsworth, C. E. & Kipper, M. J. *Biomacromolecules* **9**, 2021–2028 (2008).
  77. Yang, Y. H., Haile, M., Park, Y. T., Malek, F. A. & Grunlan, J. C. *Macromolecules* **44**, 1450–1459 (2011).
  78. Laufer, G., Kirkland, C., Cain, A. A. & Grunlan, J. C. *ACS Appl. Mater. Interfaces* **4**, 1643–1649 (2012).
  79. Holder, K. M., Spears, B. R., Huff, M. E., Priolo, M. A., Harth, E. & Grunlan, J. C. *Macromol. Rapid Commun.* **35**, 960–964 (2014).
  80. Vartiainen, J., Vähä-Nissi, M. & Harlin, A. *Mater. Sci. Appl.* **05**, 708–718 (2014).
  81. Lee, K. Y. & Mooney, D. J. *Prog. Polym. Sci.* **37**, 106–126 (2012).
  82. Rinaudo, M. *Prog. Polym. Sci.* **31**, 603–632 (2006).
  83. Goy, R. C., Britto, D. de & Assis, O. B. G. *Polímeros* **19**, 241–247 (2009).
  84. Silva, J. M., Caridade, S. G., Oliveira, N. M., Reis, R. L. & Mano, J. F. *J. Mater. Chem. B* **3**, 4555–4568 (2015).
  85. Gierszewska, M., Ostrowska-Czubenko, J. & Chrzanowska, E. *Eur. Polym. J.* **101**, 282–290 (2018).
  86. Poverenov, E., Danino, S., Horev, B., Granit, R., Vinokur, Y. & Rodov, V. *Food Bioprocess Technol.* **7**, 1424–1432 (2014).
  87. Kopacic, S., Walzl, A., Zankel, A., Leitner, E. & Bauer, W. *Coatings* **8**, 235 (2018).

88. Bilbao-Sainz, C., Chiou, B. Sen, Punotai, K., Olson, D., Williams, T., Wood, D., Rodov, V., Poverenov, E. & McHugh, T. *J. Food Sci.* **83**, 1880–1887 (2018).
89. Caridade, S. G., Monge, C., Gilde, F., Boudou, T., Mano, J. F. & Picart, C. *Biomacromolecules* **14**, 1653–1660 (2013).
90. Fu, J. & Guo, Z. *New J. Chem.* **42**, 17162–17180 (2018).
91. Kulig, D., Zimoch-Korzycka, A., Jarmoluk, A. & Marycz, K. *Polymers (Basel)*. **8**, 1–17 (2016).
92. Liao, I. C., Wan, A. C. A., Yim, E. K. F. & Leong, K. W. *J. Control. Release* (2005) doi:10.1016/j.jconrel.2005.02.013.
93. Sun, J. Y., Zhao, X., Illeperuma, W. R. K., Chaudhuri, O., Oh, K. H., Mooney, D. J., Vlassak, J. J. & Suo, Z. *Nature* **489**, 133–136 (2012).
94. Pääkko, M., Ankerfors, M., Kosonen, H., Nykänen, A., Ahola, S., Österberg, M., Ruokolainen, J., Laine, J., Larsson, P. T., Ikkala, O. & Lindström, T. *Biomacromolecules* **8**, 1934–1941 (2007).
95. Palleau, E., Morales, D., Dickey, M. D. & Velev, O. D. *Nat. Commun.* **4**, 1–7 (2013).
96. Haque, M. A., Kurokawa, T., Kamita, G., Yue, Y. & Gong, J. P. *Chem. Mater.* **23**, 5200–5207 (2011).
97. Zhao, X., Kim, J., Cezar, C. A., Huebsch, N., Lee, K., Bouhadir, K. & Mooney, D. J. *Proc. Natl. Acad. Sci.* **108**, 67–72 (2011).
98. Li, J., Celiz, A., Yang, J. Y., Wamala, I., Whyte, W., Seo, B., Vasilyev, N., Vlassak, J., Suo, Z. & Mooney, D. *Science (80-. )*. **357**, 378–381 (2017).
99. Yuk, H., Lin, S., Ma, C., Takaffoli, M., Fang, N. X. & Zhao, X. *Nat. Commun.* **8**, 1–12 (2017).
100. Langer, R. *Nature* **392**, 5–10 (1998).
101. Cayre, O. J., Suk, T. C. & Velev, O. D. *J. Am. Chem. Soc.* **129**, 10801–10806 (2007).
102. Zhao, X. *Soft Matter* **10**, 672–687 (2014).
103. Hong, S., Sycks, D., Chan, H. F., Lin, S., Lopez, G. P., Guilak, F., Leong, K. W. & Zhao, X. *Adv. Mater.* 4035–4040 (2015) doi:10.1002/adma.201501099.
104. Takahashi, R., Sun, T. L., Saruwatari, Y., Kurokawa, T., King, D. R. & Gong, J. P. *Adv. Mater.* **30**, 1–7 (2018).
105. Hu, J., Hiwatashi, K., Kurokawa, T., Liang, S. M., Wu, Z. L. & Gong, J. P. *Macromolecules* **44**, 7775–7781 (2011).
106. Creton, C. *Macromolecules* **50**, 8297–8316 (2017).
107. Gong, J. P., Katsuyama, Y., Kurokawa, T. & Osada, Y. *Adv. Mater.* **15**, 1155–1158 (2003).
108. Takahashi, R., Shimano, K., Okazaki, H., Kurokawa, T., Nakajima, T., Nonoyama, T., King, D. R. & Gong, J. P. *Adv. Mater. Interfaces* **5**, 1–10 (2018).
109. Illeperuma, W. R. K., Sun, J. Y., Suo, Z. & Vlassak, J. J. *Extrem. Mech. Lett.* **1**, 90–96 (2014).
110. Lee, J. & Lee, K. Y. *Macromol. Biosci.* **9**, 671–676 (2009).
111. Bakarich, S. E., Gorkin, R. & Spinks, M. *ACS Appl. Mater. Interfaces* (2014) doi:10.1021/am503878d.
112. Lin, W., Fan, W., Marcellan, A., Hourdet, D. & Creton, C. *Macromolecules* 2554–2563 (2010) doi:10.1021/ma901937r.
113. Dong, Q., Chow, L. C., Wang, T., Frukhtbeyn, S. A., Wang, F., Yang, M. & Mitchell, J. W. *Colloids Surfaces A Physicochem. Eng. Asp.* **457**, 256–262 (2014).

114. Tonsomboon, K., Butcher, A. L. & Oyen, M. L. *Mater. Sci. Eng. C* **72**, 220–227 (2017).
115. Kmetty, Á., Bárány, T. & Karger-Kocsis, J. *Prog. Polym. Sci.* **35**, 1288–1310 (2010).
116. Jenkins, T. L. & Little, D. *Regen. Med.* **4**, 1–14 (2019).
117. Roohani-Esfahani, S. I., Newman, P. & Zreiqat, H. *Sci. Rep.* **6**, 1–8 (2016).
118. Banerjee, H., Suhail, M. & Ren, H. *Biomimetics* **3**, 15 (2018).
119. Capiati, N. J. & Porter, R. S. *J. Mater. Sci.* **10**, 1671–1677 (1975).
120. Roh, S., Parekh, D. P., Bharti, B., Stoyanov, S. D. & Velev, O. D. *Adv. Mater.* **29**, 1–7 (2017).
121. Roh, S. & Velev, O. D. *AIChE J.* **64**, (2018).
122. Roh, S. C., Kim, J. & Kim, C. K. *Carbon N. Y.* **60**, 317–325 (2013).
123. Kovačević, V., Lučić, S. & Cerovečki, Ž. *Int. J. Adhes. Adhes.* **17**, 239–245 (1997).
124. Fu, S. Y., Feng, X. Q., Lauke, B. & Mai, Y. W. *Compos. Part B Eng.* **39**, 933–961 (2008).
125. Izer, A. & Bárány, T. *Express Polym. Lett.* **1**, 790–796 (2007).
126. Matabola, K. P., De Vries, A. R., Moolman, F. S. & Luyt, A. S. *J. Mater. Sci.* **44**, 6213–6222 (2009).
127. Fakirov, S. *Macromol. Mater. Eng.* **298**, 9–32 (2013).
128. Karger-Kocsis, J. & Bárány, T. *Compos. Sci. Technol.* **92**, 77–94 (2014).
129. Rastogi, P. & Kandasubramanian, B. *Biofabrication* **11**, (2019).
130. Asteriadi, A., Sigel, R., Vlassopoulos, D., Meier, G., Dorgan, J. R. & Knauss, D. M. *Macromolecules* **37**, 1016–1022 (2004).
131. Harreis, H. M., Likos, C. N. & Ballauff, M. *J. Chem. Phys.* **118**, 1979–1988 (2003).
132. Raghavan, S. R. & Douglas, J. F. *Soft Matter* **8**, 8539–8546 (2012).
133. Kizilova, N. *J. Therm. Eng.* **1**, 636–646 (2015).
134. Laubie, H., Radjai, F., Pellenq, R. & Ulm, F. J. *Phys. Rev. Lett.* **119**, (2017).
135. Fang, M., Dong, G., Wei, R. & Ho, J. C. *Adv. Energy Mater.* **7**, 1–25 (2017).
136. Cui, W., King, D. R., Huang, Y., Chen, L., Sun, T. L., Guo, Y., Saruwatari, Y., Hui, C. Y., Kurokawa, T. & Gong, J. P. *Adv. Mater.* **32**, 1–9 (2020).
137. Kuo, C. K. & Ma, P. X. *Biomaterials* **22**, 511–21 (2001).
138. Jang, J., Seol, Y. J., Kim, H. J., Kundu, J., Kim, S. W. & Cho, D. W. *J. Mech. Behav. Biomed. Mater.* **37**, 69–77 (2014).
139. Cardenas-Vasquez, E. D., Smith, K. M., Doolan, T. J. & Hsiao, L. C. *ACS Appl. Polym. Mater.* **2**, 594–603 (2020).
140. Hsiao, L. C., Newman, R. S., Glotzer, S. C. & Solomon, M. J. *Proc. Natl. Acad. Sci. U. S. A.* **109**, 16029–16034 (2012).
141. Moghimi, E., Jacob, A. R., Koumakis, N. & Petekidis, G. *Soft Matter* **13**, 2371–2383 (2017).
142. Chambon, F. & Winter, H. H. *J. Rheol. (N. Y. N. Y.)* **31**, 683–697 (1987).
143. Fernández Farrés, I., Douaire, M. & Norton, I. T. *Food Hydrocoll.* **32**, 115–122 (2013).
144. Fernández Farrés, I., Moakes, R. J. A. & Norton, I. T. *Food Hydrocoll.* **42**, 362–372 (2014).
145. Xu, C., Chai, W., Huang, Y. & Markwald, R. R. *Biotechnol. Bioeng.* **109**, 3152–3160 (2012).
146. Minas, C., Carnelli, D., Tervoort, E. & Studart, A. R. *Adv. Mater.* **28**, 9993–9999 (2016).
147. Mueller, J., Raney, J. R., Shea, K. & Lewis, J. A. *Adv. Mater.* **30**, 1–8 (2018).
148. Kass, L., Cardenas-Vasquez, E. D. & Hsiao, L. C. *AIChE J.* **65**, 1–8 (2019).
149. Stokes, J. R. *Food Mater. Sci. Eng.* 151–176 (2012) doi:10.1002/9781118373903.ch6.

150. Peng, Y., Serfass, C. M., Hill, C. N. & Hsiao, L. C. *arXiv Prepr.* (2019).
151. Deloid, G. M., Cohen, J. M., Pyrgiotakis, G. & Demokritou, P. *Nat. Protoc.* **12**, 355–371 (2017).
152. Cohen, J., Ji, Z., Xia, T. & Demokritou, P. *Part. Fibre Toxicol.* **11**, 1–12 (2014).
153. Deloid, G., Cohen, J. M., Darrah, T., Derk, R., Rojanasakul, L., Pyrgiotakis, G., Wohlleben, W. & Demokritou, P. *Nat. Commun.* **5**, 1–10 (2014).
154. Cohen, J., DeLoid, G., Pyrgiotakis, G. & Demokritou, P. *Nanotoxicology* **7**, 417–431 (2013).
155. Cohen, J. M., DeLoid, G. M. & Demokritou, P. *Nanomedicine* **10**, 3015–3032 (2015).
156. Herzog, F., Loza, K., Balog, S., Clift, M. J. D., Epple, M., Gehr, P., Petri-Fink, A. & Rothen-Rutishauser, B. *Beilstein J. Nanotechnol.* **5**, 1357–1370 (2014).
157. Tilly, T. B., Nelson, M. T., Chakravarthy, K. B., Shira, E. A., Debrose, M. C., Grabinski, C. M., Salisbury, R. L., Mattie, D. R. & Hussain, S. M. *Chem. Res. Toxicol.* (2020) doi:10.1021/acs.chemrestox.9b00237.
158. Paur, H. R., Cassee, F. R., Teeguarden, J., Fissan, H., Diabate, S., Aufderheide, M., Kreyling, W. G., Hänninen, O., Kasper, G., Riediker, M., Rothen-Rutishauser, B. & Schmid, O. *J. Aerosol Sci.* **42**, 668–692 (2011).
159. Hussain, S. M., Warheit, D. B., Ng, S. P., Comfort, K. K., Grabinski, C. M. & Braydich-Stolle, L. K. *Toxicol. Sci.* **147**, 5–16 (2015).
160. Boomer, L., Liu, Y., Mahler, N., Johnson, J., Zak, K., Nelson, T., Lannutti, J. & Besner, G. E. *J. Biomed. Mater. Res. - Part A* **102**, 3795–3802 (2014).
161. Luque, T., Melo, E., Garreta, E., Cortiella, J., Nichols, J., Farré, R. & Navajas, D. *Acta Biomater.* **9**, 6852–6859 (2013).
162. Ameer, J. M., Anil Kumar, P. R. & Kasoju, N. *J. Funct. Biomater.* **10**, 1–21 (2019).
163. Pizzo, A. M., Kokini, K., Vaughn, L. C., Waisner, B. Z. & Voytik-Harbin, S. L. *J. Appl. Physiol.* **98**, 1909–1921 (2005).
164. Jeon, H., Tsui, J. H., Jang, S. I., Lee, J. H., Park, S., Mun, K., Boo, Y. C. & Kim, D. H. *ACS Appl. Mater. Interfaces* **7**, 4525–4532 (2015).
165. Truby, R. L. & Lewis, J. A. *Nature* **540**, 371–378 (2016).
166. Mitchell, G. R. & Tojeira, A. *Procedia Eng.* **59**, 117–125 (2013).
167. Chen, S., John, J. V., Mccarthy, A., Carlson, M. A., Li, X. & Xie, J. *Appl. Phys. Rev.* **021406**, (2020).
168. Huang, C., Ozdemir, T., Xu, L. C., Butler, P. J., Siedlecki, C. A., Brown, J. L. & Zhang, S. *J. Biomed. Mater. Res. - Part B Appl. Biomater.* **104**, 488–495 (2016).
169. Ataollahi, F., Pramanik, S., Moradi, A., Dalilottojari, A., Pingguan-Murphy, B., Wan Abas, W. A. B. & Abu Osman, N. A. *J. Biomed. Mater. Res. - Part A* **103**, 2203–2213 (2015).
170. Sun, M., Chi, G., Li, P., Lv, S., Xu, J., Xu, Z., Xia, Y., Tan, Y., Xu, J., Li, L. & Li, Y. *Int. J. Med. Sci.* **15**, 257–268 (2018).
171. Xu, Q., Li, C., Kang, Y. & Zhang, Y. *RSC Adv.* **5**, 105651–105660 (2015).
172. Barker, T. H., Dysart, M. M., Brown, A. C., Douglas, A. M., Fiore, V. F. & Russell, A. G. *Health Effects Institute* (2014).
173. Huang, C., Butler, P. J., Tong, S., Muddana, H. S., Bao, G. & Zhang, S. *Nano Lett.* **13**, 1611–1615 (2013).
174. Bitterle, E., Karg, E., Schroepfel, A., Kreyling, W. G., Tippe, A., Ferron, G. A., Schmid, O., Heyder, J., Maier, K. L. & Hofer, T. *Chemosphere* **65**, 1784–1790 (2006).

175. Melo, E., Cárdenes, N., Garreta, E., Luque, T., Rojas, M., Navajas, D. & Farré, R. J. *Mech. Behav. Biomed. Mater.* **37**, 186–195 (2014).
176. Nelson, M. T., Short, A., Cole, S. L., Gross, A. C., Winter, J., Eubank, T. D. & Lannutti, J. J. *BMC Cancer* **14**, 1–16 (2014).
177. Tarascon, J. M. & Armand, M. *Nature* **414**, 359–67 (2001).
178. Yang, M. & Hou, J. *Membranes (Basel)*. **2**, 367–383 (2012).
179. Deimede, V. & Elmasides, C. *Energy Technol.* **3**, 453–468 (2015).
180. Heidari, A. A. & Mahdavi, H. *Chem. Rec.* **20**, 570–595 (2020).
181. Choi, S. S., Lee, Y. S., Joo, C. W., Lee, S. G., Park, J. K. & Han, K. S. *Electrochim. Acta* **50**, 339–343 (2004).
182. Lee, H., Yanilmaz, M., Toprakci, O., Fu, K. & Zhang, X. *Energy Environ. Sci.* **7**, 3857–3886 (2014).
183. Alkindi, A. S., Al-Wahaibi, Y. M. & Muggeridge, A. H. *J. Chem. Eng. Data* **53**, 2793–2796 (2008).
184. Caliari, S. R. & Harley, B. A. C. *Biomaterials* **32**, 5330–5340 (2011).
185. Zhao, G., Zhang, X., Lu, T. J. & Xu, F. *Adv. Funct. Mater.* **25**, 5726–5738 (2015).
186. Araujo, J., Padrão, J., Silva, J. P., Dourado, F., Correia, D. M., Botelho, G., Gomez Ribelles, J. L., Lanceros-Méndez, S. & Sencadas, V. *Appl. Phys. A Mater. Sci. Process.* **115**, 1291–1298 (2014).
187. Kumbar, S. G., James, R., Nukavarapu, S. P. & Laurencin, C. T. *Biomed. Mater.* **3**, (2008).
188. Luiso, S. & Fedkiw, P. *Curr. Opin. Electrochem.* **20**, 99–107 (2020).
189. Freed, L. E., Engelmayer Jr., G. C., Borenstein, J. T., Moutos, F. T. & Guilak, F. *Adv. Mater.* **21**, 3410–3418 (2009).
190. Morris, G. E., Bridge, J. C., Eltboli, O. M. I., Knox, A. J., Aylott, J. W., Brightling, C. E., Ghaemmaghami, A. M. & Rose, F. R. A. *J. Am. J. Physiol. - Lung Cell. Mol. Physiol.* **307**, 38–47 (2014).
191. Sas, I., Gorga, R. E., Joines, J. A. & Thoney, K. A. *J. Polym. Sci. Part B Polym. Phys.* **50**, 824–845 (2012).
192. Fillion, R. M., Riahi, A. R. & Edrisy, A. *Renew. Sustain. Energy Rev.* **32**, 797–809 (2014).
193. Nosonovsky, M. & Bhushan, B. *Curr. Opin. Colloid Interface Sci.* **14**, 270–280 (2009).
194. Darmanin, T. & Guittard, F. *J. Mater. Chem. A* **2**, 16319–16359 (2014).
195. Ai, J. & Guo, Z. *Chem. Commun.* (2019) doi:10.1039/C9CC03813B.
196. Meuler, A. J., Smith, J. D., Varanasi, K. K., Mabry, J. M., McKinley, G. H. & Cohen, R. E. *ACS Appl. Mater. Interfaces* **2**, 3100–3110 (2010).
197. Wang, H., He, G. & Tian, Q. *Appl. Surf. Sci.* **258**, 7219–7224 (2012).
198. Cao, L., Jones, A. K., Sikka, V. K., Wu, J. & Gao, D. *Langmuir* **25**, 12444–12448 (2009).
199. Yilgor, I., Bilgin, S., Isik, M. & Yilgor, E. *Polymer (Guildf)*. **53**, 1180–1188 (2012).
200. Lin, Y., Chen, H., Wang, G. & Liu, A. *Coatings* **8**, (2018).
201. Ensikat, H. J., Ditsche-Kuru, P., Neinhuis, C. & Barthlott, W. *Beilstein J. Nanotechnol.* **2**, 152–161 (2011).
202. Gao, L. & McCarthy, T. J. *Langmuir* **25**, 14105–14115 (2009).
203. Lv, J., Song, Y., Jiang, L. & Wang, J. *ACS Nano* **8**, 3152–3169 (2014).
204. Pan, Z., Cheng, F. & Zhao, B. *Polymers (Basel)*. **9**, 32–39 (2017).
205. Szweczyk, P. K., Ura, D. P., Metwally, S., Knapczyk-Korczak, J., Gajek, M., Marzec, M. M., Bernasik, A. & Stachewicz, U. *Polymers (Basel)*. **11**, (2018).

206. Huang, F. L., Wang, Q. Q., Wei, Q. F., Gao, W. D., Shou, H. Y. & Jiang, S. D. *Express Polym. Lett.* **4**, 551–558 (2010).
207. Eberle, P., Tiwari, M. K., Maitra, T. & Poulidakos, D. *Nanoscale* **6**, 4874–4881 (2014).
208. Sarshar, M. A., Song, D., Swartz, C., Lee, J. & Choi, C.-H. *Langmuir* **34**, acs.langmuir.8b02231 (2018).
209. Metya, A. K., Singh, J. K. & Müller-Plathe, F. *Phys. Chem. Chem. Phys.* **18**, 26796–26806 (2016).
210. Milles, S., Soldera, M., Voisiat, B. & Lasagni, A. F. *Sci. Rep.* **9**, 1–13 (2019).
211. Sojoudi, H., Wang, M., Boscher, N. D., McKinley, G. H. & Gleason, K. K. *Soft Matter* **12**, 1938–63 (2016).
212. Zhang, X., Guo, Y., Chen, H., Zhu, W. & Zhang, P. *J. Mater. Chem. A* **2**, 9002–9006 (2014).
213. Ramakrishna, S., Kumar, K. S. S., Mathew, D. & Reghunadhan Nair, C. P. *Sci. Rep.* **5**, 1–12 (2015).
214. Wang, C., Zhang, W., Siva, A., Tiew, D. & Wynne, K. J. *Langmuir* **30**, 540–547 (2014).
215. Bonn, D., Eggers, J., Indekeu, J. & Meunier, J. *Rev. Mod. Phys.* **81**, 739–805 (2009).
216. Ebnesajjad, S. in *Handbook of Adhesives and Surface Preparation* 21–30 (Elsevier Inc., 2011). doi:10.1016/B978-1-4377-4461-3.10003-3.
217. Stachewicz, U., Hang, F. & Barber, A. H. *Langmuir* **30**, 6819–6825 (2014).
218. Johnson, K. L., Kendall, K. & Roberts, A. D. *J. Phys. D. Appl. Phys.* **324**, 301–313 (1971).
219. Sojoudi, H., Khanouki, H. A., Walsh, M., Shirazi, S., McKinley, G. & Gleason, K. *Abstr. Pap. 251st ACS Natl. Meet. Expo. San Diego, CA, United States, March 13-17, 2016* POLY-563 (2016) doi:10.1039/C8SM00225H.
220. Alizadeh, A., Yamada, M., Li, R., Shang, W., Otta, S., Zhong, S., Ge, L., Dhinojwala, A., Conway, K. R., Bahadur, V., Vinciguerra, A. J., Stephens, B. & Blohm, M. L. *Langmuir* **28**, 3180–3186 (2012).
221. Wang, L., Wang, R., Wang, J. & Wong, T.-S. *Sci. Adv.* **6**, eabb2307 (2020).
222. Salame, M. & Steingiser, S. *Polym. Plast. Technol. Eng.* **8**, 155–175 (1977).
223. Arnon-Rips, H. & Poverenov, E. *Trends Food Sci. Technol.* **75**, 81–92 (2018).
224. Miller, K. S. & Krochta, J. M. *Trends Food Sci. Technol.* **8**, 228–237 (1997).
225. Senturk Parreidt, T., Müller, K. & Schmid, M. *Foods* **7**, 170 (2018).
226. Decher, G., Hong, J. D. & Schmitt, J. *Thin Solid Films* **210–211**, 831–835 (1992).
227. Priolo, M. A., Gamboa, D., Holder, K. M. & Grunlan, J. C. *Nano Lett.* **10**, 4970–4974 (2010).
228. Priolo, M. A., Holder, K. M., Guin, T. & Grunlan, J. C. *Macromol. Rapid Commun.* **36**, 866–879 (2015).
229. Xiang, F., Ward, S. M., Givens, T. M. & Grunlan, J. C. *ACS Macro Lett.* **3**, 1055–1058 (2014).
230. Lutkenhaus, J. L., Hrabak, K. D., McEnnis, K. & Hammond, P. T. *J. Am. Chem. Soc.* **127**, 17228–17234 (2005).
231. Wang, H., Qian, J. & Ding, F. *J. Agricultural Food Chem.* **66**, 395–413 (2018).
232. K. Y. Lee, D. J. M. *Prog. Polym. Sci.* **37**, 106–126 (2012).
233. Kuo, C. K. & Ma, P. X. *Biomaterials* **22**, 511–521 (2001).
234. Hirvikorpi, T., Vähä-Nissi, M., Harlin, A., Salomäki, M., Areva, S., Korhonen, J. T. & Karpinen, M. *Appl. Surf. Sci.* **257**, 9451–9454 (2011).

235. Li, K., Zhu, J., Guan, G. & Wu, H. *Int. J. Biol. Macromol.* **122**, 485–492 (2019).
236. Acevedo-Fani, A., Salvia-Trujillo, L., Soliva-Fortuny, R. & Martín-Belloso, O. *Food Biophys.* **12**, 299–308 (2017).
237. De Levie, R. *J. Chem. Educ.* **80**, 146 (2003).
238. Kittitheeranun, P., Dubas, S. T. & Dubas, L. *Appl. Mech. Mater.* **229–231**, 2745–2748 (2012).
239. Roberts, A. P., Henry, B. M., Sutton, A. P., Miyamoto, T., Kano, M., Tsukahara, Y. & Yanaka, M. *J. Memb. Sci.* **208**, 75–88 (2002).
240. Cooksey, K., Marsh, K. S. and Doar, L. H. *Food Technol.* **53**, 60–63 (1999).
241. Salomäki, M., Vinokurov, I. A. & Kankare, J. *Langmuir* **21**, 11232–11240 (2005).
242. Tan, H. L., McMurdo, M. J., Pan, G. & Van Patten, P. G. *Langmuir* **19**, 9311–9314 (2003).
243. Michel, M., Toniazzo, V., Ruch, D. & Ball, V. *ISRN Mater. Sci.* **2012**, 1–13 (2012).
244. Li, F., Biagioni, P., Finazzi, M., Tavazzi, S. & Piergiovanni, L. *Carbohydr. Polym.* **92**, 2128–2134 (2013).
245. Rhim, J. W., Mohanty, K. A., Singh, S. P. & Ng, P. K. W. *Ind. Eng. Chem. Res.* **45**, 3059–3066 (2006).
246. GENNADIOS, A., WELLER, C. L. & TESTIN, R. *J. Food Sci.* **58**, 212–214 (1993).
247. BUTLER, B. L., VERGANO, P. J., TESTIN, R. F., BUNN, J. M. & WILES, J. L. *J. Food Sci.* **61**, 953–956 (1996).
248. Stading, M., Rindlav-Westling, Å. & Gatenholm, P. *Carbohydr. Polym.* **45**, 209–217 (2001).
249. Cho, S. Y., Lee, S. Y. & Rhee, C. *LWT - Food Sci. Technol.* **43**, 1234–1239 (2010).
250. Zhu, Y., Xuan, H., Ren, J. & Ge, L. *Soft Matter* **11**, 8452–8459 (2015).
251. Schoeler, B., Delorme, N., Doench, I., Sukhorukov, G. B., Fery, A. & Glinel, K. *Biomacromolecules* **7**, 2065–2071 (2006).
252. Jimenez-Solomon, M. F., Song, Q., Jelfs, K. E., Munoz-Ibanez, M. & Livingston, A. G. *Nat. Mater. advance on*, 1–26 (2016).
253. Yu, C. C., Chang, J. J., Lee, Y. H., Lin, Y. C., Wu, M. H., Yang, M. C. & Chien, C. T. *Mater. Lett.* **93**, 133–136 (2013).
254. Luiso, S., Williams, A. H., Petrecca, M. J., Roh, S., Velez, O. D. & Fedkiw, P. S. *J. Electrochem. Soc.* **168**, 020517 (2021).
255. Agarwal, S., Greimer, A. & Wendorff, J. H. *Adv. Funct. Mater.* **19**, 2863–2879 (2009).
256. Roh, S., Okello, L. B., Golbasi, N., Hankwitz, J. P., Liu, J. A., Tracy, J. B. & Velez, O. D. *Adv. Mater. Technol.* **1800528**, 1–6 (2019).
257. Arora, P. & Zhang, Z. *Chem. Rev.* **104**, 4419–4462 (2004).
258. Erbil, H. Y. *Langmuir* **36**, 2493–2509 (2020).

## APPENDICES

## Appendix A

### CHAPTER 2: Biopolymer Soft Dendritic Colloids and Self-Reinforced Homocomposite

#### Hydrogels with a Molecular-Colloidal Double Network

##### Synthetic polyelectrolyte composite soft dendritic colloids

To illustrate that the cSDC polyelectrolyte complexation precipitation mechanism wasn't limited to the Alg and CS biopolyelectrolytes, cSDCs were fabricated using synthetic polyelectrolytes branched polyethyleneimine (BPEI) and polyacrylic acid (PAA). Micrographs of a short systematic experiment in which the injected BPEI solution's concentration was maintained at 35 wt.% in H<sub>2</sub>O, while the PAA nonsolvent solutions concentration was increased from 0.5 wt.% (Figure A1a) – where only chunks were produced – to 2 wt.% (Figure A1c), resulting in BPEI-PAA cSDC morphology. This polyelectrolyte system was chosen as a model for synthetic cSDC particles due to its common use in the layer-by-layer coating technique outlined in Chapter 5.

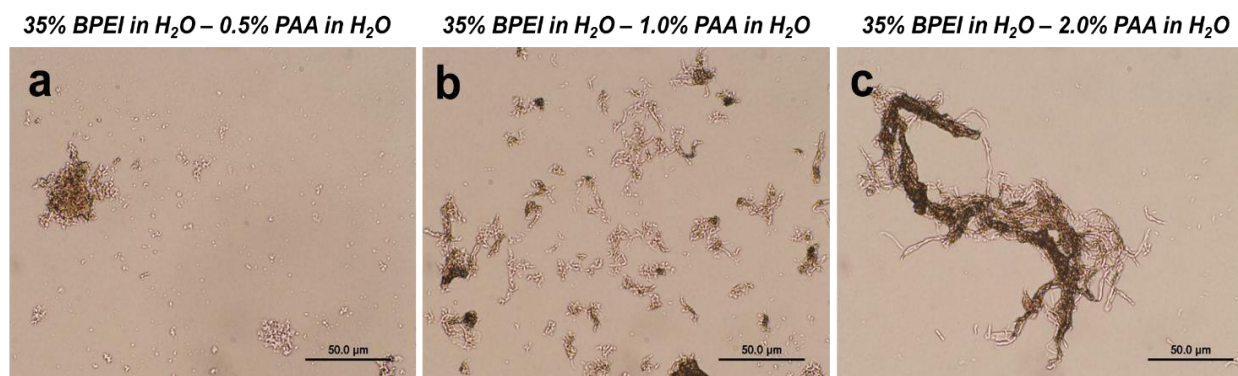


**Figure A1.** Branched polyethyleneimine (BPEI) – polyacrylic acid (PAA) synthetic cSDC morphologies. (a) 35% BPEI – 0.5% PAA resulting in polymer chunks. (b) 35% BPEI – 1.0% PAA resulting in composite microrods. (c) 35% BPEI – 2.0% PAA resulting in cSDCs.

### Alginate hydrogel soft dendritic colloid fabrication

In order to make the nanofibrous reinforcement for HHGs presented herein, we synthesized sodium alginate (SA) hydrogel soft dendritic colloids (hSDCs) with hierarchical, branched micro- and nanofibers. SA hSDCs are fabricated using shear-driven polymer precipitation within a nonsolvent flow of an aqueous  $\text{CaCl}_2$  solution. Upon injection of the SA solution into the turbulently sheared precipitation medium, the solution is randomly and vigorously stretched and templated by the hierarchical turbulent eddies of the  $\text{Ca}^{2+}$  rich medium. Concurrent with the multidirectional deformation of the polymer solution by the turbulent flow, the  $\text{Ca}^{2+}$  ions rapidly diffuse into the stretched SA solution droplet. The simultaneous droplet elongation by turbulent eddies and  $\text{Ca}^{2+}$  diffusion result in the precipitation of the alginate into highly branched and fibrous SA hSDCs. While the morphology remains the same, these hSDCs are fundamentally different from those of our previous report. Herein, we rely upon the rapid, ionic crosslink reaction between alginate and  $\text{Ca}^{2+}$  as the precipitation mechanism to form water-swollen and cross-linked SA hSDC fibers. Contrarily, our previous report utilized nonsolvent-induced precipitation, which resulted in similarly structured, but more densely packed polymer SDC fibers. For simplicity, the SA hSDCs utilized are hereafter referred to as SDCs. While the precipitation mechanisms of the two materials may differ, the resulting particulates of both processes possess the characteristic SDC morphology. We hypothesize that parameters such as temperature, pH, and exposure to light that can induce rapid precipitation in other polymer systems can also be utilized as precipitation mechanisms under shear to obtain SDCs from a vast library of materials.

## Characterization of Alginate SDCs

SA SDC suspensions were washed with deionized water to remove redundant  $\text{Ca}^{2+}$  ions using centrifugation following by decanting and resuspension of the SDC pellet in deionized water. After rinsing, a dilute suspension of SDCs ( $< 0.001$  wt.%) in ethanol was prepared and spin-coated on a silicon wafer and a glass slide to observe individual SA SDCs with a field-emission scanning electron microscopy and optical microscopy (Figure A2a). SDCs can often be particulates spanning hundreds of microns in total diameter (Figure A2b), however, the backbone fibers comprising the greater particulate branch hierarchically until the outer layer (“corona”) consists of thin flexible nanofibers whose networking is dominated by physical interactions and fiber entanglements.

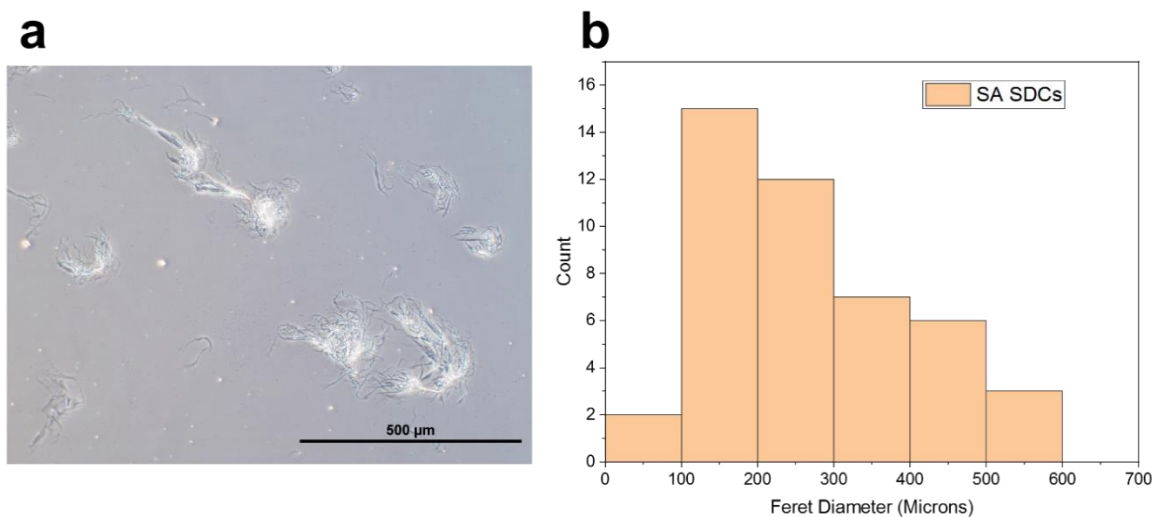


**Figure A2.** Size distribution of SA SDCs. (a) Phase contrast optical micrograph of SA SDCs spin-coated onto a glass slide. (b) Histogram showing the Feret Diameter size distribution of the coronas of nanofibers around the dried SDCs obtained from microscope images ( $n = 45$ ).

The pictures of the SDC solutions in Figure A3 show that while suspensions of SA SDCs show gel-like behavior when analyzed using a frequency sweep down to concentrations of 0.25 wt.%, these dilute suspensions flow upon inversion of their vials until a concentration between 0.50–0.75 wt.%. The impressive network-building capabilities by SDC suspensions are evidenced

by their yield stress behavior at dilute concentrations as low as 0.25 wt.% (Figure A3c), while non-cross-linked SA solutions show Newtonian behavior up to concentrations of 3 wt.%. Interestingly, the SDC suspension at just 0.25 wt.% has a complex modulus nearly matching that of the 3 wt.% SA solution containing 12× the alginate.

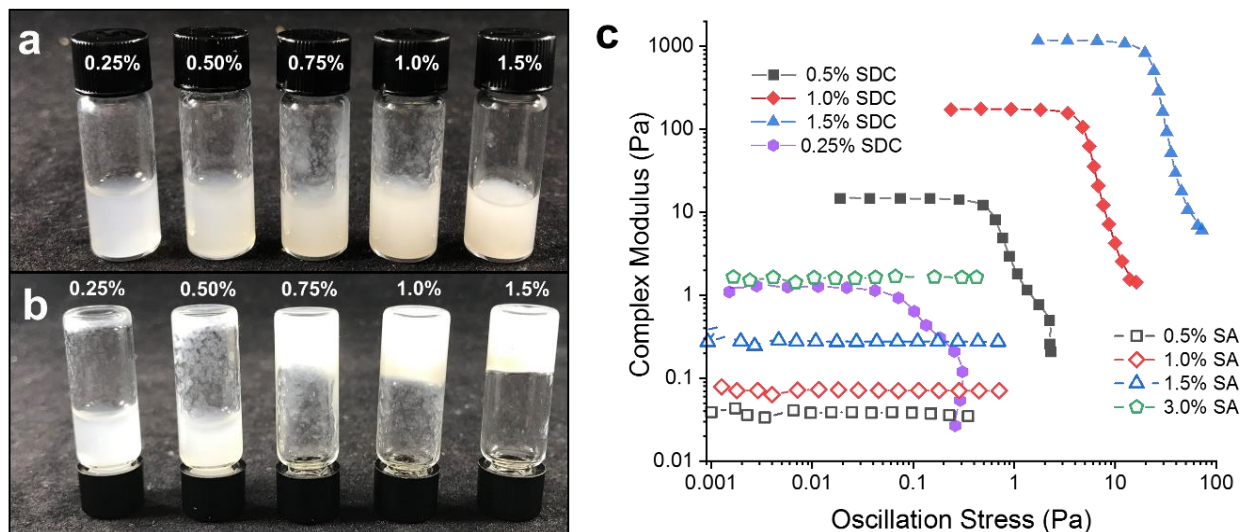


**Figure A3.** Gelation of SA SDC suspensions. Pictures of aqueous SA SDC suspensions at concentrations ranging 0.25 – 1.5 wt.% (a) before and (b) after inversion of the vials indicating apparent yield stress and gel-like behavior with increasing concentration. **c** Amplitude sweeps performed on dissolved SA solutions (unfilled) and aqueous SA SDC suspensions (filled) of varied concentrations showing yield stress behavior in dilute SDC suspensions.

To determine the  $\text{CaCO}_3$  loading capacity of the SA cross-linked molecular hydrogels (CMHs), a series of 1.0 wt.% SA gels were prepared with increasing  $\text{CaCO}_3$  content and the D-Gluconic acid  $\delta$ -lactone (GDL) added to the gels was raised proportionally with the  $\text{CaCO}_3$  content (Figure A4a). These gels showed significant syneresis with increased  $\text{CaCO}_3$  and GDL content, which was quantified by using image analysis to measure the decrease in the area of the gels over time within their 50 mm  $\times$  44 mm  $\times$  1.5 mm acrylic molds (Figure A4b). The SA CMHs containing high  $\text{CaCO}_3$  loading (0.5 wt.% and 1.0 wt.%) do not become completely transparent after 24 hours

indicating incomplete  $\text{CaCO}_3$  dissolution and lose significant volume by syneresis. Next, a set of gels containing 1.0 wt.% SA, 0.5 wt.%  $\text{CaCO}_3$ , and varying concentrations of added GDL were prepared. It can be seen visually that even up to 140.7 mM GDL, the mixture retains its opacity, indicating incomplete dissolution of the  $\text{CaCO}_3$  nanoparticles (Fig B4c).

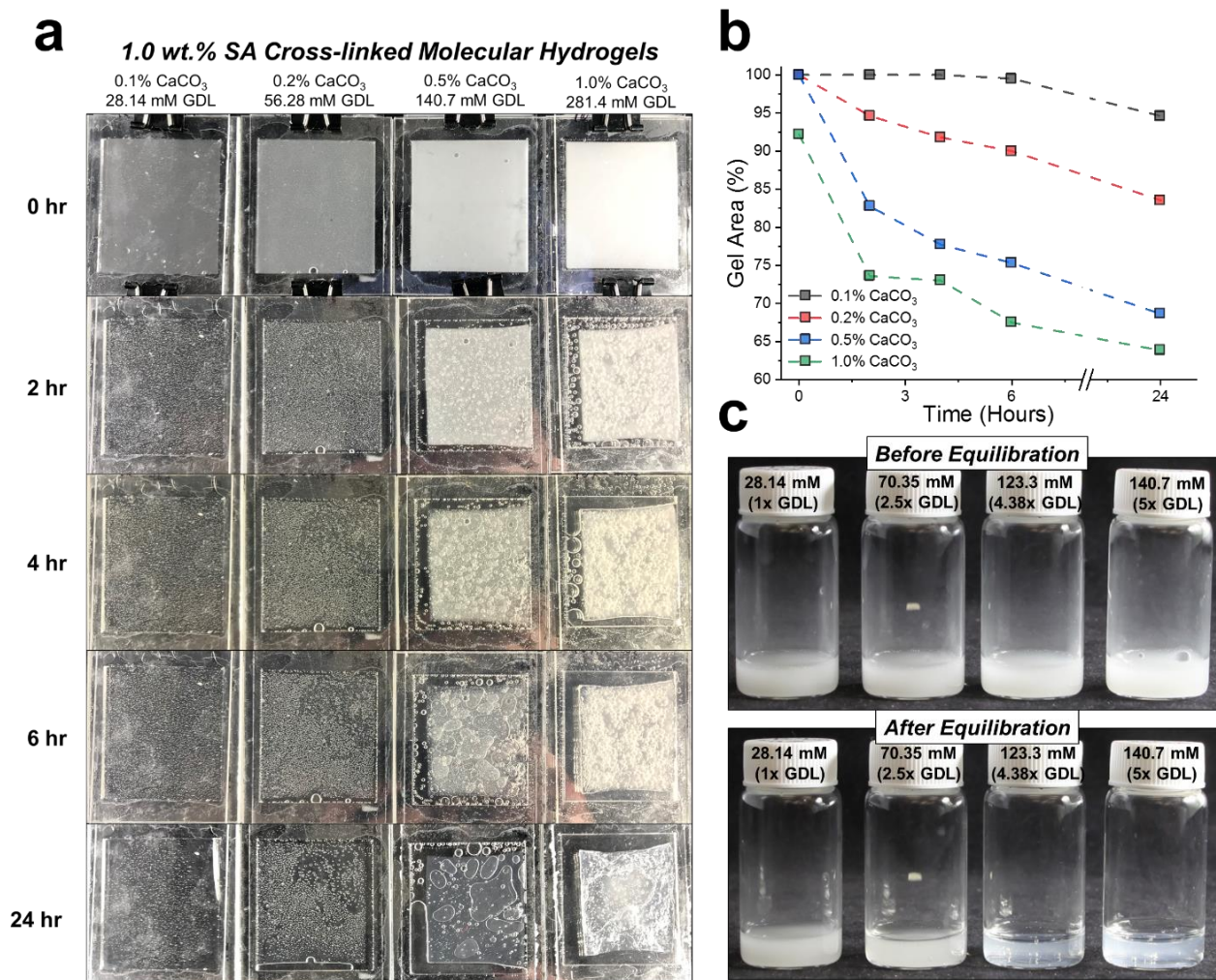


**Figure A4.** Syneresis of SA CMHs with increased  $\text{CaCO}_3$  content. (a) Pictures of gel syneresis prepared in 50 mm × 44 mm × 1.5 mm sealed acrylic molds and (b) the area of the gels over time measured by image analysis in ImageJ of the area loss of the gels over time. c Pictures of 1.0 wt.% SA, 0.5 wt.%  $\text{CaCO}_3$  mixtures immediately after addition of 28.14 – 140.7 mM GDL.

## Elucidating the Role of Calcium in SDC Gelation

To determine the level of calcium incorporated into the fibers of the SA SDCs during fabrication, a 1.0 wt.% suspension of SA SDCs was repeatedly washed with deionized water to remove excess ions from solution and 8 mL of the suspension was deposited in an aluminum dish and dried at 50°C for 24 hours. A 1.0 wt.% molecular alginate gel was also prepared with 0.11 wt.% CaCO<sub>3</sub> NPs and 28.14 mM GDL. This mixture was then deposited in an aluminum weighing dish, allowed to gel, and placed in a 50°C oven for 24 hours to dry to produce a thin, cross-linked alginate film of 10 wt.% CaCO<sub>3</sub>. These films were placed under vacuum for 2 days and analyzed by X-ray photoelectron spectroscopy (XPS, Figure A5). The atomic percentage of calcium in the CMH film was determined to be 0.5 wt.%, while that of the SDC film was found to be 2.6 wt.%, indicating that the SDCs contain approximately 5× the amount of calcium than the molecular alginate film at the prepared concentration.

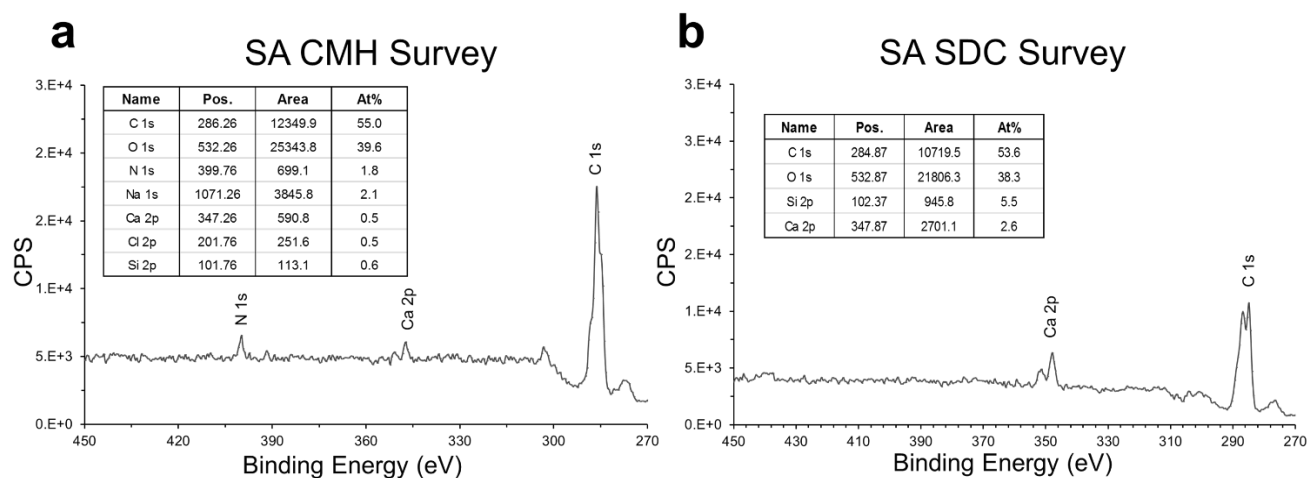


**Figure A5.** X-ray photoelectron spectroscopy analysis of dried molecular alginate and SDC films. (a) XPS spectrum of a dried molecular alginate film prepared with by drying a 1 wt.% SA, 0.10 wt.% CaCO<sub>3</sub> NPs, 28.14 mM GDL CMH into a film. (b) XPS spectrum of a dried SA SDC film after repeated washing an aqueous SDC suspension with deionized water and drying.

With SA SDCs containing appr. 5× the calcium content of the CMH, it is then possible to calculate the concentrations in [mM] of each constituent of the gel (Tables B1 and B2). With the maximum HHG tensile stiffness resulting from HHGs with a composition of 0.125 wt.% SDC/0.875 wt.% (Figure 2.7), it can then be estimated the calcium content of this HHG is appr. 15.2 mM, or 1.5× that of the pure CMH.

**Table A1.** Equilibrium compositions of SA CMH/SDC HHGs in [wt.%].

SA CMH/SDC Homocomposite Compositions (wt.%)

<b>wt.% SDC</b>	<b>0.000</b>	<b>0.125</b>	<b>0.250</b>	<b>0.500</b>	<b>0.750</b>	<b>1.000</b>	
<b>wt.% CMH</b>	<b>1.000</b>	<b>0.875</b>	<b>0.750</b>	<b>0.500</b>	<b>0.250</b>	<b>0.000</b>	
CaCO <sub>3</sub> (wt.%)	0.100	0.0875	0.075	0.050	0.025	0.000	
Total [Ca <sup>2+</sup> ] (wt.%)	0.040	0.061	0.082	0.124	0.166	0.208	
[GDL] (wt.%)	0.500	0.439	0.378	0.250	0.125	0.000	

**Table A2.** Estimated equilibrium compositions of 1.0 wt.% SA CMH/SDC HHGs in [mM].

SA CMH/SDC Homocomposite Compositions (mM)

<b>wt.% SDC</b>	<b>0.000</b>	<b>0.125</b>	<b>0.250</b>	<b>0.500</b>	<b>0.750</b>	<b>1.000</b>	
<b>wt.% CMH</b>	<b>1.000</b>	<b>0.875</b>	<b>0.750</b>	<b>0.500</b>	<b>0.250</b>	<b>0.000</b>	
Total [Ca <sup>2+</sup> ] (mM)	9.991	15.236	20.482	30.972	41.463	51.953	
[GDL] (mM)	28.143	24.625	21.107	14.071	7.036	0.000	

### Structural reversibility comparison of the hydrogel systems

To investigate the reversibility of the Calcium-alginate ionic cross-links in SA HHGs, 1.0 wt.% SA SDC, CMH, and HHG (0.5% SDC, 0.5% CMH) samples were treated with the chelating agent ethylenediaminetetraacetic acid (EDTA). A 1.0 wt.% SA SDC in water suspension was immersed in a 50 mM EDTA solution (Figure A6a). Immediately following the addition of the EDTA solution, a significant loss of turbidity in the suspension is observed as the EDTA sequesters the

Ca<sup>2+</sup> cross-links and the free alginate chains dissolve back into the aqueous phase, while the SDC suspension in pure water sees no appreciable visible change. Samples of 1.0 wt.% SA CMH gel showed similar behavior in water and in EDTA solution (Figure A6b). While the CMH gel stored in water maintained its structure, the CMH sample treated with EDTA exhibited gel fragmentation after 10 minutes and, after 24 hours, nearly complete dissolution of the alginate back into the water phase. The SA SDCs may show more a more rapid degradation in response to EDTA addition because the greater surface area of SDCs in comparison to the CMH gel. Finally, the HHG gel treated with EDTA did show a decrease in gel volume after 24 hours, but maintained the original hydrogel structure, suggesting that the HHG samples may be less prone to gel breakdown by chelating agents (Figure A6c). Absent such strong chelating agents, we found that SDCs and HHGs stored in pure water are stable and maintain their distinct morphological features and rheological behavior after several months of storage at room temperature.

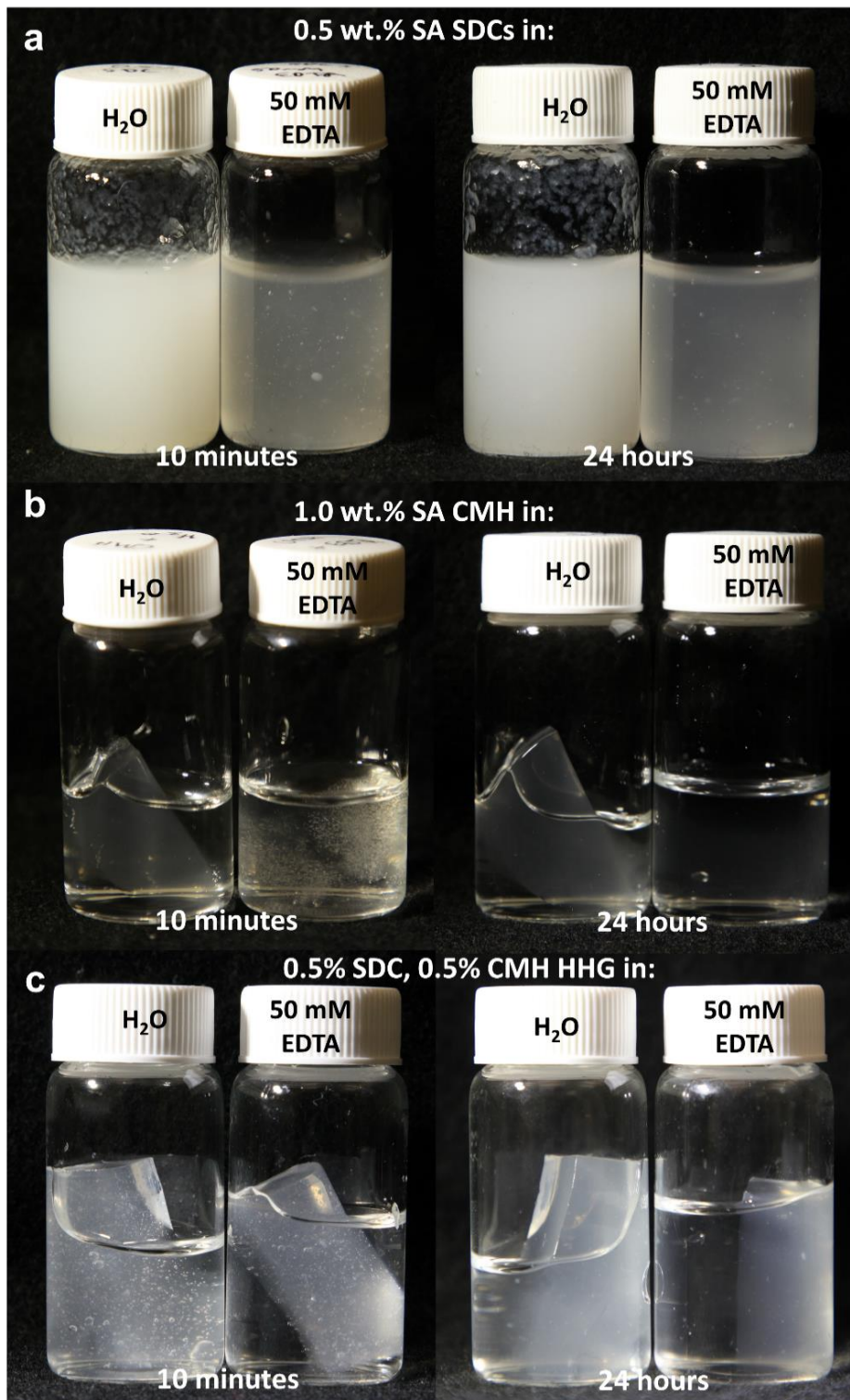


**Figure A6.** Degradation of SA SDC and CMH gels by chelating agents. (a) Pictures of 0.5 wt.% SA SDCs suspended in pure water and 50 mM EDTA after 10 minutes and 24 hours following 50mM EDTA solution addition. (b) Pictures of 1.0 wt.% SA CMH and (c) 1.0 wt.% HHG (0.5 wt.% SDC, 0.5 wt.% CMH) treated with pure water and 50 mM EDTA 10 minutes and 24 hours following addition of EDTA solution.

### Rheological time sweep analysis of SA CMHs and HHGs

To ensure that the ionization of CaCO<sub>3</sub> NPs by the GDL-mediated pH drop was solely responsible for the gelation seen in CMH and homocomposite hydrogel samples, a series of time sweep experiments were performed in which only GDL as well as CaCO<sub>3</sub> and GDL were added to pure SA CMH and SDC samples. When the combination of CaCO<sub>3</sub> NPs and GDL were added to a dissolved alginate (SA in H<sub>2</sub>O) solution, the sample saw gelation as expected. Without the presence of the CaCO<sub>3</sub> NPs, the SA solution did not see any gelation despite the drop in the solution pH from 8.1 to 3.6 after completing equilibration (Figure A7a).

The same experiments were performed on a 0.67 wt.% SA SDC suspension in deionized water and it was found that the addition of CaCO<sub>3</sub> did increase the storage and loss moduli of the suspension slightly initially, however, the dissolution of those CaCO<sub>3</sub> NPs over time by GDL hydrolysis led to the weakening of these suspensions and eventually, fluid-like behavior with the loss modulus eclipsing the storage modulus (Figure A7b). This result indicates that the SA SDCs are unable to be further cross-linked in suspension by the introduction of Ca<sup>2+</sup> ions *in situ*. Furthermore, the addition of solely GDL to the SDC suspension resulted in the weakening of the suspension over time. The combination of these results with the CMH and SDC systems shows that the greatly increased moduli seen in the homocomposite hydrogels is not a byproduct of any GDL-mediated pH drop or tertiary cross-linking phenomena between the SDCs and the CaCO<sub>3</sub>-GDL combination, but instead, is a result of the interplay between the molecular alginate network of the CMH and the colloidal alginate network of the SDCs.

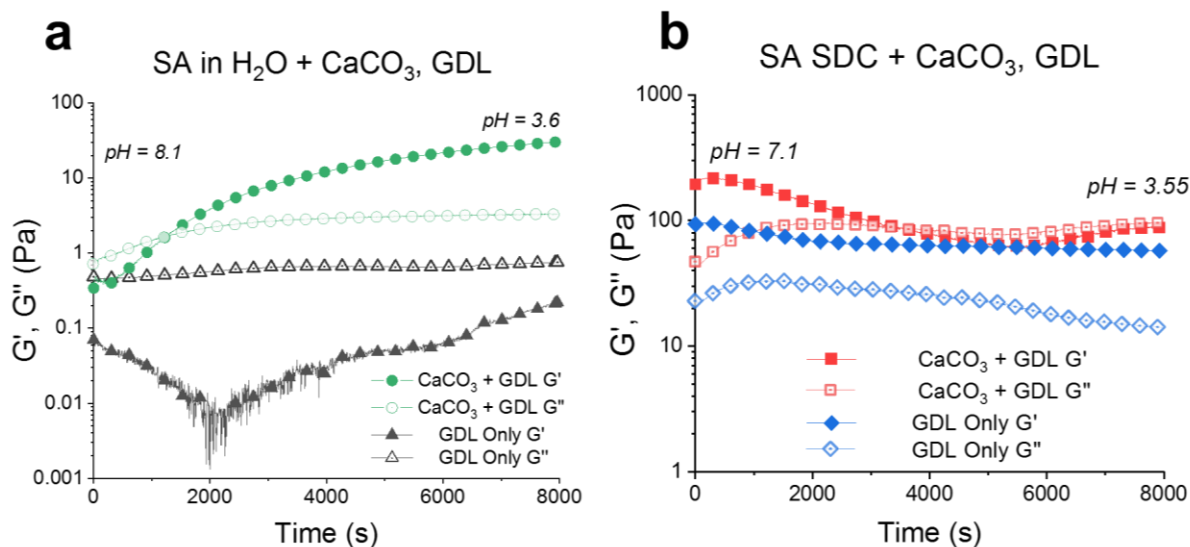


**Figure A7.** Time sweeps of SA SDCs and molecular alginate solutions (SA in H<sub>2</sub>O) with addition of CaCO<sub>3</sub> and GDL. (a) Time sweeps of 1.0 wt.% SA SDC suspensions with and without 0.1 wt.% CaCO<sub>3</sub> NPs following addition of 28.14 mM GDL. (b) Time sweeps of 0.67 wt.% SA SDC suspensions with and without 0.067 wt.% CaCO<sub>3</sub> NPs following addition of 18.77 mM GDL. Both graphs show the pH of the suspensions and solutions before and after GDL addition and equilibration.

Rheological analysis of the 1.0 total wt.% HHGs following equilibration (Figure A8) shows the maximum complex modulus of the 1.0 total wt.% equilibrated alginate HHGs resulted at a 1/1 SDC/CMH ratio, despite the maximum stiffness being obtained at lower SDC concentrations. A maximum complex modulus being obtained at 1/1 a SDC/CMH formulation is seen again in Figure 2.5b with the 1.5 total wt.% HHG mixtures prior to GDL addition.

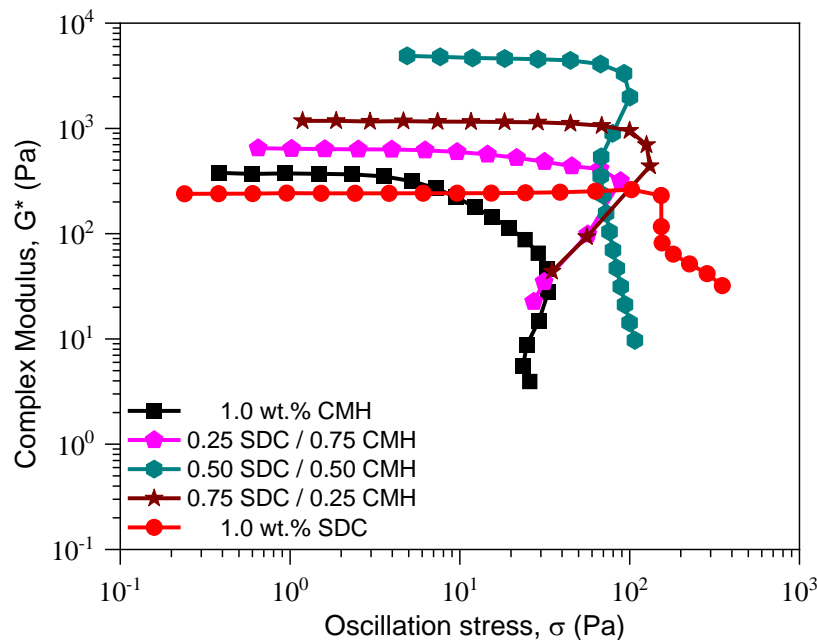


**Figure A8.** Amplitude sweeps of 1.0 wt.% total alginate HHG formulations. Cross-linked 1 wt.% HHGs of varying composition performed 2 hours after GDL addition at a frequency of 6.23 rad/s. These results show a maximum complex modulus for equilibrated HHGs is obtained at a 1/1 ratio of SDC/CMH.

#### Use of SDC reinforcement in double and triple “non-homocomposite” gel networks

The results suggest that SDC as additives can form the basis of strongly interconnected and efficient colloidal reinforcing networks in very broad ranges on “non-homocomposite” (multiple chemical component) hydrogels. We constructed and tested several heterocomposite gels containing SDCs networks. The results are summarized in Figure A9.

The first series of yield stress data, shown in Figure A9a are from gels formed by Polyvinyl Alcohol (PVOH) SDCs dispersed in Sylgard 184 PDMS liquid base. To prepare these systems, PVOH SDCs were first suspended in acetone at a concentration of 3 wt.%. This dispersion was then mixed directly with the liquid PDMS at varied concentrations and stirred magnetically at 65°C for 48 hours to remove the acetone from the mixture. The fumed silica in PDMS samples were prepared by slowly adding the Aerosil R202 particle powder to the PDMS while stirring at

65°C for 48 hours. The amplitude sweeps of SDC/PDMS composites show a 4-decade increase in the complex modulus with just 1.4 wt.% polyvinyl alcohol (PVOH) SDCs compared to the pure PDMS base. The comparison of these results with amplitude sweeps of fumed silica (Aerosil R202) in PDMS show that the SDCs far outperform the fumed silica in terms of viscoelastic modification of the continuous liquid PDMS phase even when the silica content is increased to four-fold that of the SDCs. This result highlights the extraordinary efficiency with which SDCs can form physical networks within a secondary liquid medium, as fumed silica is an extremely common thickening agent for inducing thixotropy and yield stresses through a percolated, colloidal network.

We also produced “triple network” hydrogel samples, including polyacrylamide (PAAm) – SA SDC – SA CMH hydrogels. First, an alginate stock solution of 1.0 wt.% SA SDCs, 1.0 wt.% SA, and 0.10 wt.% CaCO<sub>3</sub> NPs was prepared. Another stock solution of 28 wt.% acrylamide, ammonium persulfate (Sigma-Aldrich) was added as the acrylamide photo initiator (0.03 wt.%), and N,N-methylenebisacrylamide (Sigma-Aldrich) was added as the crosslinker for polyacrylamide. These two stock solutions were then mixed equally by weight and stirred vigorously. To induce cross-linking of the alginate and acrylamide networks, 20 wt.% GDL in water (5/1 GDL/CaCO<sub>3</sub> w/w) and N,N,N,N-tetramethylethylenediamine (TEMED; Sigma-Aldrich, .0025/1 TEMED/acrylamide w/w) were finally added to induce the crosslinking of both networks. The mixtures were stirred vigorously using a Vortex mixer and poured into 44 mm × 40 mm × 1 mm laser-cut molds, sealed using a 1.5 mm glass slide, and placed in a UV light chamber for 1 hour at 8 W power to complete cross-linking of both molecular networks.

In Figure A9b we compare representative stress-strain curves for traditional PAAm-SA CMH double network hydrogels consisting of 14 wt.% polyacrylamide and 1 wt.% SA CMH to a

“triple network” hydrogel that maintains the total alginate concentration of at 1 wt.% with a composition of 14 wt.% PAAm, 0.5 wt.% SA CMH, 0.5 wt.% SA SDC. The inclusion of the colloidal SDC component in the “triple network” leads to increased tensile strength of the resulting gels, however, the extensibility of the resulting gels is somewhat decreased compared to the double network gels prepared without the inclusion of the colloidal SDC network.

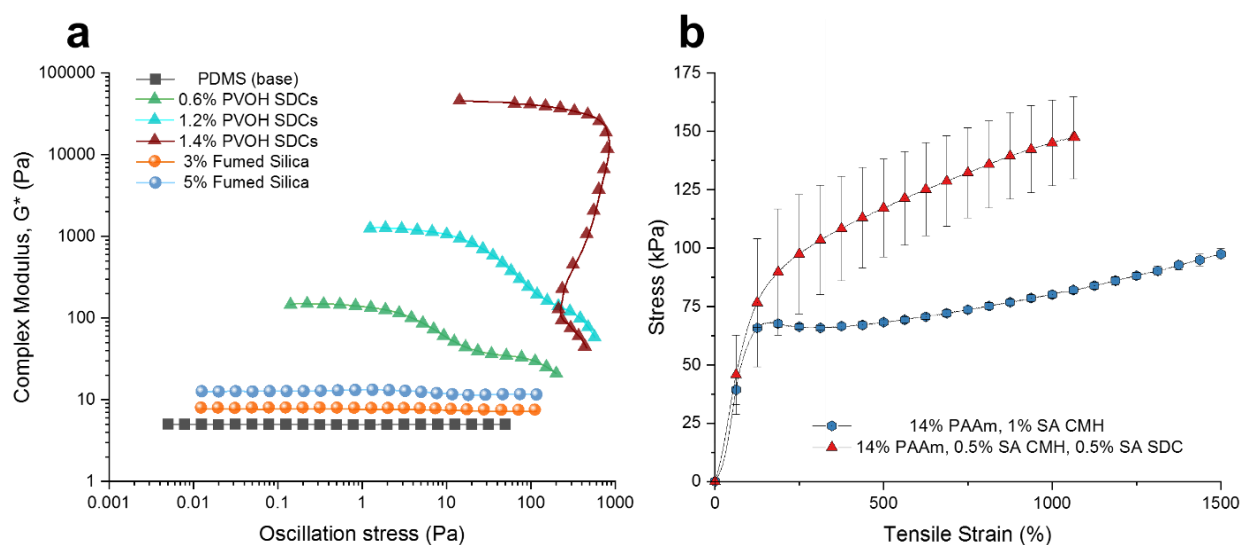


**Figure A9.** SDCs as universal composite yield stress additives. (a) Amplitude sweeps of polyvinyl alcohol (PVOH) soft dendritic colloids compared with fumed silica dispersed in PDMS base (Sylgard 184) showing yield stress emergence at low SDC concentrations (w/w). (b) Representative stress-strain curves of double network hydrogels consisting of 14% PAAm, 1% SA CMH and triple network hydrogels comprised of 14% PAAm, 0.5% SA CMH, 0.5% SA SDC (w/w) (n=3).

#### Experimental cells and procedures used in measurement of tensile properties of the gels

To prepare the HHGs with desired shape for tensile analysis and the syneresis measurements, laser cut acrylic sheets were used to make curing molds of desired dimensions for hydrogel curing and grippers for tensile analysis. A thin layer of cyanoacrylate adhesive (Gorilla Glue Gel) was applied at the gel-gripper interface and allowed to cure for 30 minutes prior to tensile analysis (Figure A10).

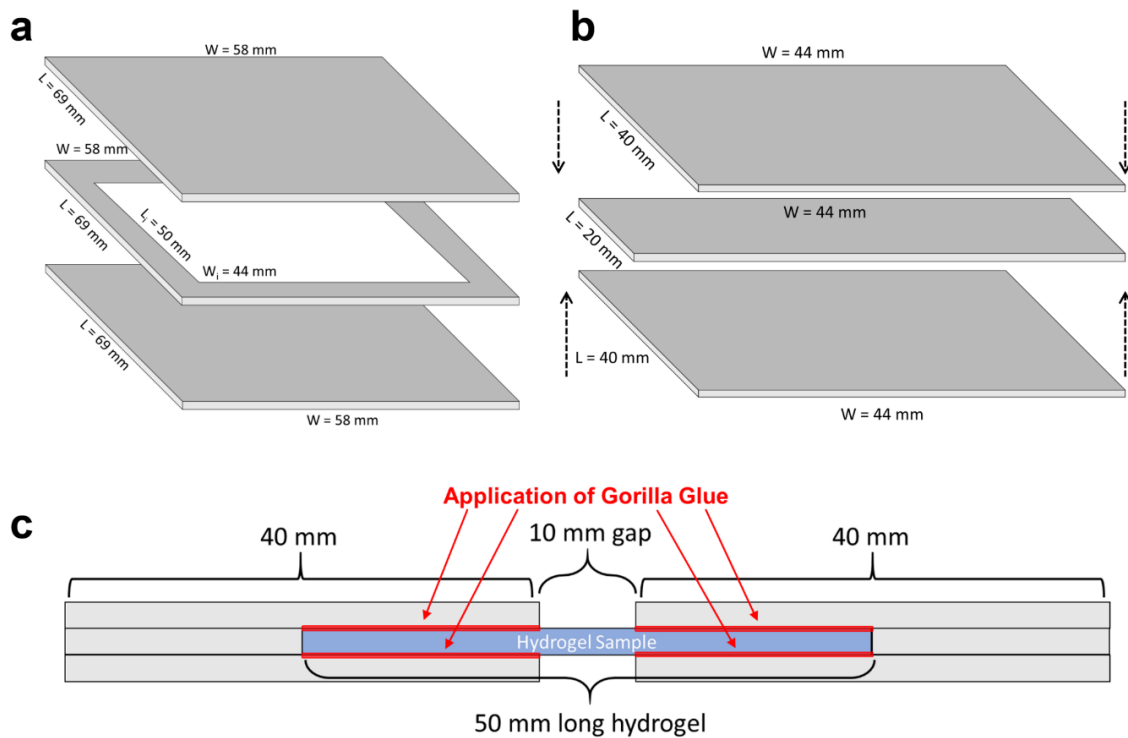


**Figure A10.** Schematic of the laser-cut acrylic (a) mold used to fabricate hydrogel sample for tensile analysis, (b) grippers used to hold the hydrogel during tensile analysis, and (c) the assembled grippers chemically bonded to the hydrogel sample with clamping zones indicated. All acrylic sheets were 1.59 mm thick and solvent-welded together using dichloromethane.

## Appendix B

### Porous Sheets and Membranes from Soft Dendritic Colloids

The pore networks in the membranes comprised of SDC (5%), fiber-sheet intermediate (10%), and nanosheet (12.5%) PVDF particles were visualized using scanning electron microscopy (Figure B1). The more fibrous SDC membranes appear to have a more ordered pores and smaller pore sizes compared to the nanosheet membranes, whose porosity appears more disordered from the overlapping sheet architecture.

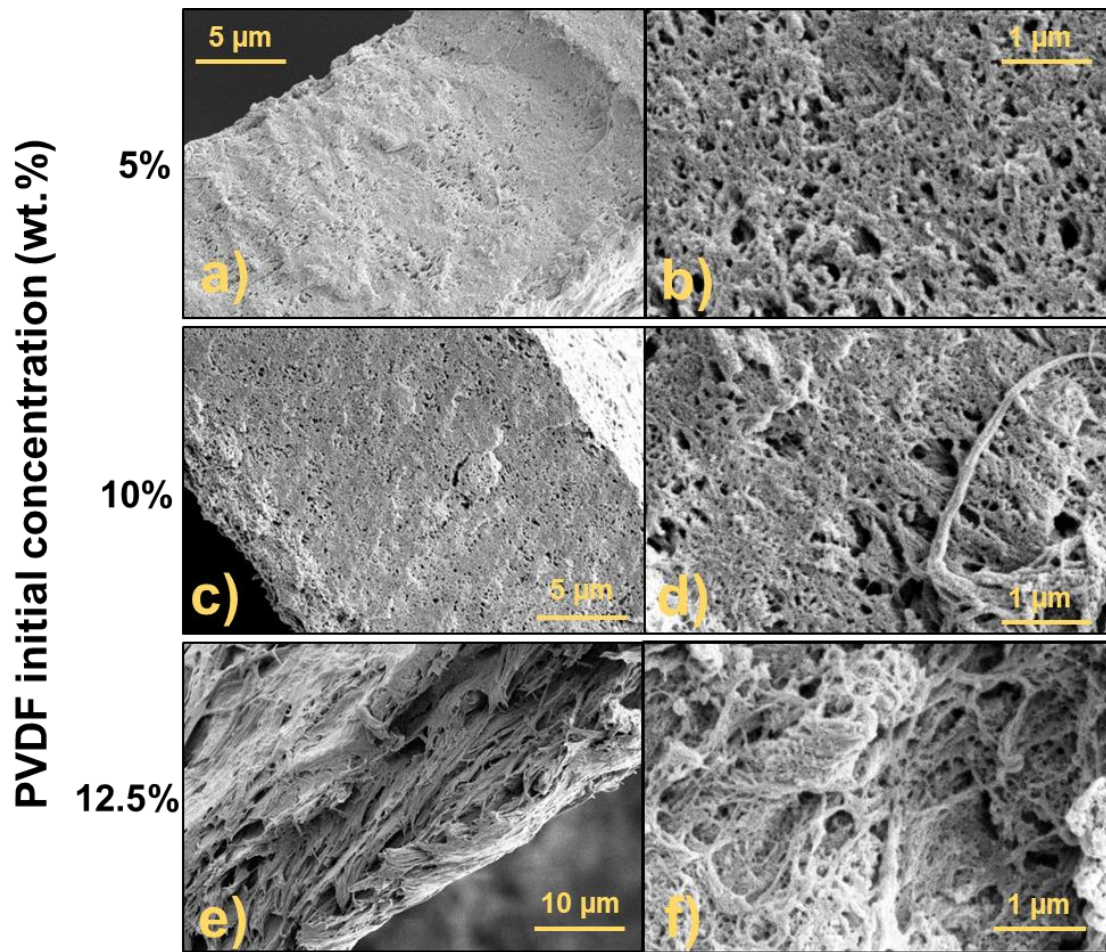


**Figure B1.** Cross-sectional scanning electron micrographs of membrane of SDC fibers (a, b), SDC fibers-NS intermediates (c, d) and NSs (e, f) at different magnifications.

The SDC membranes were placed in an oven at 90 °C for 1 hour, imaged, exposed to 130 °C for 1 hour, imaged, and finally exposed to 150 °C for 1 hour, and imaged (Figure B2). The shrinkage of the membranes was determined using pixel analysis on ImageJ software. The thermal stability of these PVDF SDC membranes above the 130°, the melting temperature of polyolefins, indicates their potential in high temperature lithium ion battery separator applications.

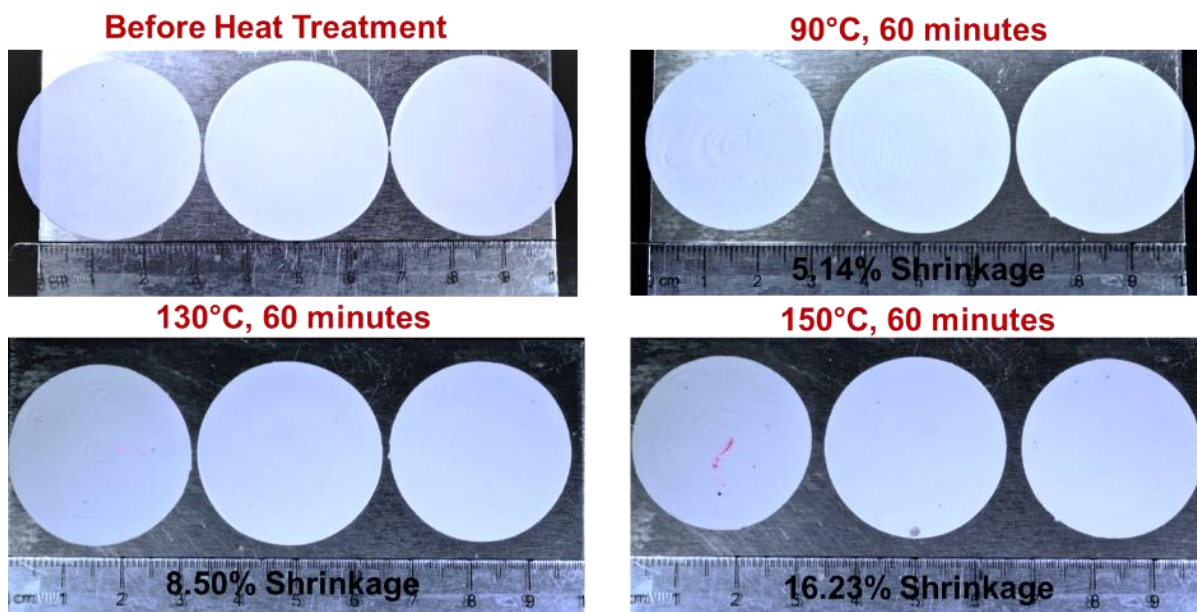


**Figure B2.** Thermal stability of 10% PVDF SDC membranes following exposure to increasing temperatures. The SDC fibers-NS intermediate membranes show that the PVDF membranes display minimal shrinkage following exposure at temperature far above polyolefin melting points.

## Appendix C

### Soft Dendritic Colloid Superhydrophobic and Anti-Icing Surface Coatings

The compositions of all SDCs described in Chapter 3 are shown in Table C1. Polyvinyl alcohol SDCs were crosslinked (0.2 wt.% SDCs in 300 mL acetone, add 50 wt.% glutaldehyde in water (Sigma-Aldrich), 5 drops pure sulfuric acid, magnetically stirred for 24 hours, washed thoroughly with Ethanol)

**Table C1.** Polymer, concentration, solvent and nonsolvent information for the fabrication of SDCs using shear-driven polymer precipitation with a turbulent nonsolvent flow.

Polymer	Concentration (wt.%)	Solvent	Nonsolvent
Polystyrene	5 %	Tetrahydrofuran	Water
Polyester	5 %	Chloroform	Methanol
Polyvinyl alcohol*	7 %	Water	Ethanol

### SDC Nonwoven Comparison

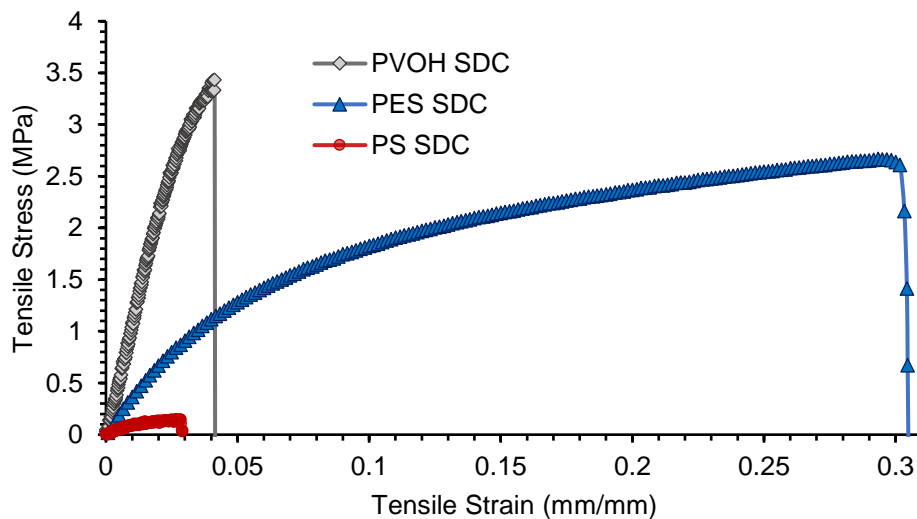


**Figure C1.** Stress-strain curves for representative nonwovens of polystyrene, polyester, and polyvinyl alcohol SDCs.

From these stress-strain curves, it is clearly seen that the stiffness of each polymer SDC nonwoven correlates strongly with the hydrophobicity, surface energies, and porosities of each of the SDC coatings (Table C1). The mechanical properties of polymer SDC nonwoven are listed in Table 3.1. The stress-strain curves for the bicontinuous PS/PVOH SDC nonwovens are shown in Figure C2.

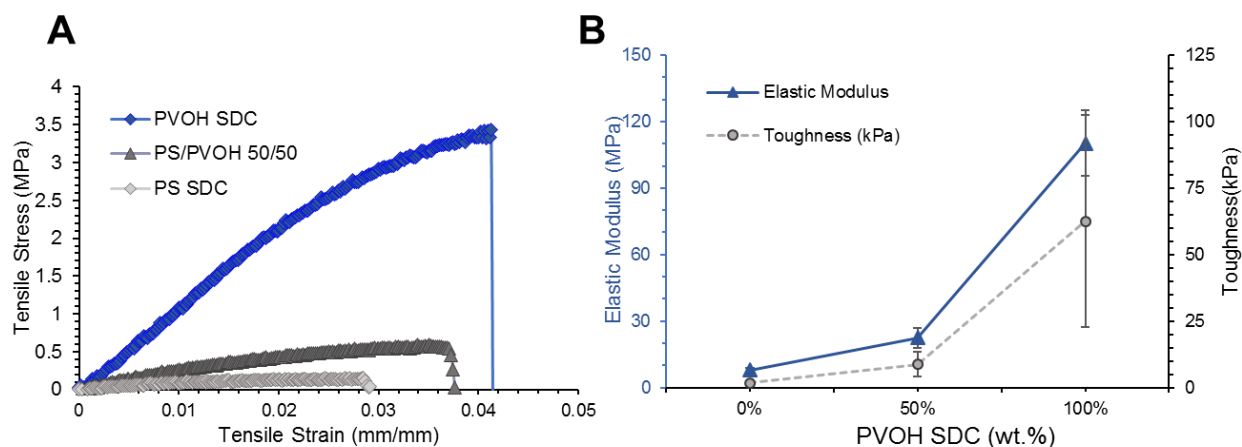


**Figure C2.** Mechanical properties of SDC networks. (a) Representative stress-strain curves for PS, PVOH, and PS/PVOH composite SDC nonwovens. (b) Elastic modulus and toughness of PS/PVOH SDC nonwovens.

Lap shear strength testing by using SDCs to adhere two glass plates and using mechanical testing instrument to measure the max force upon removal is another facile way of quantifying adhesion of SDCs composed of differing polymer or having differing morphologies (Figure C3). This method, however, may not be viable for comparing SDCs in a glassy phase (e.g. PS, PVOH) far below their  $T_g$  with polymers far above their  $T_g$  at room temperature (e.g. PES). However, utilizing this method and depositing just 1 mg of blended PS/PVOH SDCs of varying relative compositions resulting in a linear dependence between the values of the pure PVOH (54 N) and PS (8 N). For this reason, the blended, composite PS/PVOH coatings exhibit far better durability than the PS SDC coating.

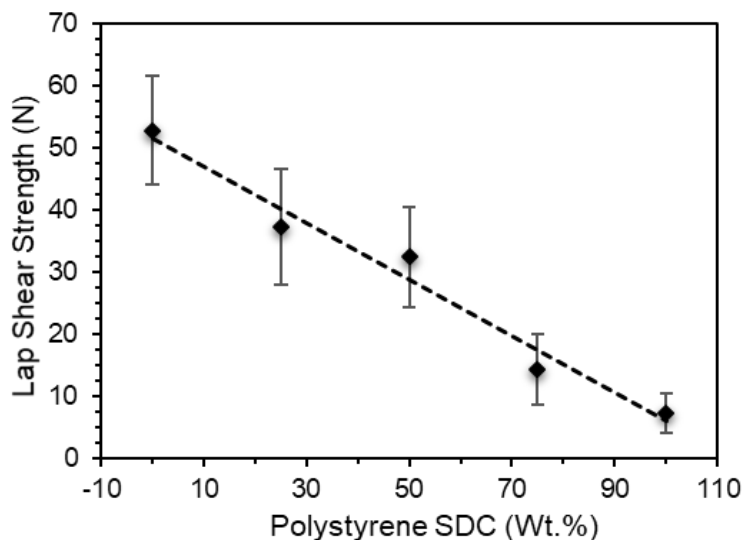


**Figure C3.** Lap shear strengths of 1 mg PS/PVOH SDC blends between glass slides with an overlap area of 25 mm x 13 mm (n=3) measured using an Instron 5943 with a crosshead speed of 5 in/min.

The experimental setup used to measure the shear ice adhesion strength on SDC coated aluminum substrates utilizing a force gauge affixed to a syringe pump at  $0.5 \text{ mm}\cdot\text{s}^{-1}$  is shown in Figure C4.

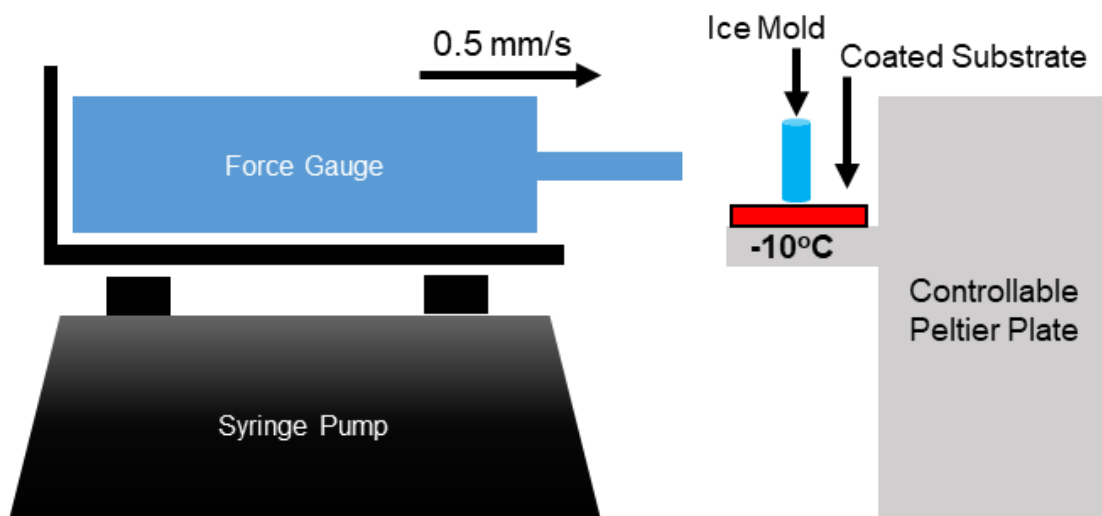


**Figure C4.** Schematic of the force gauge-syringe pump setup using hydrophobic polypropylene pipette tips on a controllable Peltier plate as ice molds to measure the ice adhesion strength on SDC coatings with a speed of 0.5 mm/second.

The increase in the droplet freezing time on an SDC surface is highly dependent on the polymer comprising the coating. As a general trend, SDC coatings of more hydrophilic and higher surface energy polymers make more hydrophilic and less porous SDC coatings. To examine the effect of coating thickness on the droplet freezing time, several PES and PS SDC coatings were prepared of varying thickness. In Figure C5, the droplet freezing time vs. the mass per unit area of the coating and the thickness of the coating for the same data.

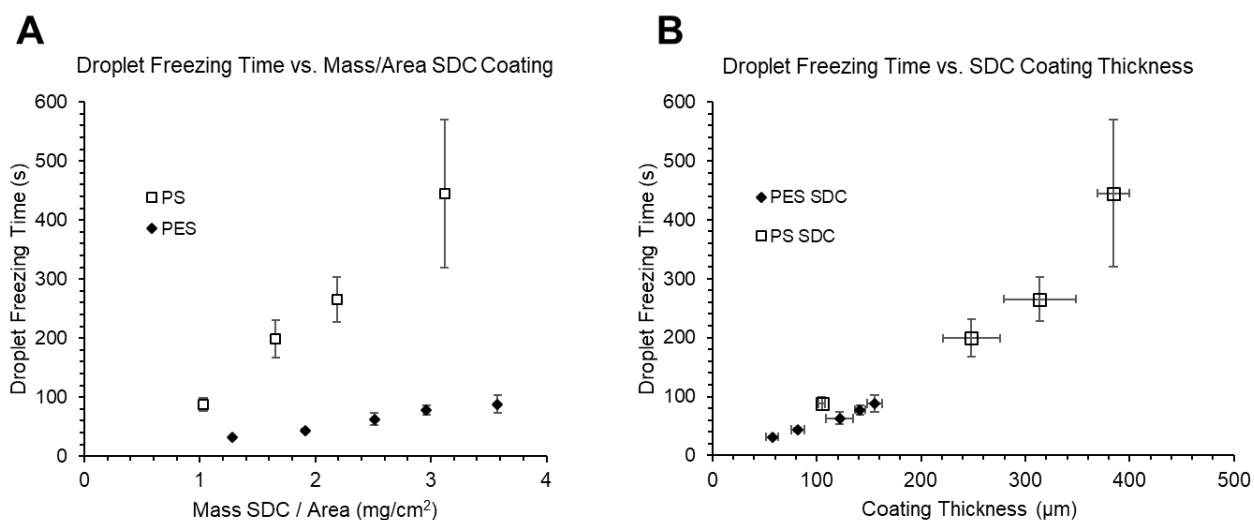


**Figure C5.** Water droplet freezing time vs. (a) mass of SDC per area of coating (mg/cm<sup>2</sup>) and (b) coating thickness (μm) for PS and PES SDC coatings.

Per unit mass, the PS SDC coating is far more efficient in delaying the nucleation of the water droplet. This difference can be mostly attributed to the higher porosity of PS SDC coatings compared to the PES coatings that allows greater insulation by larger air pockets throughout the coating. PS SDC coatings of approximately the same mass per unit area have larger thickness than the PES SDC coatings (Figure C5b). At the same thicknesses, the PS SDC coatings may delay ice nucleation slightly more efficiently than the PES SDC coatings due to decreased contact area for heat flow on the more hydrophobic surface, but it is instead the higher porosity of PS SDC nonwovens that mostly accounts for the delay in droplet nucleation.

## Appendix D

### Layer-By-Layer Polyelectrolyte Films for Food-Grade Barrier Nanocoatings

#### Polyelectrolyte layer-by-layer charge cycling

Polyelectrolyte multilayer (PEM) film growth is known to be highly dependent on the pH of both solutions. Here, we consider the “charge cycling” of chitosan (CS) and alginate (Alg). Because CS precipitates from solution above a pH of 6.5 and Alg similarly begins precipitating below a pH of 4.0, the charge profiles of CS and Alg are shown in Figure D1. The charge profile for any given polyelectrolyte is dependent on the  $pK_a$  of its ionic functionality and the precipitation and aggregation of a polymer will also depend on polymer characteristics like molecular weight as well as temperature, ionic content, and temperature. Therefore, the technical operating window for the layer-by-layer deposition of two polyelectrolytes will vary greatly. Generally, there are three regimes of charge cycling for PEM growth. A forward charge cycle (Figure D1a-b) occurs when the  $pH_{CS} > pH_{Alg}$  and both polyelectrolytes experience a higher charge in the other polymer’s solution, driving faster film growth. When the two solutions are the same pH, no charge cycle occurs for the polymers when exposed to the other solution, so more linear coating growth is observed and the rate of film growth is governed instead by the morphologies of both polyelectrolytes at that pH (Figure D1c, Figure D2). A reverse cycle occurs with  $pH_{CS} < pH_{Alg}$  and both polymers may experience a decrease in charge upon exposure to the other solution pH leading to the slowest observed film growth (Figure D1d).

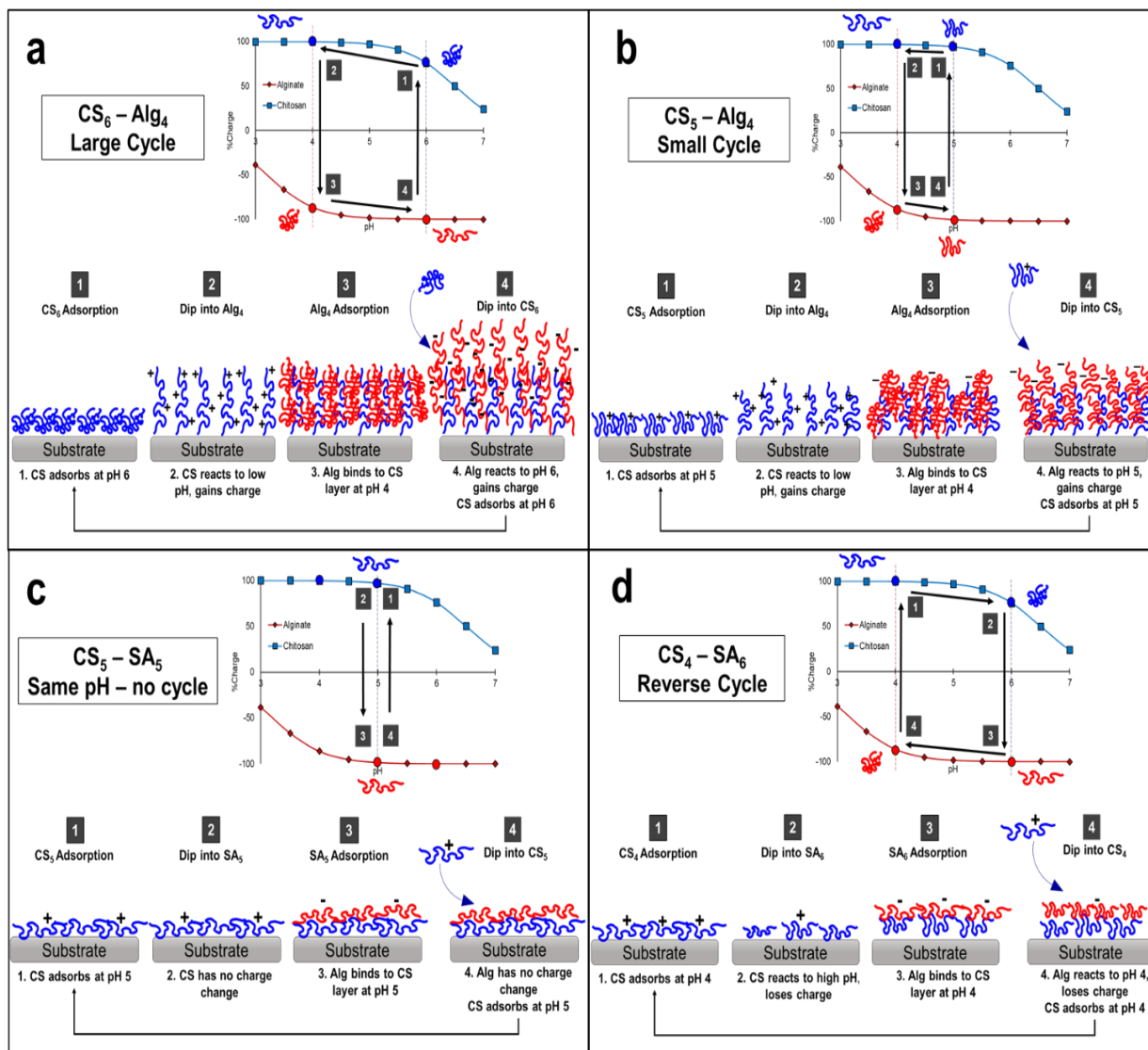


**Figure D1.** Schematics illustrating the different cycle of charging that polyelectrolytes (specifically CS and Alg) undergo during electrostatic LbL film deposition and their dependence on the pH of both polymer solutions. (a)  $CS_6 - Alg_4$  large forward cycle, (b)  $CS_5 - Alg_4$  small forward cycle, (c)  $CS_5 - SA_5$  same pH cycle, (d) a  $CS_4 - SA_6$  reverse cycle.

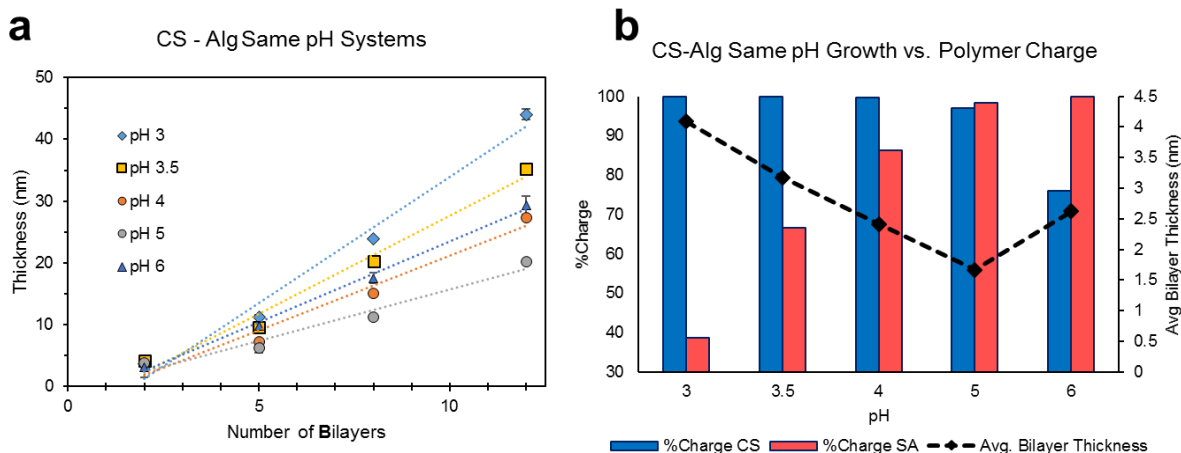


**Figure D2.** Film thickness vs. bilayer number for same-PH CS—Alg PEMs. (a) Film growth for 2, 5, 8, and 12 BL of same-pH CS-Alg films and (b) and comparison of polymer charges vs. average bilayer thickness (dashed line) for same-pH CS-Alg systems.

To investigate other system parameters that could optimize the CS-Alg PEM growth, a different CS molecular weight (15 kDa) was investigated as was the addition of NaCl to other deposition solutions (Figure D3). Both the reduction of CS molecular weight and the addition of NaCl did not show significant effects on coating growth, especially when compared to an increase in solution temperature.

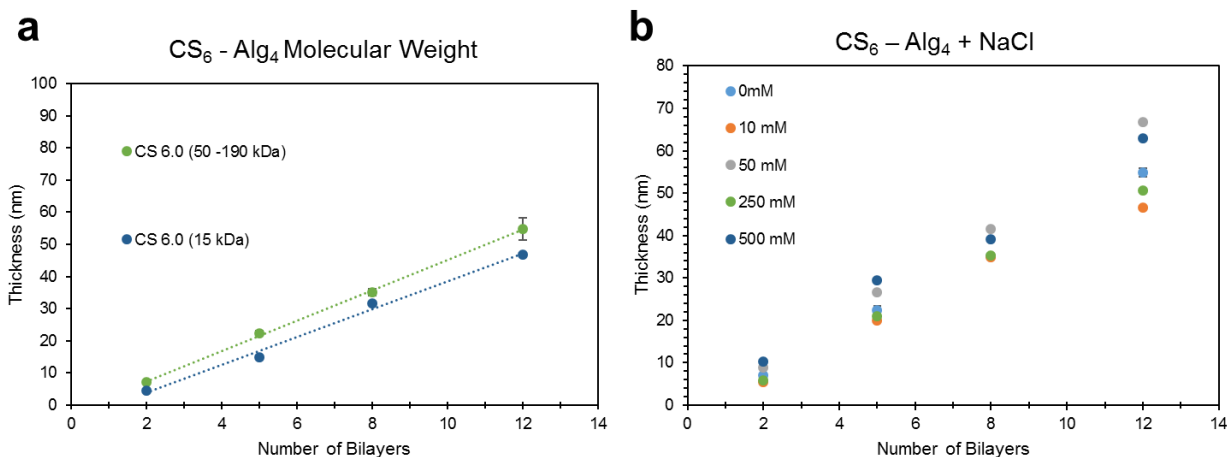


**Figure D3.** Film thickness vs. bilayer number for CS<sub>6</sub> – Alg<sub>4</sub> systems with (a) chitosan solutions with different molecular weights (15 kDa vs. 50-190 kDa) and (b) with solutions that contain varying NaCl concentrations.

## Physical properties of CS-Alg Coatings

To investigate whether the mechanical properties of CS-Alg PEMs were dependent on the charge cycling used in their fabrication, a same-pH CS<sub>3.5</sub> – Alg<sub>3.5</sub> coating was directly compared to a forward cycle CS<sub>5.0</sub> – Alg<sub>3.5</sub> coating using nanoindentation. In Figure D4, it can be seen that the same pH Cs-Alg coating has slightly higher reduced moduli and hardness values compared to the forward cycle coating. This difference can be attributed to greater incorporation of water into the PEM of LbL coatings with exponential growth seen in forward charge cycles.<sup>74</sup>

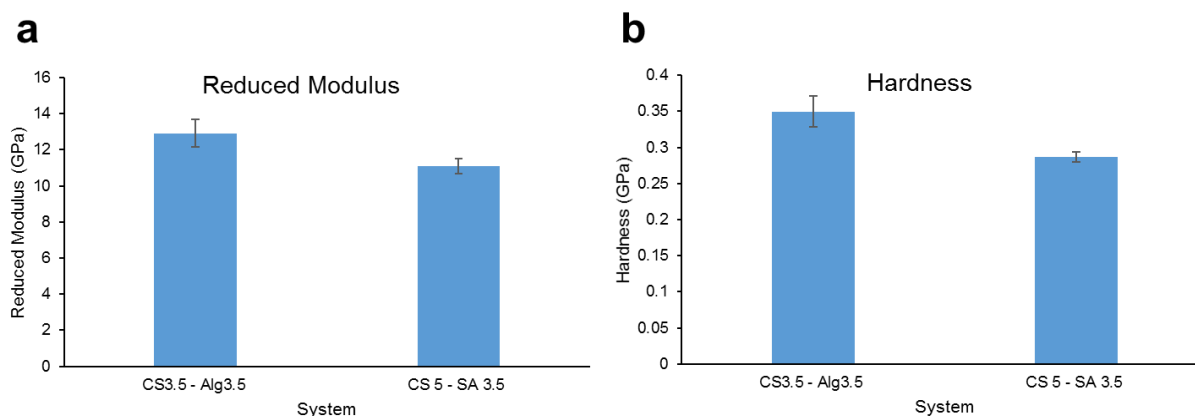


**Figure D4.** Mechanical properties of CS-Alg films determined by nanoindentation (50  $\mu$ N indents). (a) Reduced modulus and (b) hardness values of a charge cycle film (CS<sub>5</sub> – Alg<sub>3.5</sub>) and same pH system film (CS<sub>3.5</sub> – Alg<sub>3.5</sub>).

The surface roughness of the CS-Alg PEM is dictated by the pH of the final deposited layer and the conformation of the polymer at that pH. To illustrate this dependence, atomic force microscopy (AFM) was performed on layers 6.5, 7.0, 7.5 and 8.0 of CS-Alg systems of CS<sub>6</sub> – Alg<sub>3,4,5,6</sub> (Figure D5). The highest surface roughness was seen in the greater forward charge cycle system and a trend to highly smooth surface roughness with decreasing charge cycling is seen.

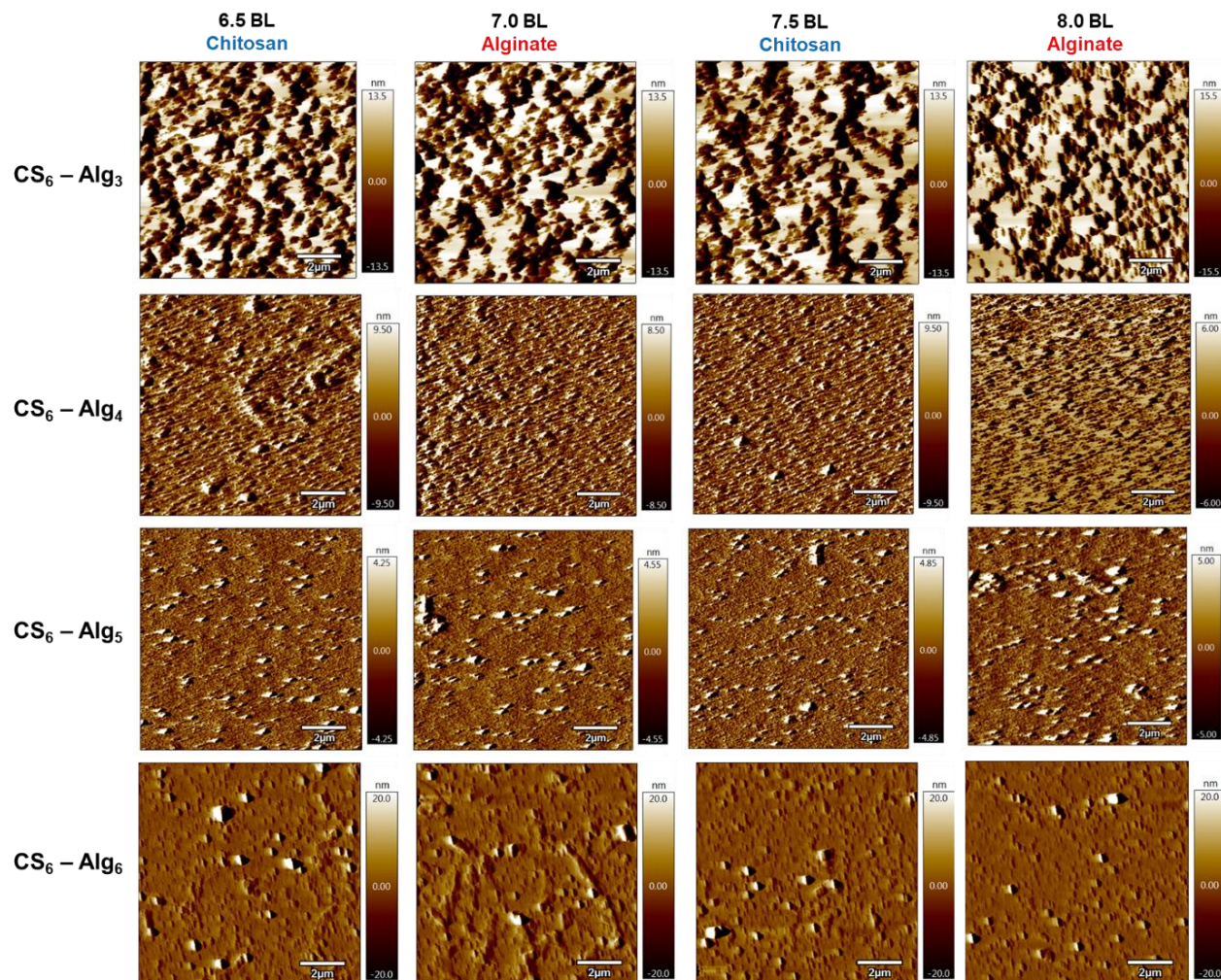


**Figure D5.** Topographical amplitude atomic force microscopy scans showing surface roughness of 6.5, 7.0, 7.5, and 8.0 BL samples of CS<sub>6</sub>-Alg<sub>3,4,5,6</sub> films. Bilayer numbers were chosen to insure film had completed nucleation and growth phase.

Finally, the mechanical performance of CS-Alg PEMs under strain were analyzed by depositing the PEM onto a highly soft polyurethane rubber substrate. Following deposition, the CS-Alg coated substrate was strained to set values and immediately imaged using electron microscopy (Figure D6). The CS-Alg PEM is able to withstand 10% strain without cracking, however, cracks appear with applied strain of 20% and greater. This result indicates that CS-Alg coatings have some elastic behavior prior to cracking, which sacrifices the efficacy of the coating's

barrier and may suggest that some magnitude of hydrogen bonding is occurring in the CS-Alg PEM, which is known to enable more elastic behavior in highly ionic PEM systems.

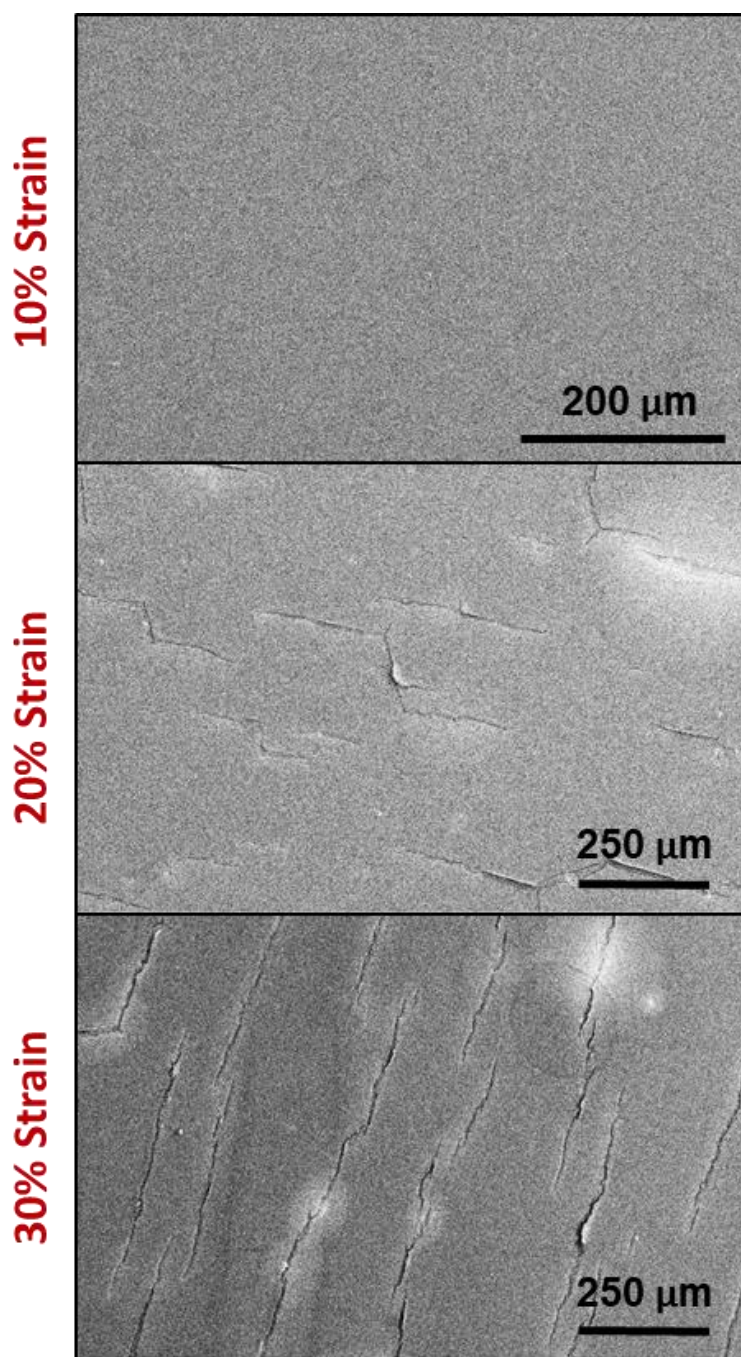


**Figure D6.** Scanning electron micrographs of the cracking of CS<sub>6</sub>-Alg<sub>4</sub> (60°C, 45s dips, 30 BL) films coated on a polyurethane rubber substrate following varying applied strain.